4
2007

This is to certify that the
dissertation entitled

THE EFFECT OF GRAIN SIZE, MICROCRACKING AND GRAIN BOUNDARY GROOVING ON OSTEOBLAST ATTACHMENT IN HYDROXYAPATITE

presented by

IAN ORLAND SMITH

has been accepted towards fulfillment
of the requirements for the

Ph.D. degree in Materials Science and Engineering

Major Professor's Signature

April 25, 2007

Date

MSU is an affirmative-action, equal-opportunity employer

THE EFFECT OF GRAIN SIZE, MICROCRACKING AND GRAIN BOUNDARY GROOVING ON OSTEOBLAST ATTACHMENT IN HYDROXYAPATITE

By

Ian Orland Smith

A DISSERTATION

Submitted to
Michigan State University
in partial fulfillment of the requirements
for the degree of

DOCTOR OF PHILOSOPHY

Department of Chemical Engineering and Materials Science

2007

ABSTRACT

THE EFFECT OF GRAIN SIZE, MICROCRACKING AND GRAIN BOUNDARY GROOVING ON OSTEOBLAST ATTACHMENT IN HYDROXYAPATITE

By

Ian Orland Smith

This research examined the effect of particle size, microcracking and grain-boundary grooving in hydroxyapatite (HA) ceramics on osteoblast (OB) attachment, with the overall goal of understanding the role of physical characteristics in optimized scaffolds for bone tissue engineering.

Bimodally porous HA scaffolds were fabricated by foaming and sintering either micron-scale or nano-scale HA powder, yielding two sets with average grain diameters of 8.6 ± 1.9 μm and 588 ± 55 nm, respectively. OBs were seeded onto these scaffolds and counted at 0.5, 1, 2 and 4 hours for attachment and 1, 3 and 5 days for proliferation using a hemacytometer. Results showed that OB attachment and proliferation was not significantly affected by the change in grain size and may depend more on the bimodal porosity of the implant. However, as our attempt to reduce the error in the hemacytometer counts was not fully successful, a more accurate method of counting the OBs, such as a quantifiable dye, must be used to verify this trend.

While microcracks occur as a result of thermal processing of HA, these TEA-induced cracks are not easily controlled. For our studies we used Vickers-induced microcracks to quantify the effect of microcracking on OB attachment in HA. OB attachment was not significantly affected at one hour, but increased at four hours to 61% higher than on non-microcracked control specimens. This increase indicates that microcracking does have an effect on OB attachment and should be studied further, to assess its effect on OB proliferation and differentiation. It is not surprising that microcracks have a positive effect on OB attachment, as this mimics the natural process of bone remodeling. However, they are not likely to occur in nano-grained HA as a result of processing, as its small grain size falls below the known values of critical grain size for microcracking (G_{CR}) in HA.

grain boundary grooving in dense HA is also investigated in this dissertation. OBs were seeded onto grain boundary grooved and control dense HA discs and counted at one and four hours. At both times, the presence of grain-boundary grooves did not have a significant effect on OB attachment.

These findings eliminate microcracking and grain boundary grooving as contributing factors in increased OB attachment on HA substrates with nano-scale grains. Having ruled out these two phenomena, the observed increase in OB attachment on nano-grained HA is likely due to either the associated increase in surface roughness or the presence of nano-scale charge variations at grain boundaries. The latter is the subject of a current study by our group.

ACKNOWLEDGEMENTS

I would like to thank my parents, Keith and Karen Smith. Their undying support during my time at Michigan State University made this all possible.

I would also like to thank my academic advisor, Professor Melissa Baumann, for her guidance and assistance during the pursuit of my studies at Michigan State University. Her oversight helped me to focus and accomplish everything that I set out to do. She has helped me to realize my potential in the realm of engineering research.

Additionally, I would like to thank Professor Eldon Case for all of his help. By sharing his wealth of knowledge, he has truly enriched my learning experience.

TABLE OF CONTENTS

LIST OF TABLES

LIST OF FIGURES

CHAPTER 1

CHAPTER 2

CHAPTER 6

CHAPTER 7

CHAPTER 8

CHAPTER 9

APPENDIX A

APPENDIX B

APPENDIX D

APPENDIX E

CHAPTER 1

INTRODUCTION TO CALCIUM PHOSPHATE BONE TISSUE ENGINEERING

This research examined the effect of particle size, microcracking and grain-boundary grooving in hydroxyapatite (HA) ceramics on osteoblast (OB) attachment, with the overall goal of understanding the role of physical characteristics in optimized scaffolds for bone tissue engineering. Images in this dissertation are presented in color.

BONE STRUCTURE

Structurally, bone is composed of two primary types of tissue.[1,2] On one hand there is cortical bone, also known as compact bone, found prominently around the exterior of the diaphysial regions of long bones. Cortical bone is composed of a network of osteons, also known as Haversian systems, made up of thin lamellae of bone tissue surrounding channels called Haversian canals (Figure 1). These Haversian canals act as a conduit for blood vessels and nerve fibers and travel parallel to the axis of loading in the bone. Within the lamellae are cavities called lacuna, which are home to osteocytes (inactive osteoblast cells). These cells exchange nutrients with the rest of the bone tissue via small channels called canaliculi, which contain extensions of the osteocytes. Near the outer region of the bone, lamellae spread out to form a concentric ring around the entire bone, adjacent to the periosteum.

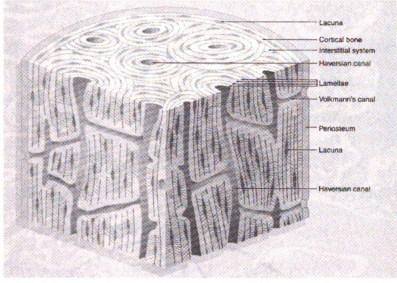

Figure 1: Schematic of the Haversian systems within cortical bone tissue[1]

Cancellous, or spongy bone consists of bone-tissue trabeculae and interconnected pores containing the bone marrow. These trabeculae also consist of lacunae-containing lamellae, although these lamellae are not oriented as in cortical bone.[1]

The interconnected porosity of cancellous bone is vital for the transport of nutrients via the bone marrow vasculature. Blood vessels run from the periosteum, outside of the cortical bone, through the Haversian canals, through the trabelcular space and into the medullary canal.[1] In order to create scaffolds that are able to connect with the surrounding bone tissue, it is important to reproduce this interconnected porous network. This will be discussed later.

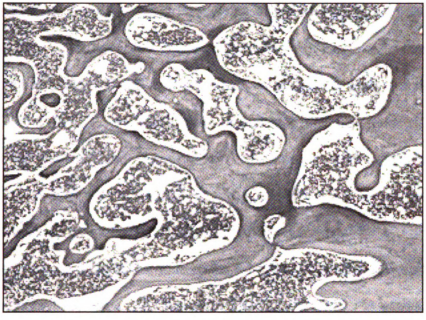

Figure 2: Histological section showing trabeculae within cancellous bone tissue[1]

Bone remodeling and growth arise as a result of new bone production by osteoblasts and concurrent resorption of old bone by osteoclasts. These cells are active as bone is being continually remodeled as a result of normal stresses applied during everyday use.[2-4]

When an osteoblast is forming new bone, it is deemed an active osteoblast. These cells act to synthesize type 1 procollagen molecules and release them into the area of growth, called the osteoid. Within the osteoid, procollagen molecules align themselves and, over the course of approximately 10 days, calcium phosphate is deposited and eventually matures into bone apatite. As active osteoblasts are consumed by newly formed bone, the majority die and a fraction of the remaining living cells become encased within this bone and become osteocytes.[1,3]

There are a variety of approaches for studying osteoblast (OB) function. Several cell lines are available for use, including rat osteogenic sarcoma (ROC) cells such as the UMR 106 line and the newborn mouse calveria-derived MC3T3-E1 line.[1,5,6] The MC3T3-E1 osteoblast clonal cell line is used in many cell attachment, proliferation and differentiation experiments, in lieu of primary human or animal OBs due to their greater availability and well-established bone forming activity[7], as well as its ability to differentiate on hydroxyapatite.[1] Further, using a clonal line eliminates the problems that are inherent to primary cell cultures, such as difficulty in cell isolation.[7-10] The use of MC3T3-E1 OBs in place of primary OBs in tissue engineering has been shown to be a suitable substitute.[11] We used OBs rather than osteoclasts (OCs) for all of our studies because we chose to focus on new bone production, rather than bone resorption that acts as a trigger for bone production.

NEED FOR BONE REPLACEMENT

Each year in the United States alone there are over 500,000 bone graft procedures performed as a result of trauma damage and resection as well as deterioration associated with disease.[12-14] Bone tissue graft options include autograft, allografts and artificial replacement materials.

Autografts require the removal of bone tissue from a donor site within the patient's body. This technique has inherent complications. Autografts require that bone be removed at the donor site to replace and repair the damaged or missing tissue. By causing damage to repair or replace missing or damaged tissue,

autografting is problematic, and therefore cannot involve load-bearing donor sites. Additionally, retrieval of autograft tissue requires a second surgery at the donor site, thereby increasing the morbidity/mortality rate.

Allograft tissue on the other hand, originates in a same-species, predominately cadaveric, donor other than the patient. Cadaveric tissue is in limited supply and carries the possibility of tissue rejection and disease transmission.

Artificial bone tissue replacement materials are an option being developed through an extensive range of research. These bone substitutes fall into three categories: scaffold-based, cell-based and factor-based. This dissertation focuses on scaffold-based bone substitutes. An ideal bone replacement scaffold for filling a critical sized gap in bone tissue would have a bimodal pore structure similar to that of cancellous bone. This structure allows ingrowth of new tissue into the larger macropores and nutrient transmission through the micropores. Interconnected macropores between 200-500 μm in diameter have been shown to promote new tissue ingrowth and vascularization.[15,16]

In addition to having a pore structure conducive to bone ingrowth, an ideal bone replacement scaffold would also be chemically similar to natural bone. Consequentially, ceramic materials are involved in approximately 60% of available bone graft substitutes where, the calcium phosphate (CaP) family of materials is used in the majority of artificial bone grafts.[12] In particular, hydroxyapatite (HA, $Ca_{10}(PO_4)_6(OH)_2$) is frequently used, because of its similarity to the natural apatite bone mineral.[67, 68, 35, 12, 15, 17-20]

One way in which bone substitute materials are being designed to better mimic bone is through the design of nanoscale ceramic/polymer composites. These composites consist of a nanoscale CaP ceramic, usually HA, and collagen[21-23], a non-collagen polymer such as polyamide[24-26] or a combination of the two[27,28]. Some of these composites show improved compressive strength compared to HA, but the inclusion and eventual degradation of polymers such as polylactic acid (PLA) has in some cases been shown to have a negative effect on cell behavior.[29] Also, while some of these composite systems contain components found in living bone, they do not mimic its complex heirarchical structure, which is compised of apatite crystals, 15 - 200 nm in length and 10 – 80 nm in width with a thickness between 2 and 7 nm.[30] These crystals reside within the collagen fibers, which form lamellar sheets in the concentric rings of osteons in cortical bone[2] and the trabeculae of cancellous bone.[31] Therefore, one current thrust of research is in the development of a bioceramic whose structure mimics the nano-scale features of bone.[32]

CALCIUM PHOSPHATE BIOMATERIALS

Calcium phosphate (CaP) ceramics have been frequently studied as candidates for hard tissue replacement.[15] While these materials are not osteoinductive, they are biocompatible and osteoconductive, meaning they elicit a biologic response *in vivo*.[33] CaP ceramics commonly used in biomedical engineering include α-tricalcium phosphate (α-TCP), β-tricalcium phosphate (β-

TCP), tetracalcium phosphate (TTCP) and hydroxyapatite (HA).[15] Some benefits of using each will be discussed later in this chapter.

One use for CaP in biomedical engineering is as an osteoconductive coating for alloys in orthopedic devices and its benefits as a coating for these metals used as orthopedic implants have been well documented.[34-36]

Because of its high degree of similarity to bone apatite, HA ($Ca_{10}(PO_4)_6(OH)_2$) is a frequently investigated material for use as a bone replacement. As a result of this inherent chemical similarity, HA exhibits exceptional biocompatibility. Although HA shows a favorable propensity for attracting OBs, its properties as a bone implant are constantly being adjusted for improvement.[37] For example, by changing the processing parameters of the HA itself, as well as through post-processing surface treatments OB attachment can be altered.[38] These methods and others are discussed later in this chapter.

Along with surface energy and surface composition, the biomaterial surface charge is a factor which can be used to promote a better bone/implant interface.[39] Osteoblasts have been shown to have a propensity for attaching to HA, beginning with an electrostatic attraction. OBs in suspension exhibit a large enough gap in ζ-potential with respect to HA to exhibit an interaction deemed unstable (meaning conducive to interparticle flocculation) by the Hogg, Healy and Fuerstenau model for interparticle stability.[40-42] Osteoblasts attach to, grow on and eventually differentiate, laying down mineral matrix upon HA.[7,8] OBs have been shown to bind more effectively to HA than other common biomaterials, including Ti and steel, because of increased fibronectin and vitronectin

adsorption *in vivo*.[43] HA belongs to the group of materials dubbed "bioactive", because of their tendency to bond with surrounding bone tissue and to promote bone formation *in vivo*. [39,44] However, the use of this term here is incorrect because bioactivity, strictly speaking, refers to the ability of a material to produce living matter. This is something that HA cannot accomplish on its own.

The initial reaction between a bioceramic material and its environment is determined by the rate of dissolution from the ceramic and the precipitation back onto the ceramic, prior to the attachment of OBs to the specimen surface. This rate of dissolution varies based on the Ca/P ratio of HA-based materials, and is slowest in HA (~1:90 vs TCP[43]). This lack of resorbability shown by HA *in vivo* offers a trade-off though, in that HA implants maintain their mechanical integrity over time and even result in improved shear strength at the bone/implant interface compared with α- and β-TCP, exhibiting a 10x increase, determined using the push-out mechanical test.[45]

Hydroxyapatite, a ceramic, exhibits good compressive but poor tensile mechanical properties. Dense HA has a Young's modulus (E) of 40 – 117 GPa, a compressive strength of 294 MPa and a bending strength of 147 MPa.[46] In comparison, a typical femur possesses a Young's modulus (E) of 13.5 GPa and a bending strength of 250 MPa.[46] This disparity in strength is what currently limits the use of HA bone-replacement scaffolds to primarily non-load-bearing applications.[46] In order for a HA scaffold to effectively promote bone ingrowth, it must be porous, and therefore have an ever further disparity in strength to cortical bone.[16]

OSTEOBLAST RESPONSE TO HYDROXYAPATITE

The scope of our research within this dissertation is focused mainly on the interaction between OBs and the HA surface, either within a bimodally porous HA ceramic network or on the dense HA ceramic substrates. The way in which this interaction is affected depends on the properties of that surface, those that are intrinsic in nature and those that are extrinsic. The difference between the two will become more apparent later in this chapter, but intrinsic properties are those that are inherent to the particular type of HA being studied such as crystallinity, grain size and inherent surface roughness, chemical additives during processing and porosity, and are a result of processing parameters. Extrinsic properties refer to those which result from further treatment of the as-processed ceramic and include, for example the surface functionalization of the as-processed HA substrate.

By varying the crystallinity of HA, the dissolution rate is altered.[47] For example, it was recently shown that nano-crystalline and nano-amorphous HA elicited improved OB adhesion than conventional crystalline HA and this response was similar to that found on RGD functionalized conventional HA.[47] This is consistent with earlier findings that amorphous materials, such as Bioglass® and apatite-wollastonite (A-W) glass ceramic better encouraged bone ingrowth when compared to crystalline HA.[19,48] For example, particles of Bioglass® and A-W glass ceramic brought about bone ingrowth rates 2 and 1.3 times that associated with crystalline HA particles, respectively, after 24 weeks *in vivo* (rabbit model). Surface functionalization using RGD-containing peptides is

another example of a treatment which improves OB attachment. Functionalizing the HA surface with EEEEEEEPRGDT improved OB attachment[49] and using GRGDSPC and cyclo-DfKRG increased attachment at 3 and 24 hours[50] versus HA control. (The nomenclature for these peptides is designed to indicate their specific sequence of amino acids, with each letter referring to one of these amino acids.)

The relationship between nano-grained ceramics versus micro-grained dense bioceramics as related to OB behavior on nano-grained versus micro-grained dense bioceramics has been investigated by Webster et al. Using dense substrates with nano-scale grains increases OB attachment[51-53] and proliferation[51,54], alkaline phosphatase (AP) activity[51,54] and calcium deposition[51,54] and decreases OB motility[51,54]. For example, OB proliferation on nanograined HA (67 nm average grain diameter) versus conventional HA (123 nm average grain diameter) is ~50% higher after 5 days.[54] Additionally, AP activity was ~50% higher and calcium deposition ~100% higher after 28 days *in vitro*.[54] This work suggests that the increase in surface roughness inherent to the decreased grain size is a contributing factor to this improvement in OB behavior. This is consistent with improved OB behavior shown with incidence of surface microroughing on various biomedical alloys, including Ti alloys[55,56] and 316L stainless steel,[57] bioactive glasses[58], HA and glass-reinforced HA[59] For example, microroughing induced by chemical etching in three different kinds of bioactive glass resulted in a ~60-300% increase in OB attachment after 2 hours.[58]

However, Webster et al. does not investigate how nano-grained *porous* ceramics affect OB behavior. We address this relationship in Chapters 3 - 4.

Chemical additions to HA during processing include the use of sintering aids, such as Na_3PO_4[60,61], and the substitution of silicon ions for phosphate ions in order to increase dissolution rate[62-65].

The inclusion of pores in HA scaffolds is important for successful bone tissue ingrowth and will be discussed in its own section.

MICROCRACKING

While experiencing the rigors of daily activity, bone undergoes repeated cyclic strain[66,67] The repetitive nature of this strain causes an accumulation of microcracks in the bone tissue.[46] The idea that this microdamage results from fatigue was originally presented by Frost[68], who also suggested that bone microdamage is related to bone remodeling.[68] Fatigue microdamage in bone likely triggers targeted bone remodeling,[69] which occurs near microdamage.[70-74]

Microcracks in bone were observed using various methods, including radiography[75] and fuschin or fluorescent dye staining with or without optical microscopy[68, 76-78] The dimensions of observed cracks were not always reported, but in those instances that they were these values varies based on location, species and the nature of activity undertaken by the patient. For example, microcracks found in human rib bones were between 296-404 μm in length with a crack opening displacement of 88-97 μm.[76] Microcracks found in equine subjects

had mean lengths between 37-60 μm, depending on the number of races the horses had undertaken.[77]

Chapters 5 - 7 of this dissertation addresses microcracking in HA as a property which may improve OB attachment. Originally observed as occurring intrinsically, microcracking was later controlled and induced in dense HA.

POROUS HYDROXYAPATITE FOR BONE TISSUE ENGINEERING

While unimodal porosity in HA is controlled by varying parameters such as the forces applied during cold or hot pressing, sintering time and sintering temperature, bimodal porosity requires more complex methods of fabrication. Bimodal porosity in HA is achieved in a number of ways, including foaming (used by our group[79]), by burning out a fugitive phase such as polymethyl methacrylate (PMMA)[80-81], the use of rapid prototyping to build up a periodic matrix, which does not mimic the natural structure of bone, but rather is comprised of orthogonal "struts" of HA[82], or by removing the organic component of natural cancellous bone, followed by conversion of the bone mineral into HA.[17-18]

As mentioned above, the inclusion of naturally-occurring pores and canals within bone is important in the transport of nutrients throughout the bone, as well as for communication between cells and innervation of the tissue.[2] An advantage of using a porous HA implant is that the interface available for cell attachment is far greater and more complex, resulting in an improved interlocking interface.[83] In comparison, a more dense material would offer a smooth interface with no available features with which the bone can ingrow.[16, 83] Pore sizes above 100 μm

lead to bone ingrowth, while sizes between 200-500 μm have been shown to optimize the vascularization of the new tissue.[15,16,83] This range of porosity includes interconnected pores, referred to as macropores, coupled with the interconnections themselves, called micropores. It is this interconnectivity that is key in promoting bone ingrowth and subsequent vascularization.[84] Bimodal interconnected porosity is detailed in our work with confocal laser scanning microscopy (CLSM) as a method for imaging cancellous bone and porous HA, included in Appendix A-B.

OVERALL AIMS

We chose to examine the effect of grain size, microcracking and grain boundary grooving in order to design a better bone tissue engineering scaffold. Such a scaffold would be bimodally porous and possess properties that improve cell behavior and tissue ingrowth. The aim of the first set of studies is to determine whether the observed relationship between nano-grained dense HA and improved OB attachment and growth translates into similar behavior in bimodally porous HA implants. The aim of the studies described in Chapters 5 - 8 is to investigate the role played, if any, by two different surface features on dense HA: microcracking and grain boundary grooving. Ultimately, should these features prove beneficial to OB behavior, they would be included in the design of an ideal porous scaffold.

REFERENCES

1. Sudo H, Kodama HA, Amagai Y, Yamamoto S, Kasai S. In vitro differentiation and calcification in a new clonal osteogenic cell line derived from newborn mouse calvaria. J Cell Biol 1983;96:191-198.

2. Young B, Heath JW. Wheater's Functional Histology. Edinburgh: Churchill Livingstone; 2000. 413 p.

3. Gray H. Gray's Anatomy. Philadelphia: Running Press; 1974. 1257 p.

4. Widmaier EP, Raff H, Strang KT. Vander Sherman and Luciano's Human Physiology: The Mechanisms of Body Function. McGraw Hill; 2004. 864p.

5. Manolagas SC, Spiess YH, Burton DW, Deftos LJ. Mechanism of action of 1,25-dihydroxyvitamin D3-induced stimulation of alkaline phosphatase in cultured osteoblast-like cells. Mol Cell Endocrinol 1983;33:27-36.

6. Ng KW, Partdridge NC, Niall M, Marten TJ. Epidermal growth factor receptors in clonal lines of a rat osteogenic sarcoma and in osteoblast-rich rat bone cells. Calcif Tissue Int 1983;35:298-303.

7. Berne RM, Levy MN, Koeppen BM, Stanton BA. Physiology. St. Louis: Mosby; 2004. 1014 p.

8. Xie J, Baumann MJ, McCabe LR. Osteoblasts respond to hydroxyapatite surfaces with immediate changes in gene expression. J Biomed Mater Res 2004;71A:108-117.

9. Shu R, McMullen R, Baumann MJ, McCabe LR. Hydroxyapatite accelerates differentiation and suppresses growth of MC3T3-E1 osteoblasts. J Biomed Mater Res 2003;67A:1196-1204.

10. Meganck JA, Baumann MJ, Case ED, McCabe LR, Allar JN. Biaxial flexure testing of calcium phosphate bioceramics for use in tissue engineering. J Biomed Mater Res 2005;72A:115-126.

11. Griffin MA, Smith IO, Baumann MJ. Comparison between primary and clonal osteoblast cells for in vitro attachment studies to hydroxyapatite. In: Sundar V, Rusin RP, Rutiser CA. Bioceramics: Materials and Applications V. Proceedings of the 106th Annual Meeting of The American Ceramic Society, Indianapolis, IN; 2004. p 83-89.

12. Laurencin CT, Khan Y. Bone graft substitute materials. eMedicine.com Inc. 2004; http://www.emedicine.com/orthoped/topic611.htm.

13. Cutter CS, Mehrara BJ. Bone grafts and substitutes. J Long Eff Med Implants 2006;16:249-260.

14. Lavernia CJ, Malinin TI, Temple HJ, Moryrea CE. Bone tissue allograft use by orthopedic surgeons. J Arthr 2004;19:430-435.

15. Jarcho M. Calcium phosphate ceramics as hard tissue prosthetics. Clin Ortho and Rel Res 1981;157:259-278.

16. Hench LL. Bioceramics: From concept to clinic. J Am Ceram Soc 1991;74:1487-1510.

17. Hing KA, Best SM, Tanner KE, Bonfield W, Revell PA. Quantification of bone ingrowth within bone-derived porous hydroxyapatite implants of varying density J Mater Sci: Mater Med 1999;10:663-670.

18. Hing KA, Best SM, Tanner KE, Bonfield W, Revell PA. Biomechanical assessment of bone ingrowth in porous hydroxyapatite J Mater Sci: Mater Med 1997;8:731-736.

19. Oonishi H, Hench LL, Wilson J, Sugihara F, Tsuji E, Matsuura M, Kin S, Yamamoto T, Mizokawa S. Quantitative comparison of bone growth behavior in granules of Bioglass, A-W glass-ceramic, and hydroxyapatite. J Biomed Mater Res 2000;51:37-46.

20. Ambrosio AMA, Sahoto JS, Khan Y, Laurencin CT. A novel amorphous calcium phosphate polymer ceramic for bone repair: I. Synthesis and characterization. J Biomed Mater Res B: Appl Biomat 2001;58;295-301.

21. Du C, Cui FZ, Feng QL, Zhu XD, deGroot K. Tissue response to nano-hydroxyapatite/collagen composite implants in marrow cavity. J Biomed Mater Res. 1998;42:540-548.

22. Du C, Cui FZ, Zhu XD, deGroot K. Three-dimensional nano-HAp/collagen matrix loading with osteogenic cells in organ culture. J Biomed Mater Res. 1999;44:407-415.

23. Sakane M, Mutsuzaki H, Miyanaga Y, Tanaka J, Ochiai N. Nano-composites of calcium phosphate-collagen promote osteoclast growth at the interface between tendons and bone tunnels in knee ligament reconstruction. In: The proceedings of the 7th World Biomaterials Congress, Sydney, Australia; 2004. p 385.

24. Wei J, Li Y, Chen W, Zuo Y. A study on nano-composite of hydroxyapatite and polyamide. J Mater Sci. 2003;38:3303-3306.

25. Wei J, Li Y, Peng X, Li Z. Injectable apatite and polymer biomimetic nano-composite cement for bone tissue engineering. In: The proceedings of the 7th World Biomaterials Congress, Sydney, Australia; 2004. p 1359.

26. Wei J, Li Y, Peng X, Li Z, Jing H. A study on tissue engineering scaffold material of nano-apatite and polyamide composite. In: The proceedings of the 7th World Biomaterials Congress, Sydney, Australia; 2004. p 827.

27. Cui FZ, Zhang W, Liao SS. Hierarchical self-assembling of nano-fibril of mineralized collagen for bone graft. In: The proceedings of the 7th World Biomaterials Congress, Sydney, Australia; 2004. p 1004.

28. Liao SS, Cui FZ, Zhang W, Feng QL. Hierarchically biomimetic bone scaffold materials: Nano-HA/collagen/PLA composite. J Biomed Mater Res 2004;69B:158-165.

29. Yoneda S, Guthrie WF, Bright DS, Khatri CA, Wang FW. In vitro biocompatibility of hydrolytically degraded poly(d,l-lactic acid). 7th World Biomaterials Congress, Sydney, Australia; 2004. p1324.

30. Fratzl P, Gupta HS, Paschalis EP, Roschger P. Structure and mechanical quality of the collage-mineral nano-composite in bone. J Mater Chem. 2004;14:2115-2123.

31. Hassenkam, T, Fantner, GE, Cutroni, JA, Morse DE, Weaver JC, Hansma PK.. High-resolution AFM imaging of intact and fractured trabecular bone. Bone 2004;35:4-10.

32. Longsworth J, Eppell SJ. Design and assembly of a sterile nanoscale orthopedic biomaterial. In: Biomaterials, proceedings of the northeast conference; 2002. p 173-174.

33. Legeros RZ. Properties of osteoconductive biomaterials: Calcium phosphates. Clin Orthop 2002;395:81-98.

34. Barrere F, Van Der Valk CM, Dalmeijer RAJ, Meijer G, Van Blitterswijk, CA, De Groot K, Layrolle P. Osteogenecity of octacalcium phosphate coatings applied on porous metal implants Source. J Biomed Mater Res 2003;66A:779-788.

35. Layrolle P, Barrere F, Van Der Valk CM, Meijer G, Dalmeijer RAJ, De Groot K. Osteointegration of biomimetic apatite coating applied onto dense and porous metal implants in femurs of goats. J Biomed Mater Res B Appl Biomat 2003;67:655-665.

36. Li P. Biomimetic nano-apatite coating capable of promoting bone ingrowth. J Biomed Mater Res 2003;66A:79-85.

37. Hossain M, Irwin R, Baumann MJ, McCabe LR. Hepatocyte growth factor (HGF) absorption kinetics and enhancement of osteoblast differentiation on hydroxyapatite surfaces. Biomaterials 2005;26:2595-2602.

38. Smith IO, Baumann MJ, Case ED. Induced microcracking affects osteoblast attachment on hydroxyapatite scaffolds for tissue engineering. Am J Biochem Biotechnol 2006;2:105-110.

39. Puleo DA, Nanci A. Understanding and controlling the bone-implant interface. Biomaterials 1999;20:2311-2321.

40. Crimp MJ, Oppermann DA, Doctor UU. *In Vitro* Stability Predictions for the Bone/Bioglass and Bone/HA Interactions. In: Bioceramics: Materials and Applications III. Proceedings of the 102nd Annual Meeting of The American Ceramic Society, St. Louis, MO; 2000. p 1-13.

41. Oppermann DA, Crimp MJ, Bement D. In vitro stability predictions for the bone/hydroxyapatite composite system. J Biomed Mater Res 1998;42:412-416.

42. Hogg R, Healy TW, Fuerstenau DW. Mutual coagulation of colloidal dispersions. Trans Faraday Soc 1966;66:490.

43. Kilpadi KL, Chang PL, Bellis SL. Hydroxylapatite binds more serum proteins, purified integrins, and osteoblast precursor cells than titanium or steel. J Biomed Mater Res 2001;57:258-267.

44. Ducheyne P, Qiu Q. Bioactive ceramics: the effect of surface reactivity on bone formation and bone cell function. Biomaterials 1999;20:2287-2303.

45. Lind M, Overgaard S, Bunger C, Soballe K. Improved bone anchorage of hydroxyapatite coated implants compared with tricalcium-phosphate coated implants in trabecular bone in dogs Source: Biomaterials 1999;20:803-808.

46. Park JB, Lakes RS. Biomaterials: An Introduction. New York: Plenum Press; 1992. 394p.

47. Balasundaram G, Sato M, Webster TJ. Using hydroxyapatite nanoparticles and decreased crystallinity to promote osteoblast adhesion similar to functionalizing with RGD. Biomaterials 2006;27:2798-2805.

48. Fujishiro Y, Hench LL, Oonishi H. Quantitative rates of in vivo bone generation for Bioglass and hydroxyapatite particles as bone graft substitute. J Mater Sci: Mater Med 1997;8:649-652.

49. Itoh D, Yoneda S, Kuroda S, Kondo H, Umezawa A, Ohya K, Ohyama T, Kasugai S. Enhancement of osteogenesis on hydroxyapatite surface coated with synthetic peptide (EEEEEEEPRGDT) in vitro. J Biomed Mater Res 2002;62:292– 298.

50. Durrieu MC, Pallu S, Guillemot F, Barielle R, Amedee J, Baquey CH, Labrugere C, Dard M. Grafting RGD containing peptides onto hydroxyapatite to promote osteoblastic cells adhesion. J Mater Sci: Mater Med 2004;15:779-786.

51. Webster TJ, Ergun C, Doremus RH, Siegel RW, Bizios R. Nanocrystalline hydroxyapatite enhances osteoblast function. In: Proceedings of the First Joint BMES/EMBS Conference, Atlanta, GA; 1999. p744.

52. Webster TJ, Siegel RW, Bizios R. Design and evaluation of nanophase alumina for orthopaedic/dental applications. Nanostruct Mater 1999;12:983-986.

53. Webster TJ, Siegel RW, Bizios R. Osteoblast adhesion on nanophase ceramics. Biomaterials 1999;20:1221-1227.

54. Webster TJ, Ergun C, Doremus RH, Siegel RW, Bizios R. Enhanced functions of osteoblasts on nanophase ceramics. Biomaterials 2000;21:1803-1810.

55. Silva CC, Pinheiro AG, de Oliveira RS, Goes JC, Aranha N, de Oliveira LR, Sombra ASB. Properties and *in vivo* investigation of nanocrystalline hydroxyapatite obtained by mechanical alloying. Mat Sci and Eng C. 2004;24:549-554.

56. Huang, J, Best, SM, Bonfield, W, Brooks RA, Rushton N, Jayasinghe SN, Edirisinghe MJ. *In vitro* assessment of the biological response to nano-sized hydroxyapatite. J Mater Sci: Mater M. 2004;15:441-445.

57. Yoneda, S, Guthrie, WF, Bright, DS, Khatri CA, Wang, FW. In vitro biocompatibility of hydrolytically degraded poly(d,l-lactic acid). In: The Proceedings of the 7th World Biomaterials Congress, Sydney, Australia; 2004. p1324.

58. Itala A, Ylanen HO, Yrjans J, Heino T, Hentunen T, Hupa M, Aro HT. Characterization of microrough bioactive glass surface surface: Surface

reactions and osteoblast responses in vitro J Biomed Mater Res 2002;62:404-411.

59. Prado da Silva MH, Lemos AF, Ferreira JMF, Lopes MA, Santos JD. Production of porous biomaterials based on glass-reinforced hydroxyapatite composites. Key Engin Mater 2002;230-232:483-486.

60. Kleebe HJ, Nakahira A, Pezzotti G. Microstructure and microcrack formation at phase boundaries in Na3PO4-doped hydroxyapatite. Nippon Seramikkusu Kyokai Gakujutsu Ronbunshi/J Ceram Soc Japan 2001;109:181-185.

61. Halouani R, Bernache-Assolant D, Champion E, Ababou A. Microstructure and related mechanical properties of hot pressed hydroxyapatite ceramics. J Mater Sci: Mater Med 1994;5:563-568.

62. Porter AE, Patel N, Skepper JN, Best SM, Bonfield W. Comparison of in vivo dissolution processes in hydroxyapatite and silicon-substituted hydroxyapatite bioceramics. Biomaterials 2003;24:4609-4620.

63. Porter AE, Best SM, Bonfield W. Ultrastructural characterisation of hydroxyapatite and silicon-substituted hydroxyapatite. Key Engin Mater 2003;240-242:505-508.

64. Porter AE, Botelho CM, Lopes MA, Santos JD, Best SM, Bonfield W. Ultrastructural comparison of dissolution and apatite precipitation on hydroxyapatite and silicon-substituted hydroxyapatite in vitro and in vivo. J Biomed Mater Res 2004;69A:670-679.

65. Porter AE, Patel N, Skepper JN, Best SM, Bonfield W. Effect of sintered silicate-substituted hydroxyapatite on remodelling processes at the bone-implant interface. Biomaterials 2004;25:3303-3314.

66. Lanyon LE, Hampson WGJ, Goodship AE, Shah JS. Bone deformation recorded in vivo from strain gauges attached to the human tibial shaft. Acta Orthop Scand 1975;46:256-268.

67. Burr DB, Milgrom C, Fyhrie DP, Forwood M, Nyska M, Finestone A, Hoshaw S, Saiag E, Simkin A. In vivo measurement of human tibial strains during vigorous activity. Bone 1996;18:405-410.

68. Frost HL. Presence of microscopic cracks in vivo in bone. Henry Ford Hospital Med Bull 1960;8:27-35.

69. Burr DB. Targeted and nontargeted remodeling. Bone 2002;30:2-4.

70. Burr DB, Martin RB, Schaffler MB, Radin EL. Bone remodeling in response to in vivo fatigue microdamage. J Biomech 1985;18:189-200.

71. Burr DB, Martin RB. Calculating the probability that microcracks initiate resorption spaces. J Biomech 1993;26:613-616.

72. Mori S, Burr DB. Increased intracortical remodeling following fatigue microdamage. Bone 1993;14:103-109.

73. Stepnik MW, Radtke CL, Scollay MC, Oshel PE, Albrecht RM, Santschi EM, Markel MD, Muir P. Scanning electron microscopic examination of third metacarpal/third metatarsal bone failure surfaces in thoroughbred racehorses with condylar fracture. Vet Surg, 2004;33:2-10.

74. Bronckers ALJJ, Goei W, Luo G, Karsenty G, D'Souza RN, Lyaruu, DM, Burger EH. DNA fragmentation during bone formation in neonatal rodents assessed by transferase-mediated end labelling. J Bone Miner Res 1996;11:1281-1291.

75. Blickenstaff LD, Morris JM. Fatigue fracture of the femoral neck. J Bone Joint Surg 1966;48A:1031-1047.

76. Lee TC, O'Brien FJ, Taylor D. The nature of fatigue damage in bone. Int J Fatigue 2000;22:847-853.

77. Da Costa Gomez TM, Radtke CL, Kalscheur VL, Swain CA, Scollay MC, Edwards RB, Santschi EM, Markel MD, Muir P. Effect of focused and radial extracorporeal shock wave therapy on equine bone microdamage. Vet Surg 2004;33:49-55.

78. Muir P, Johnson KA, Ruaux-Mason CP. In vivo matrix microdamage in a naturally occurring canine fatigue fracture. Bone 1999;25:571-576.

79. McMullen, R. An in vitro investigation of MC3T3-E1 osteoblast proliferation and differentiation on hydroxyapatite based tissue-engineered scaffolds. Masters Degree Thesis. Department of Chemical Engineering and Materials Science. Michigan State University, East Lansing, MI; 2004. 181p.

80. Flautre B, Descamps M, Delecourt C, Blary MC. Porous HA ceramic for bone replacement: role of the pores and interconnections - experimental study in rabbit. J Mater Sci: Mater Med, 2001;12:679-682.

81. Li SH, De Groot K, Layrolle P. Bioceramic scaffold with controlled porous structure for bone tissue engineering. Key Engin Mater 2002;218-220:25-30

82. Wilson CE, de Bruijn JD, van Blitterswijk CA, Verbout AJ, Dhert WJA. Design and fabrication of standardized hydroxyapatite scaffolds with a defined macro-architecture by rapid prototyping for bone-tissue-engineering research. J Biomed Mater Res 2004;68A:123-132.

83. Bucholz RW. Properties of osteoconductive biomaterials: calcium phosphates. Clin Orthop Relat Res 2002;395:81-98.

84. deGroot K. Effect of porosity and physicochemical properties on the stability, resorption, and strength of calcium phosphate ceramics. Ann N Y Acad Sci 1988;523:227-233.

CHAPTER 2

EXPERIMENTAL PROTOCOLS

I. Overview

This chapter is a detailed outline of all experimental procedures used in the studies contained in this dissertation, including that work which has been published previously.[1-3] It is divided into sections which each describe a general area of the work: cell culture and care, specimen fabrication and cell culture and finally quantitation. Within each section, each individual protocol is described. I have included an example of a statistical quantitation using actual data in Appendix C.

II. MC3T3-E1 osteoblast culture[1-3]

This section describes the basic cell culture protocol for the upkeep of MC3T3-E1 murine (mouse) osteoblasts (OBs). These protocols are vital prior to a specific trial, when they are used to expand the OB population to a number suitable for that study.

The stock media used in MC3T3-E1 OB culture is referred to as "complete" and consists of 90% alpha minimum essential media (α-MEM, Invitrogen, Carlsbad, CA) and 10% fetal bovine serum (FBS, Atlanta Biologicals, Lawrenceville, GA).

OBs were removed from the tissue culture substrates enzymatically, using 10% Trypsin-ethylenediaminetetraacetic acid (Trypsin-EDTA, Invitrogen, Carlsbad, CA).

A. Freezing cell stock

Long-term storage of OBs requires storage under extremely cold conditions. Prior to storage at -180°C (93 K), OBs must be quickly frozen. A suspension of 1,000,000 OBs in complete media is placed into a 50 ml centrifuge tube and spun in a centrifuge (3000 rpm, 10 minutes) to separate the cells from the media. The large number of cells included in each freezing batch takes into account an expected post-thaw survival rate of < 50%. This population results in a workable thawed batch cell population. The volume of suspension used here is irrelevant and varies depending on the cell population density. The complete media is removed by slowly pouring it into a waste container and 1.5 ml of freezing media is added. Freezing media contains 90% complete media and 10% dimethyl sulfoxane (DMSO). The OBs are then resuspended by pipetting up and down 10 times and transferred to a 2 ml cryovial (Corning, Wilkes-Barre, PA). Cryovials are placed into a -80°C (193 K) freezer for a period from a minimum of 12 hours up to 2 weeks. Twelve hours allows sufficient time for the cells to freeze, while the maximum time of 2 weeks prevents unnecessary loss of cell viability due to storage at a temperature higher than -180°C (93 K). Vials are then transferred to a liquid nitrogen (LN_2) storage tank (-180°C/ 93 K) for long-term storage.

B. Thawing from stock

Cell stock is kept at -180°C (93 K) for long-term storage (longer than 2 weeks). Cells are divided into groups of 1-million, each in a 1.5 ml polypropylene cryovial. Henceforth, each group of cells will be referred to as a vial.

Prior to each study, MC3T3-E1 murine osteoblasts were thawed from frozen stock by placing each vial between the hands and rolling it back and forth until thawed (approximately 2 minutes). Each vial was then submerged in 70% EtOH (prepared by combining 90%* EtOH [Sigma-Aldrich, St. Louis, MO] with enough RO water to yield a final concentration of 70%) for one minute, removed with long handled stainless steel forceps and placed onto a piece of dry cotton gauze to dry. Using a piece of gauze in each hand, each vial was then opened and poured into the center of a 100 mm polystyrene tissue culture plate (Petri dish).

Prior to the thawing procedure described above, complete media was warmed by placing the 500 ml stock bottle in a water bath at 37°C (310 K, normal body temperature) for approximately 15 minutes. Ten ml of complete media was then added to each culture dish containing the thawed contents of a cell vial.

After 24 hours, the complete media was removed by aspiration, non-adherent cells rinsed away by twice pipetting onto and removing 1X phosphate-buffered saline (PBS) from the culture plate surface, in order to eliminate dead cells from the counts, and the thawed OBs were removed from their plates,

* 100% EtOH (200 proof) is available but is not used in this case. This is due to the presence of benzyne in 200 proof EtOH, which is used as a stabilizing agent and is toxic to living cells.

counted and replated at 60,000 – 75,000 cells/culture dish. This density is sufficient for the plated cells to divide without reaching confluency.

C. Splitting/Feeding

The term "splitting" is used when an OB culture is removed from its substrate, divided into smaller groups and plated at a lower cell density. Healthy OBs are normally split every 2 – 3 days when using 100 mm cell culture plates. Experience shows that this time interval leads to a population suitable for splitting. It should be noted that more active cells (lower passage number) may split sooner than this. Cells are ready to be split when ~25 cells are visible in each field of view under the microscope (10x objective). This population is large enough to be nearing, but not at, cell confluency. Confluency is a state where adjacent cells are touching each other, and may lead to subcloning of the cells.

Plates selected for splitting are moved to the biosafety cabinet (positive pressure, HEPA filtered, officially certified) and their media removed by aspiration. Aspiration uses a narrow glass tube (9 inch Pasteur pipette) connected to the central vacuum system draining into a 4 liter waste flask. Once the media is removed, the plate is rinsed twice with sterile 1X PBS and 2 ml of a 1:1 mixture of Trypsin-EDTA and complete media *per plate* in order to free the OBs from the culture surface. This process takes less than 2 minutes and is assisted by rocking the plate back and forth and side to side (90° apart) several times. Finally, the newly liberated cells are pipetted in suspension, up and down five times, washing the entire surface of the plate. OBs from each plate are

combined in a 50 ml centrifuge tube prior to counting. Typically, a batch from 10 – 20 plates will yield 1.5 – 2 million cells. This population is then partially plated (~20 plates) and partially frozen (1 – 2 cryovials). For lower passage cells, the amount that is frozen is ~ 90%, in order to preserve cell stock.

Cells are counted with a hemacytometer and replated at 60,000 – 75,000 per 100 mm plate. Ten ml of complete media is added to each plate and they are placed into the incubator at 37°C (310 K) and 5% CO_2 and the process repeated.

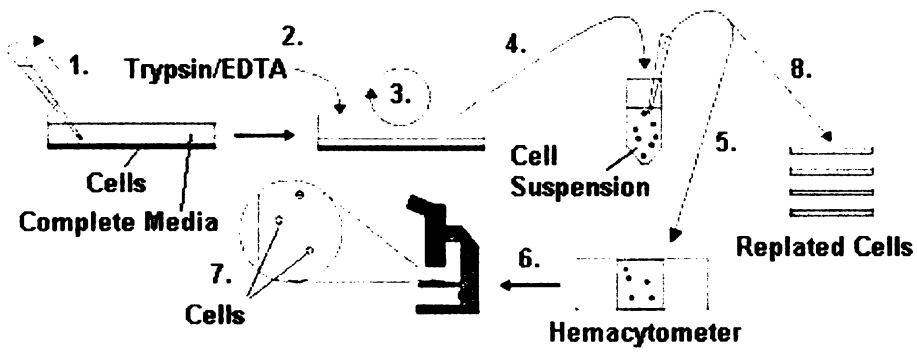

Figure 1: Schematic detailing the cell splitting process. Media is removed by aspiration **(1)** and the cells are rinsed twice with 1x PBS. Trypsin/EDTA and complete media are added in a 1:1 ratio **(2)** and each plate is rocked back and forth **(3)** to aid in cell detachment. Detached cells are pipetted away and placed into a 50 ml centrifuge tube, along with the cells from other plates **(4)**. 10 μl of this suspension is placed into each of the two sides of a hemacytometer **(5)**. Cells are then viewed under the optical microscope **(6)** and the cells counted **(7)**. Using this cell population data, the remaining cell suspension is divided up between fresh plates (60,000 – 75,000 per plate) and 10 ml fresh complete media added to each **(8)**.

III. Specimen fabrication:

This section will be divided into two subsections, one for porous and another for dense hydroxyapatite (HA). Further divisions will detail the various steps taken to create specific sample types.

A. Porous hydroxyapatite scaffolds[1]

Two groups of porous scaffolds were fabricated by foaming using hydroxyapatite (HA) with two different average particle sizes (diameter).

Micron scale HA powder was obtained from Hitemco Medical (Old Bethpage, NY) and had a manufacturer-reported particle size of 10 μm. This powder was used in its as-received form. As received powder arrived sintered.

Porous specimens were formed by first suspending HA powder in a 10^{-3} M aqueous solution of KNO_3. Powder and electrolyte were combined in a beaker and mixed with a stainless steel spatula. A typical batch of suspension would consist of 33 g of HA and 17 ml of KNO_3 solution. This ratio yielded a suspension of suitable consistency (similar to pancake batter) for eventual casting of cylinders. To this suspension, 1.8 ml of 30% H_2O_2 was added as the foaming agent and the suspension stirred once again. This electrolyte was used because it aids in the dispersion of HA powder particles by creating a large double layer thickness ($1/\kappa$), resulting in uniform porosity across the cylindrical specimens.[4]

The HA + H_2O_2 slurry was scooped into cylindrical silicone molds, each with a diameter of 15 mm. These molds were fabricated out of a two-part silicone kit (SI-25 SIL-MOLD, Hyperlast North America, Chattanooga, TN) and consisted of two pieces. The main piece contained the cylindrical mold chambers and the second piece was placed underneath, to prevent the slurry from dripping out. Each mold was covered with aluminum foil and placed into a gravity convection oven (Lindberg/Blue) at 125°C (398 K) for one hour. This time and temperature combination effectively dried the specimens sufficiently prior to sintering. Each

batch of suspension yielded approximately 6 green (unfired) specimens with a diameter of 1.5 cm and a length between 2 and 4 cm.

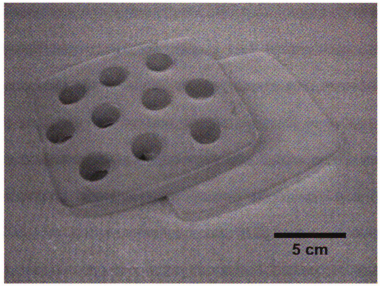

Figure 2: Silicone mold used for the foaming and casting of cylindrical porous HA scaffolds. Both pieces are shown, including the main piece with its cylindrical mold chambers and the solid base piece.

After one hour, these green HA specimens were gently ejected from their mold. In most cases, this was accomplished by carefully lifting the main piece of each mold away from the base, allowing the cylinders to remain behind. In some cases though, the HA cylinders would remain in their mold. To eject these HA specimens, the flat end of a syringe plunger was used and gentle pressure applied to eject each specimen out. The green HA specimens were then placed into a high-purity Al_2O_3 sintering dish, with Al_2O_3 cover, and immediately sintered in air at 1360°C (1633 K) for four hours, with a heating/cooling rate of 10°C/minute. This sintering time and temperature produces a specimen that is chemically HA and the prescribed heating/cooling rate prevents thermal shock,

both in the specimens and in the furnace heating elements. Sintering was performed immediately in order to maintain residual moisture in the green specimens. This moisture allows the particles to remain in their post-foamed positions and leads to a final product with structural integrity and consistent pore structure. Sintering was completed using a high temperature CM Rapid Temp sintering furnace (CM, Bloomsfield, NJ) equipped with molydisilicide heating elements.

Sintered specimens were sectioned into 1 mm slices using a Buehler Isomet 1000 diamond abrasive wafering saw (Buehler, Lake Bluff, IL, USA) operated at 200 rpm and reverse osmosis (RO) water as a lubricant. Each cylinder was gripped using a custom fabricated padded aluminum specimen holder and slice thickness was determined using the built-in controls of the saw.

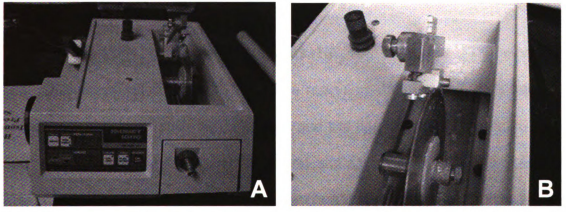

Figure 3: Figure 3A is a view of the Buehler Isomet 1000 wafering saw used to section the porous cylinders. Figure 3B is a close-up of the custom-built chuck used to hold each cylinder during cutting.

Nano-scale HA powder with a manufacturer reported average particle size of 20 nm was purchased from Berkeley Advanced Biomaterials (San Leandro,

CA, USA). The powder arrived in an ammonium hydroxide suspension, which was subsequently centrifuged (3000 rpm, 10 minutes) to separate the powder. The nano HA was then resuspended in 90% stock EtOH, centrifuged at 3000 rpm for 10 minutes and vacuum dried for 12 hours at room temperature in a vacuum furnace (IsoTemp 280A, Thermo Fisher, Watham, MA). This method of separating the powder was prescribed by the manufacturer.

Foaming and sintering were accomplished in the same manner described above for micron HA powder, with some specific exceptions. First, each batch of nano HA slurry contained 22 g of HA powder and 18 ml of 10^{-3} M KNO_3. This ratio yielded the desired consistency for foaming and casting of cylindrical scaffolds. Second, green specimens were sintered at 1100°C (1373 K) for one hour with a 10°C/min heating/cooling rate, using the same CM high temperature furnace. This sintering time and temperature has been used in the past to successfully yield nano-grained HA.[5-10]

The average grain size in porous HA scaffolds was determined by scanning electron microscopy (SEM). Five representative images were taken of both micron and nano-scale HA scaffolds and the line-intercept method (n = 50) used to determine average grain size and standard deviation. Pore size was determined using the same method. Specimen porosity was determined using Archimedes method with n = 5 for both micron and nano-scale HA scaffolds. Sample size is chosen to aid in observing any variances in porosity between specimens.

B. Dense hydroxyapatite[2,3]

Dense discs were fabricated using medical-grade HA powder (Taihei Chemical, Osaka, JP) with vendor-reported mean particle diameter of 1 – 3 μm. HA powder was uniaxially pressed into discs at 35 MPa for 1 minute using a hydraulic press (Carver Inc, Wabash, IN) and KBr pellet die (International Crystal Laboratories, Garfield, NJ). This force/time combination yielded green specimens with uniform density and minimal incidence of breakage. The resulting discs had a diameter of 32 mm and were 2 – 3 mm thick. These discs were placed in a single layer inside of Al_2O_3 sintering boats and sintered in air at 1360°C (1633 K) for 4 hours with a heating/cooling rate of 10°C/min (CM furnace) and the resulting HA discs were typically 23 mm in diameter and 1 – 2 mm thick, with a >99% theoretical density. These sintering specifications yield specimens determined to be HA and this thickness led to minimal warping.

Average grain size for dense HA specimens were determined using SEM and the same line intercept technique described in the previous section. Specimen density was calculated by comparing actual specimen mass for their measured volume (n = 5) to theoretical values expected for that volume.

Any macroscopic imperfections on the HA discs were ground flat using 30 μm (600 grit) SiC wet abrasive paper (Carbimet 8" abrasive discs, Buehler, Lake Bluff, IL) using a sequence including 5 minutes each at 30 μm, 12 μm, 9 μm, 6 μm and 1 μm diamond abrasive suspension or paste. Grinding and polishing were performed with a Buehler EcoMet 3 variable speed grinder/polisher equipped with an AutoMet 2 power head. After polishing, specimens were

ultrasonically cleaned by submersion in reverse osmosis (RO) water and pulsing with an ultrasonic probe at 20 kHz and 250 watts for 5 minutes.

In both microcracking and grain boundary grooving studies, control specimens were dense HA discs with average grain sizes equal to those of the non-control specimens. These HA discs were also polished, sterilized and seeded in identical fashion to the microcracked and grain boundary grooved specimens.

Microcracks were induced by systematically indenting each specimen 196 times (14 x 14 grid with 1 mm spacing) using a Buehler Micromet II microindentor (Buehler, lake Bluff, IL), with a load of 4.9 N, a load time of 5 seconds and a loading rate of 70 μm/sec.[2,3] We found these indentation parameters to induce microcracks with minimal spalling and chipping of the HA specimens. Microcracks were formed on the HA surface by the radial cracks originating from the corners of each indentation impression. Indent spacing was assured by turning the stage micrometer two full turns, equaling 1 mm, between each indent.

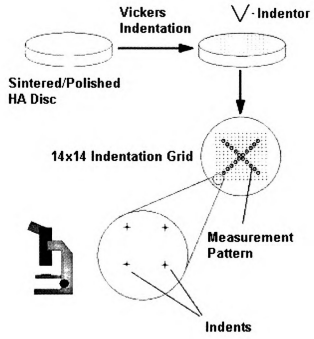

Figure 4: Schematic of indentation/induced microcracking and viewing/measuring of microcracks using optical microscopy. Indents selected for measurement ("X" pattern) are indicated by circles.

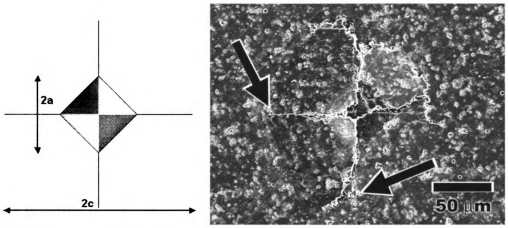

Figure 5: The image at left is a schematic of a typical Vickers indentation. The length "2a" is the width of the indentation pyramid and "2c" is the length of a microcrack. The image at right is an SEM micrograph of a single indentation on the surface of a dense sintered HA specimen. The black arrows indicate microcracks. Figure taken from Smith et al.[3]

In order to accelerate crack growth saturation, each HA disc was submerged in RO water for 8 hours after indentation.[3] The average indentation size and crack size were then determined by optical microscopy by measuring a

representative selection of indentations (n = 20) for each HA specimen. These indents were taken in a pattern resembling a large "X" across the entire specimen surface (See Figure 4).

Thermal etching was used to induce grain boundary grooving in HA in order to determine its effect on OB attachment. Polished HA discs were heated to 1100°C (1373 K) for 45 minutes, with a heating/cooling rate of 10°C/minute. SEM was used to determine whether etching was successful and to estimate the width of the grain boundary grooves, using AnalySIS software (Olympus Soft Imaging Solutions Corp Lakewood, CO). Due to its magnitude, the depth of these grooves could not be estimated using SEM.

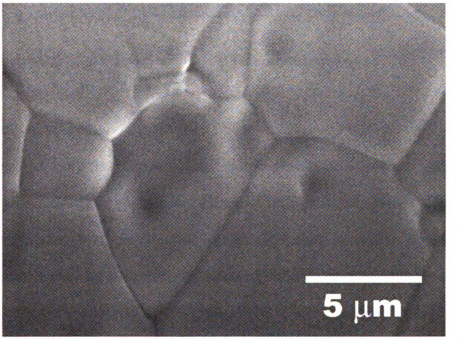

Figure 6: SEM micrograph taken at the surface of a sintered dense HA specimen that has been thermally etched at 1100°C (1373 K) for 45 minutes to induce grain boundary grooving.

The average surface roughness (R_a) was measured using a Veeco DEKTAK 6M profilometer, with a stylus radius of 2.5 μm and a measurement length of 3000 μm. Three measurements were taken on the specimen surface, to determine average R_a and standard deviation.

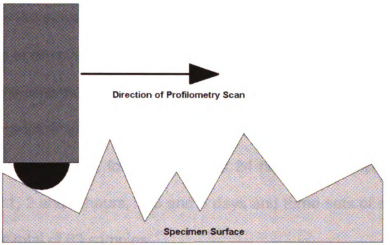

Figure 7: Schematic of a profilometry scan across the specimen surface.

IV. Cell culture/counting:

This section is divided into subsections, for porous and dense hydroxyapatite. Since cell culture, imaging and counting protocols used for microcracked and thermally etched (grain boundary grooved) hydroxyapatite were the same, they have both been included under "dense hydroxyapatite".

Prior to cell culture, all HA specimens were sterilized using the same protocol. Specimens were sterilized by steam autoclave (Tuttnauer, Hauppauge, NY) at 125°C (398 K) for 45 minutes with 30 minutes drying time. Specimens

were placed into beakers, which were covered with aluminum foil and were autoclaved in the absence of any other materials.

A. Porous hydroxyapatite[1]

MC3T3-E1 subclone 7 OBs of passages 22-23, cultured in complete media were seeded across the surface of both micron and nano-scale porous HA scaffolds inside of Al collars at 11,320 cells/cm^2 and incubated in air at 37°C (310 K), 5% CO_2 and high humidity. Subclone 7 cells were used because they are known to differentiate into OBs (Reported by supplier). Complete media was replenished every two days, following the first 24 hours. Three specimens were seeded at 0.5, 1, 2 and 4 hours, 1, 3 and 5 days and three sets of cultures were examined, for a total of 63 samples.

OB attachment was assessed at intervals of 0.5, 1, 2 and 4 hours and OB proliferation at 1, 3 and 5 days. Prior to cell counting, scaffolds were removed, placed into separate wells, rinsed twice with 1x phosphate-buffered saline (PBS), trypsin/EDTA: complete media (1:1, a ratio which allow detachment at a sufficient rate) added and the scaffolds morselized to facilitate OB detachment, using a mortar-and-pestle motion with the handle end of a cell scraper. Ten µl of cell suspension was pipetted from the center of each well and placed into each of the two sides of a hemacytometer for counting.

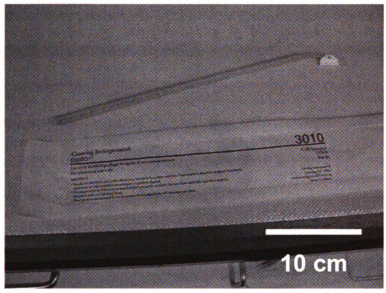

Figure 8: The cell scraper used to morselize porous HA scaffolds prior to counting attached OBs. The handle end, located at the left end of the photo, was placed into each well and the specimen morselized.

Statistical differences in OB counts on micron and nano-scale HA scaffolds were determined by using the Student's t-test. This test is useful in determining significance in the difference between means of two groups. A p value of 0.05 or lower was considered to be significant. This level of p value is commonly associated with significance.

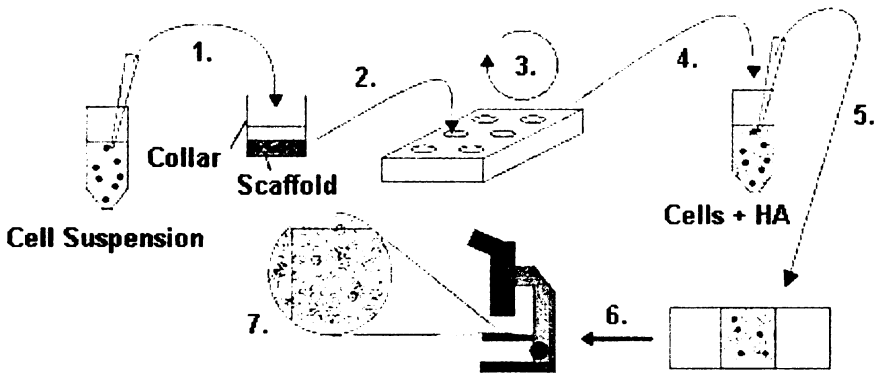

Figure 9: Schematic showing the process of counting cells on porous HA scaffolds. Cells are removed from their tissue culture plates **(1)** and seeded onto sterile porous HA scaffolds, placed inside of Al foil collars **(2)**. Each collared scaffold is placed into a 6-well polystyrene tissue culture plate and into the incubator for the prescribed time. After incubation, each specimen is removed from its collar and placed into a fresh 6-well plate, rinsed twice with 1x PBS, exposed to Trypsin/EDTA and the scaffold morselized with the handle end of a cell scraper **(3)**. 10 μl of the resulting suspension is placed into each of the two sides of the hemacytometer **(4)** and the cells (with HA particles) are viewed under the optical microscope **(6)** and counted **(7)**.

Issues which arose while using the hemacytometer for cell counting are addressed in detail in Chapter 4. In short, we attempted to correct the error observed in our cell counts by subtracting away background HA particles. This involved repeating the above procedure without the cells present. Morselized scaffolds were placed into the hemacytometer and false-positive "cells" were counted. If a particle resembled a cell, as it appeared during a normal cell count with scaffold particles present, it was tallied.

In future studies, cells should be counted by first staining to differentiate them from the surrounding scaffold particles and then by counting, either directly by optical microscopy or confocal laser scanning microscopy (CLSM), or indirectly by spectrophotometry.

B. Dense hydroxyapatite[3]

MC3T3-E1 subclone 14 OBs were obtained from ATCC (Manassas, VA). Sterile microcracked HA and control HA specimens were placed into Al collars inside 6-well polystyrene cell culture plates and OBs were seeded onto the HA discs at a density of 11,320 cells/cm^2. Two separate trials were conducted for incubation times of 1 and 4 hours each. OB seeding was done on specimens in triplicate, with n = 3 for a total of nine microcracked HA and nine control HA specimens for each trial. The triplicate model is commonly used to improve statistical significance for *in vitro* cell culture studies. The same protocol was used for seeding OBs onto grain boundary grooved (and corresponding control) HA specimens. The only difference is that MC3T3-E1 subclone 7 cells were used instead.

In both microcracking and grain boundary grooving studies, OBs were fixed using 3.7% formaldehyde (H_2CO) (JT Baker, Phillipsburg, NJ) in order to terminate the life cycle and preserve the physical state of the cells prior to their death, as well as permeabilized with a solution of 0.1% Triton X-100 (Sigma-Aldrich, St. Louis, MO) to open the cell membranes. Prior to staining, OB-seeded HA specimens were pre-incubated in 1% bovine serum albumin (BSA, Invitrogen). Pre-incubation improves the uptake of Rhodamine-Phalloidin into the cells.

The actin cytoskeletin was stained using Rhodamin-Phalloidin while the nucleus was stained using Hoescht 3342 (Invitrogen). These stains penetrate the cell membrane and selectively stain particular organelle (in this case the

cytoskeleton and nucleus, respectively). Stained OB-seeded HA specimens were mounted in glycerol solution (JT Baker) to seal the specimen surfaces from the air, and viewed using a Leica DM IL fluorescence microscope (Leica Microsystems, Wetzlar, GER) and optical micrographs recorded using the Spot RT camera system (Diagnostic Instruments, Inc. Sterling Heights, MI). Rhodamine-Phalloidin stain fluoresces at a wavelength of 565 nm when exposed to light of a wavelength of 542 nm while the Hoescht stain fluoresces at a wavelength of 465 nm when exposed to light with wavelength equal to 355 nm.

For the microcracking study, OB attachment was quantified by counting OB nuclei over the microscope's field of view (h = 1000 μm, w = 1500 μm). Ten fields of view were selected and counted for each specimen and the Student's t-test was used to determine statistical significance, with $p < 0.05$ taken as significant. A similar protocol was used for the grain boundary grooving study, with the only difference being that 20 fields of view were selected per specimen.

The effect of induced microcracking in HA specimens on OB morphology was assessed by staining the actin fibers and observing the OB shape using optical fluorescence microscopy. Actin fibers are a component of the cytoskeleton and spread throughout the cell, following its shape.

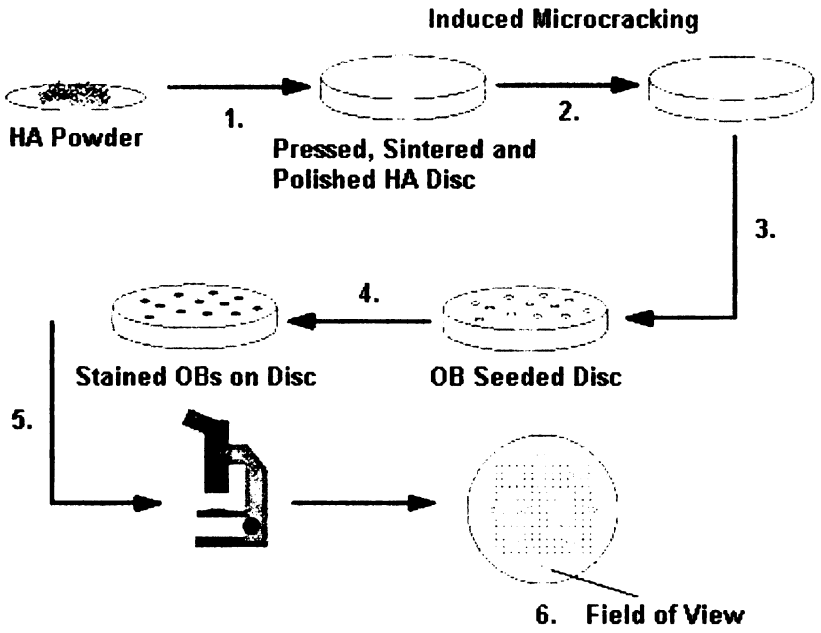

Figure 10: Schematic showing the process of fabricating, microcracking, cell seeding, staining and counting on dense HA. Powder is uniaxially pressed, sintered and polished **(1)** prior to induced microcracking **(2)**. Microcrack size is determined, the specimens sterilized and OBs are seeded onto their surfaces **(3)**. Following culture times of one and four hours, the OBs are stained with Rhodamine/Phalloidin and Hoescht **(4)** and viewed under an optical fluorescence microscope **(5)**. Fields of view are chosen as shown (grey boxes each indicate one field of view) **(6)**.

REFERENCES

1. Smith IO, McCabe LR, Baumann MJ. MC3T3-E1 Osteoblast attachment and proliferation on porous hydroxyapatite scaffolds with nanophase powder. Int J Nanomed 2006;1:189-194.

2. Case ED, Smith IO, Baumann MJ. Microcracking in hydroxyapatite and the implications for bone tissue engineering. Mater Sci Engin A 2005;390:246-254.

3. Smith IO, Baumann MJ, Case ED. Induced microcracking affects osteoblast attachment on hydroxyapatite scaffolds for tissue engineering. J Am Biochem Biotechnol, 2006;2:105-110.

4. Hiemenz PC, Rajagopalan R. Princliples of colloid and surface chemistry. New York: Marcel Dekker; 1997. 650p.

5. Webster TJ, Ergun C, Doremus RH, Siegel RW, Bizios R. Nanocrystalline hydroxyapatite enhances osteoblast function. In: Proceedings of the First Joint BMES/EMBS Conference, Atlanta, GA; 1999. p744.

6. Webster TJ, Ergun C, Doremus RH, Siegel RW, Bizios R. Enhanced functions of osteoblasts on nanophase ceramics. Biomaterials 2000;21:1803-1810.

7. Webster TJ, Ergun C, Doremus RH, Siegel RW, Bizios R. Specific proteins mediate enhanced osteoblast adhesion on nanophase ceramics. J Biomed Mater Res 2000;51:475-483.

8. Webster TJ, Siegel RW, Bizios R. Design and evaluation of nanophase alumina for orthopaedic/dental applications. Nanostruct Mater 1999;12:983-986.

9. Webster, TJ, Siegel, RW and Bizios, R. Osteoblast adhesion on nanophase ceramics. Biomaterials 1999;20:1221-1227.

10. Webster TJ, Siegel RW, Bizios R. Nanoceramic surface roughness enhances osteoblast and osteoclast functions for improved orthopaedic/dental implant efficiency. Scripta Mater 2001;44:1639-1642.

CHAPTER 3

MC3T3-E1 OSTEOBLAST ATTACHMENT AND PROLIFERATION ON POROUS HYDROXYAPATITE SCAFFOLDS FABRICATED WITH NANOPHASE POWDER

IAN O. SMITH[1], LAURA R. MCCABE[2] AND MELISSA J. BAUMANN[1]
[1]Department of Chemical Engineering and Materials Science, Michigan State University, East Lansing, MI, USA
[2]Department of Physiology, Michigan State University, East Lansing, MI, USA

PUBLISHED IN: Int J Nanomed 2006;1:189-194.

ABSTRACT

Porous bone tissue engineering scaffolds were fabricated using both nano hydroxyapatite (nano HA) powder (20 nm average particle size) and micro HA powder (10 μm average particle size), resulting in sintered scaffolds of 59 vol% porosity and 8.6 ± 1.9 μm average grain size and 72 vol% porosity and 588 ± 55 nm average grain size, respectively. Scanning electron microscopy (SEM) was used to measure both the grain size and pore size. MC3T3-E1 osteoblast (OB) attachment and proliferation on both nano HA and micro HA porous scaffolds was quantified. As expected, OB cell number was greater on nano HA scaffolds compared to similarly processed micro HA scaffolds 5 days after seeding, while OB attachment did not appear greater on the nano HA scaffolds ($p < 0.05$).

INTRODUCTION

Bone is a composite material having a calcium phosphate (CaP) mineral component and a collagen-based organic matrix. CaP is a bioceramic resembling hydroxyapatite (HA, $Ca_{10}(PO_4)_6(OH)_2$), where the individual crystals have a plate-

like morphology, 15 - 200 nm in length and 10 – 80 nm in width with a thickness between 2 and 7 nm. (Fratzl et al, 2004) These apatite crystals are imbedded within the collagen fiber component of the organic matrix, which forms lamellar sheets comprising the concentric rings of osteons in cortical bone (Young and Heath, 2000) and the more woven structure of trabeculae in cancellous bone. (Hassenkam et al, 2004) The collagen matrix is composed primarily of Type I collagen fibers of approximately 100 nm in diameter. (Fratzl et al, 2004)

These nano-components play an active role in bone development and growth. Collagen fibers act as the scaffold on which newly formed nanocrystals of bone apatite form and grow, leading eventually to the formation of woven bone. This primitive early phase of bone is eventually replaced by the lamellae of adult bone. (Young and Heath, 2000) Additionally, collagen fibers have been shown to incorporate into porous HA tissue engineering scaffolds where the interfacial zone between bone and scaffold has been found to be a nano HA-reinforced collagen matrix. (Chen et al, 2004)

One area of current research in biomimetic nano-scale ceramic bone substitute materials is therefore focused on the design of nanoscale ceramic/polymer composites to mimic some of the morphological features of natural bone. These systems can be grouped into three categories: nano-CaP/collagen (Du et al, 1998; Du et al, 1999; Sakane et al, 2004), nano-CaP/non-collagen polymer (Wei et al, 2003; Wei et al, 2004a; Wei et al, 2004b) and a combination of the two (Cui et al, 2004; Liao et al, 2004). Although there are several types of CaP bioceramics, HA is the most commonly used, having a

chemistry that closely matches normal bone apatite. (Hench, 1998; Jarcho, 1981; Li et al, 2004)

Nanocrystalline HA has been shown to be biocompatible with a minimal inflammatory response (Silva et al, 2004), (Huang et al, 2004), although there is a potential for cytotoxicity. (Huang et al, 2004) While some engineered nanoCaP/polymer composites such as HA/collagen polylactic acid (PLA) scaffolds from Liao et al reported improvements in compressive strength using nano HA, they did not replicate the hierarchical structure of bone which may be crucial in encouraging bone ingrowth into a tissue engineered scaffold. (Du et al, 1998; Liao et al, 2004) Also, Yoneda et al. confirm that the degradation of PLA adversely affects cell behavior specifically, that increased degradation leads to a decrease in cell spreading, adhesion and cell survival. (Yoneda et al, 2004) Therefore, current research focuses on developing a bioceramic with a morphological structure similar to normal bone to promote bone regeneration *in vitro* and *in vivo*. (Longsworth and Eppell, 2002)

Webster et al compared changes in osteoblast (OB) behavior on nano-grained versus micro-grained dense bioceramics, including Al_2O_3, TiO_2 and HA, demonstrating increases in OB attachment (Webster et al, 1999a; Webster et al, 1999b; Webster et al, 1999c) and proliferation (Webster et al, 1999a; Webster et al, 2000a), alkaline phosphatase (AP) activity (Webster et al, 1999a; Webster et al, 2000a) and calcium deposition (Webster et al, 1999a; Webster et al, 2000a), as well as decreased cell motility (Webster et al, 1999a; Webster et al, 2000a).

Osteoblast attachment on a bioinert ceramic like Al_2O_3 can be attributed to the presence of physical surface irregularities that lead to increased morphological fixation. (Hench, 1998) Such fixation in turn plays an important role in the use of TiO_2 as a coating for orthopedic implants, improving the integrity of the implant/bone interface. (Areva et al, 2004) Fixation also plays a role in OB attachment to HA, but increased osteoblast adhesion may also occur because of improved protein interactions that have been linked to decreases in grain size.[25]

Enhanced OB behavior for HA having a finer grain size is further illustrated in a study by Xie et al, which recently reported that MC3T3-E1 OBs seeded onto dense HA discs showed differences in gene expression related to grain boundary surface area. (Xie et al, 2004) Gene expression of OBs on HA discs fabricated with an average particle size of 35 μm showed a decrease in cellular metabolism and an increase in differentiation while HA discs processed from smaller particle sizes (~11 μm) showed gene expression profiles that signified increased cell growth. Each of the previous studies was conducted using dense ceramic scaffolds, designed specifically for cell culture purposes, while the current study assesses whether porous bone replacement scaffolds fabricated with nano HA powder rather than micro HA improves OB attachment and proliferation.

MATERIALS AND METHODS

HA powder, of 10 μm average particle size, was purchased from Hitemco Medical (Old Bethpage, NY, USA) and used in its as-received form. Nano-scale HA powder having an average particle size of 20 nm was purchased from Berkeley Advanced Biomaterials (San Leandro, CA, USA). The nano HA powder arrived in an ammonium hydroxide suspension which was subsequently centrifuged, resuspended in ethanol, centrifuged again to separate out the nano HA powder and then vacuum dried for 12 hours before use (per manufacturer instructions).

Methods used in this study can be divided into four parts: scaffold fabrication, imaging of scaffold surfaces, osteoblast cell culture and assessment of OB attachment and proliferation.

Porous cylindrical samples of each HA powder particle size were foamed by suspending the HA powders in KNO_3 electrolyte to which H_2O_2 had been added, pouring the resulting foamed suspension into cylindrical molds and drying at 125°C. The dry, green HA samples were then sintered at 1100°C for 1 hour (nano HA) following the procedure established by Webster et al. (Webster et al, 1999a; Webster et al, 2000a; Webster et al, 2000b) or 1360°C for 4 hours (micro HA) using a protocol (McMullen, 2004) developed by McMullen. Both the micro and nano HA sintered scaffolds were next sectioned using a Buehler IsoMet 1000 diamond abrasive wafering saw (Buehler, Lake Bluff, IL, USA) into discs of approximately 1 mm thickness and autoclaved.

Nano HA and micro HA scaffold surfaces were observed using scanning electron microscopy (SEM). Samples were coated with a thin layer of Au, approximately 21 nm thick, using an Emscope SC500 sputter coater (Emscope Laboratories Ltd, Ashford, UK), mounted onto Al stubs and imaged using a JEOL 6400 SEM (JEOL Corporation, Tokyo, Japan) operated at an accelerating voltage of 5 keV. SEM photomicrographs were collected and exported using the AnalySIS software package.

MC3T3-E1 OBs of passage 22-23, cultured in alpha Minimum Essential Medium (α-MEM) supplemented with 10% Fetal Bovine Serum (FBS), were trypsinized, resuspended in α-MEM and seeded evenly across the surface of porous HA scaffolds at a density of 11,320 cells/cm^2 and incubated in air at 37°C (310 K), 5% CO_2 and high humidity. (Shu et al, 2003) 2 ml of α-MEM was added per specimen and was replenished every two days. Three specimens were statically cultured per time interval and two sets of cultures were examined, resulting in 6 samples per time interval. MC3T3-E1 OBs are a widely used OB cell line (Cerroni et al, 2002; Iyer et al, 2004; Shu et al, 2003; Werner et al, 2002; Xie et al, 2004) that have been shown to behave in a similar manner to primary OBs. (Griffin et al, 2005)

OB attachment was assessed at intervals of 0.5, 1, 2 and 4 hours. Scaffolds were removed, placed into separate wells, rinsed with phosphate-buffered saline (PBS), trypsin/α-MEM (50/50) added and the scaffolds morselized to facilitate osteoblast detachment. Media was drawn from each well

and the OBs counted using a hemacytometer. OB cell counts were also conducted at 1, 3 and 5 days following attachment to assess OB proliferation.

Statistical differences between attachment and differentiation on micro HA and nano HA scaffolds were calculated using the Student *t* test. A *p* value of 0.05 or lower was considered to be significant.

RESULTS

Porous HA scaffolds were successfully fabricated by foaming and sintering both micro HA and nano HA powder as described in the previous section. SEM showed that the micro HA scaffolds have a grain size of 8.6 μm ± 1.9 μm which is approximately 15 times greater than the nano HA grain size of 588 nm ± 55 nm, (representative micrographs given in Figure 1). The average grain size was determined using a line-intercept method (n = 50) based on ASTM standard E 112.[33] The volume porosity of micro HA and nano HA scaffolds using Archimedes method were found to be 59 vol% and 72 vol %, respectively.[27] Both micro and nano HA scaffold surfaces consisted of grains which are the sintered particles interspersed with frequent gaps along with larger macropores/micropores of 390 μm ± 210 μm/ 38 μm ± 22 μm for micro HA and 480 μm ± 275 μm/ 30 μm ± 21 μm for nano HA. These size ranges fall within standard macropore (200-400 μm) and micropore (<60 μm) ranges reported by deGroot et al. (deGroot et al, 1988) A representative SEM photomicrograph

showing the nature and distribution of the porosity within the pore wall of a nano HA scaffold is given in Figure 2.

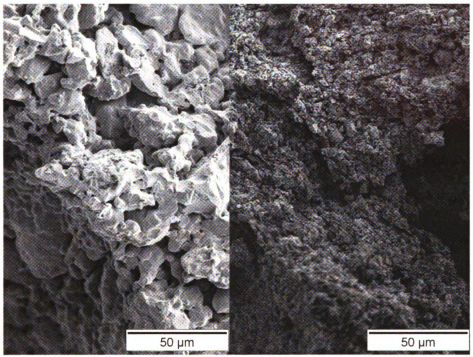

Figure 1: Comparison of SEM micrographs of the surface of scaffolds fabricated using micro HA (left) and nano HA (right).

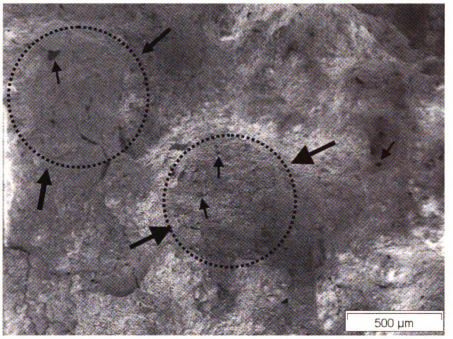

Figure 2: SEM micrograph showing the surface of porous scaffold fabricated using nano HA, including macropores (large arrows noting approximate boundary of a macropore) and micropores (small arrows emphasizing the <60 µm interconnecting pores).

Contrary to published data by Webster et al using dense HA scaffolds, these results show that initial OB attachment does not increase as a function of decreased grain size on porous HA scaffolds. (Webster et al, 1999a; Webster et al, 2000a; Webster et al, 2000b; Webster et al, 2001) MC3T3-E1 OB attachment on porous scaffolds is plotted as a function of time for 0.5, 1, 2 and 4 hours (Figure 3). Based on hemacytometer analysis, OB attachment on the micro HA scaffolds appears greater than on the nano HA scaffolds and differences were statistically significant (with $p < 0.05$).

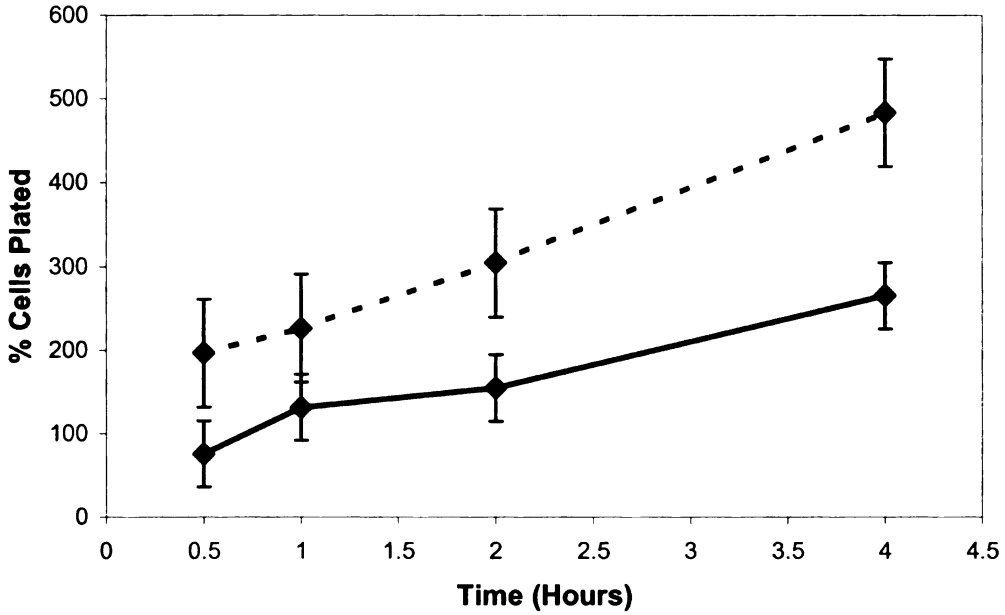

Figure 3: MC3T3-E1 OB attachment on micro HA (dashed line) and nano HA (solid line) scaffolds as a function of time, at intervals of 0.5, 1, 2 and 4 hours. Values are mean ± SE, $p < 0.05$ at all time intervals for comparison of nano HA to micro HA.

When OB cell number is examined, the mean values for OB proliferation on nano HA scaffolds are higher when compared to the mean values on micro HA scaffolds (Figure 4) at 1, 3 and 5 days culture time. Differences in proliferation between micro HA and nano HA scaffolds at 1 and 3 days were not found to be statistically significant, with $p > 0.05$ in both cases ($p = 0.64$ and $p = 0.12$, respectively). However, at 5 days, differences in osteoblast number were found to be significant ($p < 0.05$).

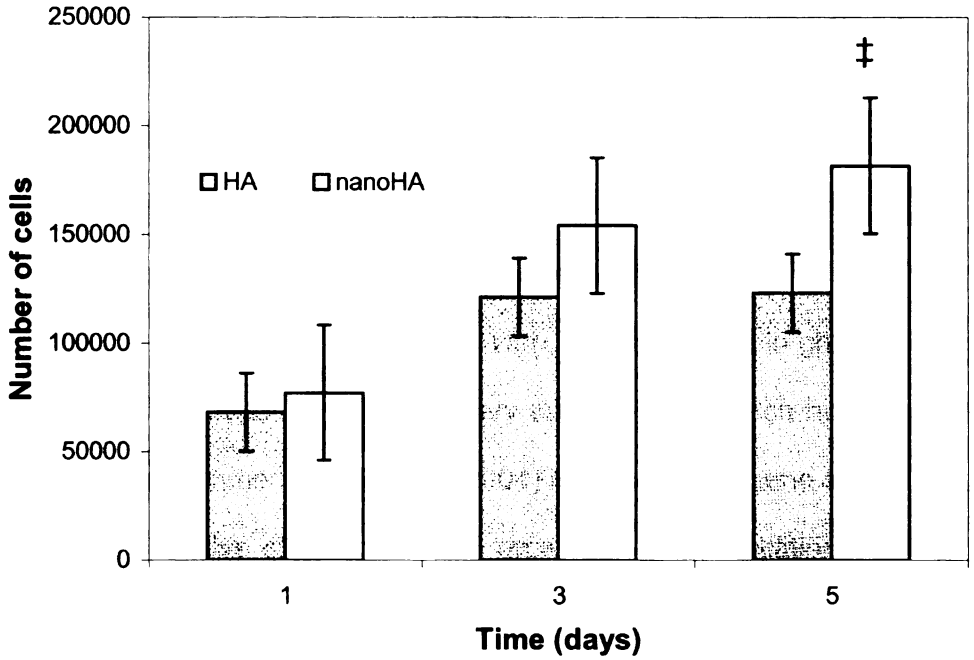

Figure 4: MC3T3-E1 Osteoblast proliferation on micro HA and nano HA, after periods of 1, 3 and 5 days. Values are mean ± SE. $p > 0.05$ for comparison of nano HA to micro HA porous scaffold for 1 and 3 days. $p < 0.05$ for 5 days (‡).

DISCUSSION

Porous bioceramic scaffolds offer advantages over dense substrates for bone tissue engineering applications, because they present a more complex interface for bone ingrowth that more closely mimics natural bone. Hench, 1998; Hulbert et al, 1972; Hulbert et al, 1970) Additionally, porous CaP ceramics are capable of promoting osteoprogenitor attachment and new bone formation. (Ohgushi et al, 1990) Osteoprogenitor cells cultured on porous HA have been shown to produce extracellular matrix *in vivo*, a precursor to bone formation. (Ohgushi et al, 1990) Therefore, it is important to observe the effect of HA grain

size reduction on OB behavior and to examine these differences for porous scaffolds which are more suited for bone tissue engineering applications.

Foaming and sintering nano HA with a particle size of 20 nm yielded porous scaffolds of submicron grain size (588 ± 55 nm). While this grain size is not truly nanoscale (< 100 nm), it is small enough to assess the effect of grain size reduction (15X) on OB behavior *in vitro*. This reduction in grain size means that there is an increased grain boundary surface area, which has been tied to increased OB attachment (Perla et al, 2004) and enhanced gene expression (Xie et al, 2004) indicative of increased cell growth and differentiation. Reduction in grain size has also been linked to increased surface roughness, which in turn has been shown to increase OB adhesion, proliferation, AP activity and calcium production. (Webster 2001) In future studies, atomic force microscopy (AFM) will be used to measure the surface roughness of these scaffolds, to determine whether these results are repeatable for porous HA.

Webster et al have repeatedly shown that a large decrease in HA grain size produces changes in osteoblast activity, including improvements in attachment and proliferation. (Webster et al, 1999a; Webster et al, 2000a; Webster et al, 2000b; Webster et al, 2001) Results of this study both contradict (OB attachment) and reinforce (OB proliferation) these findings. Our study shows that OB attachment did not improve on scaffolds fabricated from nano HA powder as compared to those produced from micro HA powder. However, each of Webster's studies used dense HA having a sintered grain size of 67 nm (Webster et al, 2000a; Webster et al, 2000b), which is ~11% of our sintered grain

size and only 1/3 larger than their unsintered particle size. In contrast, our scaffolds have grains, which are 30 times larger than our unsintered particles. This difference in grain growth in our scaffolds, from 20 nm to 588 ± 55 nm, is likely an artifact of the highly porous nature of our scaffolds in which the predominant sintering mechanism is coarsening. (Barsoum, 1997) Future studies will investigate the sintering behavior of these foamed nano HA scaffolds with the goal of reducing grain growth to yield true high volume porosity nanograined HA scaffolds.

At each time period, 0.5, 1, 2 and 4 hours, hemacytometer analyses suggest an increase in cell number (attachment) on micro HA scaffolds compared to nano HA scaffolds. This suggests that increased grain is not positively related to OB attachment behavior in highly porous scaffolds. However, the cell attachment values for both scaffolds are much larger in this study than expected. This suggests that HA particles themselves may have been included in the cell counting analyses. Additional approaches are currently being used to address this issue.

While OB attachment did not increase with decreased grain size, the mean OB proliferation, measured at 1, 3 and 5 days, on nano HA scaffolds was higher than the mean values for the micro HA scaffolds. This indicates that proliferation may be driven by increased grain boundary area resulting from the smaller grain size, in addition to the optimum morphology in terms of pore size and pore interconnectivity (eg macro and microporosity) presented by our highly porous scaffolds. The basis for OB/HA adhesion and the effect of grain boundary

volume on OB behavior are not completely understood, but may be linked in part to protein interactions at the surface. (Webster et al, 2000b) Webster et al found that a decrease in grain size promoted an increase in vitronectin and collagen concentration and a decrease in albumin, laminin and fibronectin concentration. (Webster et al, 2000b) They also linked the protein stereochemical structure to grain size and surface topography of bioceramic substrates. (Webster et al, 2000b) Based on these findings, FBS proteins may adsorb more readily to nano HA scaffolds compared to micro HA scaffolds in this study, but this was not verified. The effect of FBS protein adsorption *in vitro*, contrasted with protein adsorption in an *in vivo* environment should be investigated.

Other approaches to increasing OB attachment and proliferation on HA surfaces include peptide coating. For example, EEEEEEEPRGDT coating increased attachment at 30 minutes, as compared to an HA control. (Itoh et al, 2002) GRGDSPC and cyclo-DfKRG increase osteoprogenitor cell attachment at 3 and 24 hours, as compared to non-treated hydroxyapatite. (Durrieu et al, 2004) While these coatings increased OB attachment and proliferation, the smaller grain size found in our HA scaffolds is an intrinsic property, reducing the need for post-fabrication scaffold treatments such at the peptide coatings of Itoh et al. and Durrieu et al.

Although the use of nano HA in porous bone scaffolds does not initially improve OB attachment by 4 hours culture time, the apparent increase in proliferation of OBs at day 5 shows the potential for more rapid osteoblast growth, and presumably more rapid calcification and bone formation *in vitro*.

While further studies must be conducted to measure OB differentiation and calcium production over time *in vitro*, nano HA porous bone scaffolds, because of their increased grain boundary area and optimum pore size and interconnectivity, show promise as an effective bone scaffold for use in bone tissue engineering applications.

ACKNOWLEDGEMENTS

The authors acknowledge the use of the SEM facilities at the Advanced Microscopy Center, Michigan State University along with the assistance of Mr J Quast with the SEM imaging.

REFERENCES

Areva, S, Paldan, H, Peltola, T, et al. 2004. Use of sol-gel-derived titania coating for direct soft tissue attachment. *J Biomed Mater Res.* 70A:169-78.

ASTM. 2004. E112-96 Standard Test Methods for Determining Average Grain Size. *ASTM International.*

Barsoum, M. 1997. Fundamentals of ceramics. McGraw-Hill, New York.

Cerroni, L, Filocamo, R, Fabbri, M, et al. 2002. Growth of osteoblast-like cells on porous hydroxyapatite ceramics: an in vitro study. *Biomol Eng.* 19:119-24.

Chen, QZ, Lu, WW, Wong, CT, et al. 2004. Role of collagen fibres in bone-bonding of crystalline hydroxyapatite implant. *7th World Biomaterials Congress,* Sydney, Australia. 1439.

Cui, FZ, Zhang, W and Liao, SS. 2004. Hierarchical self-assembling of nano-fabril of mineralized collagen for bone graft. *7th World Biomaterials Congress,* Sydney, Australia. 1004.

deGroot, K. 1988. Effect of porosity and physicochemical properties on the stability, resorption, and strength of calcium phosphate ceramics. *Ann N Y Acad Sci.* 523:227-33.

Du, C, Cui, FZ, Feng, QL, et al. 1998. Tissue response to nano-hydroxyapatite/collagen composite implants in marrow cavity. *J Biomed Mater Res.* 42:540-8.

Du, C, Cui, FZ, Zhu, XD, et al. 1999. Three-dimensional nano-HAp/collagen matrix loading with osteogenic cells in organ culture. *J Biomed Mater Res.* 44:407-15.

Durrieu, MC, Pallu, S, Guillemot, F, et al. 2004. Grafting RGD containing peptides onto hydroxyapatite to promote osteoblastic cells adhesion. *J Mat Sci: Mat Med.* 15:779-86.

Fratzl, P, Gupta, HS, Paschalis, EP, et al. 2004. Structure and mechanical quality of the collage-mineral nano-composite in bone. *J Mater Chem.* 14:2115-23.

Griffin, MA, Smith, IO and Baumann, MJ. 2005. Comparison between primary and clonal osteoblast cells for in vitro attachment studies to hydroxyapatite.

Hassenkam, T, Fantner, GE, Cutroni, JA, et al. 2004. High-resolution AFM imaging of intact and fractured trabecular bone. *Bone.* 35:4-10.

Hench, LL. 1998. Bioceramics. *J Am Ceram Soc.* 81:1705-28.

Huang, J, Best, SM, Bonfield, W, et al. 2004. *In vitro* assessment of the biological response to nano-sized hydroxyapatite. *J Mater Sci: Mater M.* 15:441-5.

Hulbert, SF, Morrison, SJ and Klawitter, JJ. 1972. Tissue response to three ceramics of porous and non-porous structures. *J Biomed Mater Res.* 6:347-74.

Hulbert, SF, Young, FA, Mathews, RS, et al. 1970. Potential of ceramic materials as permanently implantable skeletal protheses. *J Biomed Mater Res.* 4:433-56.

Itoh, D, Yoneda, S, Kuroda, S, et al. 2002. Enhancement of osteogenesis on hydroxyapatite surface coated with synthetic peptide (EEEEEEEPRGDT) *in vitro*. *J Biomed Mater Res.* 62:292-8.

Iyer, VV, Kadakia, TB, McCabe, LR, et al. 2004. CCAAT/enhancer-binding protein-beta has a role in osteoblast proliferation and differentiation. *Exp Cell Res.* 295:128-37.

Jarcho, M. 1981. Calcium phosphate ceramics as hard tissue prosthetics. *Clin Orthop Relat R.* 157:259-78.

Li, Z, Yubao, L, Wang, X, et al. 2004. Comparison of compositions and structural characterizations of synthetic nano-hydroxyapatite and mineral phase from porcine femoral bone. *High technology Letters.* 10:48-51.

Liao, SS, Cui, FZ, Zhang, W, et al. 2004. Hierarchically biomimetic bone scaffold materials: Nano-HA/collagen/PLA composite. *J Biomed Mater Res.* 69B:158-65.

Longsworth, J and Eppell, SJ. 2002. Design and assembly of a sterile nanoscale orthopedic biomaterial. *Biomaterials, proceedings of the northeast conference,* 173-4.

McMullen, R. 2004. In *Chemical Engineering and Materials Science*. Vol. Michigan State University, East Lansing, MI.

Ohgushi, H, Okumura, M, Tamai, S, et al. 1990. Marrow cell induced osteogenesis in porous hydroxyapatite and tricalcium phosphate: a comparative histomorphometric study of ectopic bone foremation. *J Biomed Mater Res.* 24:1563-70.

Perla, V, Ejiofor, JU and Webster, TJ. 2004. Directed osteoblast adhesion at particle boundaries: Promises for nanophase metals. *Mat Res Soc Symp,* 823:207-12.

Sakane, M, Mutsuzaki, H, Miyanaga, Y, et al. 2004. Nano-composites of calcium phosphate-collagen promote osteoclast growth at the interface between tendons and bone tunnels in knee ligament reconstruction. *7th World Biomaterials Congress,* Sydney, Australia. 385.

Shu, R, McMullen, R, Baumann, MJ, et al. 2003. Hydroxyapatite accelerates differentiation and suppresses growth of MC3T3-E1 osteoblasts. *J Biomed Mater Res.* 67A:1196-204.

Silva, CC, Pinheiro, AG, de Oliveira, RS, et al. 2004. Properties and *in vivo* investigation of nanocrystalline hydroxyapatite obtained by mechanical alloying. *Mat Sci and Eng C.* 24:549-54.

Webster, TJ, Ergun, C, Doremus, RH, et al. 1999a. Nanocrystalline hydroxyapatite enhances osteoblast function. *First Joint BMES/EMBS Conference,* Atlanta, GA. 744.

Webster, TJ, Ergun, C, Doremus, RH, et al. 2000a. Enhanced functions of osteoblasts on nanophase ceramics. *Biomaterials.* 21:1803-10.

Webster, TJ, Ergun, C, Doremus, RH, et al. 2000b. Specific proteins mediate enhanced osteoblast adhesion on nanophase ceramics. *J Biomed Mater Res.* 51:475-83.

Webster, TJ, Siegel, RW and Bizios, R. 1999b. Design and evaluation of nanophase alumina for orthopaedic/dental applications. *Nanostruct Mater.* 12:983-6.

Webster, TJ, Siegel, RW and Bizios, R. 1999c. Osteoblast adhesion on nanophase ceramics. *Biomaterials.* 20:1221-7.

Webster, TJ, Siegel, RW and Bizios, R. 2001. Nanoceramic surface roughness enhances osteoblast and osteoclast functions for improved orthopaedic/dental implant efficiency. *Scripta Mater.* 44:1639-42.

Wei, J, Li, Y, Chen, W, et al. 2003. A study on nano-composite of hydroxyapatite and polyamide. *J Mater Sci.* 38:3303-6.

Wei, J, Yubao, L, Xuelig, P, et al. 2004a. Injectable apatite and ploymer biomimetic nano-composite cement for bone tissue engineering. *7th World Biomaterials Congress,* Sydney, Australia. 1359.

Wei, J, Yubao, L, Xuelig, P, et al. 2004b. A study on tissue engineering scaffold material of nano-apatite and polyamide composite. *7th World Biomaterials Congress,* Sydney, Australia. 827.

Werner, J, Linner-Krcmar, B, Friess, W, et al. 2002. Mechanical properties and in vitro cell compatibility of hydroxyapatite ceramics with graded pore structure. *Biomaterials.* 23:4285-1494.

Xie, J, Baumann, MJ and McCabe, LR. 2004. Osteoblasts respond to hydroxyapatite surfaces with immediate changes in gene expression. *J Biomed Mater Res.* 71A:108-17.

Yoneda, S, Guthrie, WF, Bright, DS, et al. 2004. In vitro biocompatibility of hydrolytically degraded poly(d,l-lactic acid). *7th World Biomaterials Congress,* Sydney, Australia. 1324.

Young, B and Heath, JW. 2000. Wheater's Functional Histology. Churchill Livingstone, Edinburgh.

CHAPTER 4

A BRIEF COMMUNICATION REGARDING THE INACCURACIES OF HEMACYTOMETER MEASUREMENTS WHEN ASSESSING OSTEOBLAST ATTACHMENT ON POROUS NANO- AND MICRON-SCALE HYDROXYAPATITE SCAFFOLDS

IAN O. SMITH[1], LAURA R. MCCABE[2] AND MELISSA J. BAUMANN[1]
[1]Dept Chemical Engineering and Materials Science, Michigan State University, East Lansing, MI, USA
[2]Dept Physiology, Michigan State University, East Lansing, MI, USA

INTRODUCTION

In our paper entitled "MC3T3-E1 osteoblast attachment and proliferation on porous hydroxyapatite scaffolds fabricated with nanophase powder", published in the International Journal of Nanomedicine[1], we found that porous scaffolds fabricated using nano-scale hydroxyapatite (HA) powder significantly improved osteoblast (OB) proliferation when compared to HA scaffolds fabricated with micron-scale powder after 5 days *in vitro*. However, we also showed that OB attachment on nano-HA porous scaffolds was significantly lower on the nano-HA powder scaffolds in comparison to the micron-HA porous scaffolds. This finding is contrary to those shown in multiple studies by Webster et al., who found that a large decrease in grain size led to increased OB attachment and proliferation[2-5]. This apparent discrepancy led us to examine the accuracy of the techniques used in our previous study, namely OB counts using a hemacytometer.

In this letter, we address the accuracy of hemacytometer counts for porous HA scaffolds and use a simple method to reduce the error. The hemacytometer relies on transmitted light to identify cells. In order to trypsinize

and count the cells, we had to morselize the porous scaffolds. Therefore, despite our best efforts to eliminate extraneous morselized scaffold particles, the HA scaffold particles were commingled with the OBs and, because these particles reflected light in a similar manner and were of approximately the same size, it was difficult to discern between an OB and an HA morsel. By employing a background count to quantify the number of HA particles which could be statistically generated during the sample processing procedure, we can subtract these values from the raw counts leaving us with a normalized and corrected OB cell count.

MATERIALS AND METHODS

Cylindrical porous HA scaffolds were fabricated using the foaming technique described in earlier studies.[1,6] Sintered HA specimens were approximately 2 cm in length and 1.25 cm in diameter with an average porosity of 59 ± 2.2% (micron-HA) or 72 ± 8.3% (nano-HA), determined by Archimedes method. These HA scaffolds had an average grain diameter of 8.6 ± 1.9 μm for micron-HA and 588 ± 55 nm for nano-HA, with a bimodal pore distribution (macro/micropore diameter of 390 ± 210 μm/38 ± 33 μm for micron-HA and 480 ± 275 μm/30 + 21 μm for nano-HA) determined by scanning electron microscopy.[1] These cylindrical specimens were sectioned into 2 mm-thick discs using a Buehler Isomet 1000 diamond abrasive wafering saw. Three micron-HA discs and three nano-HA discs were used at each time point and the entire study was run in triplicate, requiring a total of 63 micron-HA discs and 63 nano-HA discs.

Prior to OB seeding, scaffolds were autoclave sterilized and placed into commercially pure Al collars.

MC3T3-E1 subclone 7 murine osteoblasts (OBs) of passage 26-28 were used for this study. OBs were cultured on polystyrene (PS) tissue culture plates, with complete media (α minimum essential media [α-MEM] supplemented with 10% fetal bovine serum [FBS]) until a suitable population size was reached. Prior to seeding onto the porous HA scaffolds, the OBs were removed from the PS using trypsin-EDTA and counted with a hemacytometer. The OBs were then placed into 24-well plates, one per well and the OBs seeded onto the scaffolds at 11,320 cells/cm^2 to ensure confluency[7] with 2 ml of complete media added to each well. These specimens were then incubated at 37°C, 5% CO_2 and high humidity.

OB attachment was assessed at 0.5, 1, 2 and 4 hours and OB proliferation measured at 1, 3 and 5 days. At each time interval, the scaffolds were removed, rinsed with 1X phosphate-buffered saline (PBS), to remove any non-adherent OBs, and placed onto fresh 24-well tissue culture plates, one per well. One ml each of trypsin-EDTA and complete media were then added to each well. Scaffold homogenization was used to assist in the release of OBs from surface during trypsinization.[8] Each scaffold was morselized using the handle-end of a cell scraper (Benton Dickenson) to encourage OB detachment. Samples of suspended OBs were then drawn from each well and the cells counted using a hemacytometer. The student's t-test was used to determine statistical difference at each time point, with $p < 0.05$ taken to indicate a significant difference.

Because the remnants of the morselized scaffold can be of a similar size and shape as the OBs when viewed under the hemacytometer (Figure 1), background counts on morselized HA scaffolds which were not seeded with OBs were also conducted. Three micro-HA specimens and three nano-HA specimens (run in triplicate for a total of 9 each) were submerged in complete media, removed, rinsed with 1X PBS, trypsin was added and the scaffolds morselized. Media was drawn from each well and any cell-like particles were counted using a hemacytometer. These background counts were then subtracted from the raw hemacytometer counts at each time interval.

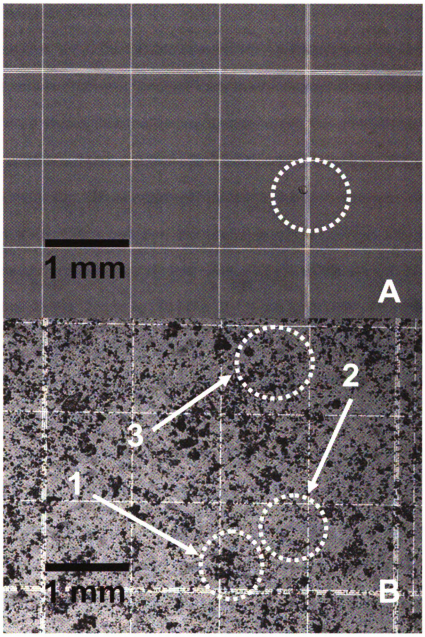

Figure 1: Figure 1A is an optical micrograph of a hemacytometer with a single OB (indicated by circle) taken during a cell count where there were no ground HA particles. Figure 1B is an optical micrograph of a hemacytometer with a morselized OB-seeded micron-HA scaffold. Arrow 1 indicates an HA particle, arrow 2 indicates an OB and arrow 3 indicates an object that is not definitively one or the other. The general haze resulting from the ground particles, as well as the presence of larger OB-sized particles make it difficult to identify OBs.

RESULTS AND DISCUSSION

Figure 2 is a plot of OB attachment (0 – 4 hours) and proliferation (24 - 120 hours) versus time with, and without, the background HA count subtracted away. The data shows that the background-adjusted OB attachment on micron-HA porous scaffolds increases from 66 ± 259% at 0.5 hours to 193 ± 327% at 4 hours. In comparison, OB attachment increases to a lesser degree on nano-HA, from 0% to 28 ± 155% between 0.5 and 4 hours. However, OB proliferation increases much more noticeably, from 239 ± 261% to 1004 ± 697% on micron-HA and from 239 ± 261% to 1044 ± 301% on nano-HA. These results are different than those reported in our earlier work, in that there is no significant difference in OB attachment or proliferation on nano-HA porous scaffolds compared to micron-HA porous scaffolds.[1]

The non-adjusted data is consistent with our earlier findings showing OB attachment to be significantly higher ($p < 0.05$) for micron-HA porous scaffolds with no significant difference ($p > 0.05$) in OB proliferation between 1 and 3 days for nano-HA relative to micron-HA porous scaffolds. The non-adjusted data does differ from the earlier data in that at 5 days OB proliferation is not significantly higher on nano-HA scaffolds compared to micron-HA scaffolds.

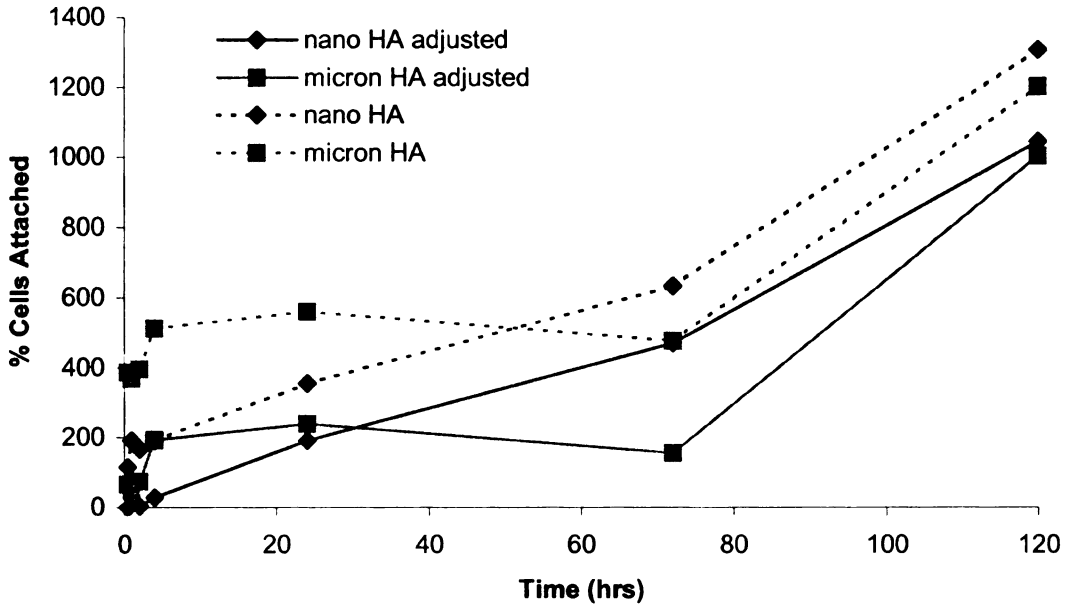

Figure 2: MC3T3-E1 OB attachment (0.5, 1, 2 and 4 hrs) and proliferation (24, 72 and 120 hrs) on porous nano-HA and micron-HA scaffolds.

Both the nano-HA and micron-HA scaffolds promote OB proliferation at times approaching five days. This indicates that the controlling factor in whether a porous scaffold potentially promotes bone growth may be porosity, rather than grain size. This finding is contrary to those shown at length by Webster et al. and to a lesser extent by Xie et al. in studies of OB behavior on dense ceramic scaffolds, including HA, which showed that decreased grain size improved OB attachment, proliferation, differentiation, AP activity and calcium production[2-5] as well as enhanced gene expression[9]. However, in each of these cases the scaffolds studied were highly dense, meaning that grains and surface roughness were the only topographical features present. In comparison, a bimodally porous scaffold, such as those used in the current study, more closely mimics the

structure of natural bone[10-12] and presents a more biomimetic interface for OB interactions. These findings further strengthen the argument that bimodal porosity, similar to that found in natural bone, is a primary factor in promoting bone ingrowth. Bone tissue engineering scaffold materials, including HA, must include both large and small pores, which allow ingrowth and nutrient flow.

CONCLUSIONS

The purpose of examining hemacytometer counting techniques for assessing OB attachment and proliferation on porous HA scaffolds was to determine whether inherent problems with this technique could be corrected by utilizing background counts. By using a simple background count, where scaffolds were ground and OB-like objects were counted, we attempted to correct for any inaccuracy in hemacytometer values. While this method reduced interference in hemacytometer counts due to the inclusion of HA particles, the results indicate further inaccuracies. Results show roughly a doubling of the OB population by 10 hours, which is not typical on HA.[7] This high number of OBs is likely due to counting non-adherent cells, which were trapped in the porous matrix and not effectively rinsed away. To avoid these problems, a quantifiable stain could be used in lieu of hemacytometer counts, and a more thorough rinsing regimen used.

Inaccurate OB counts from hemacytometer data for porous scaffolds is currently unavoidable. The scaffolds used here are porous in nature as opposed to the dense scaffolds used in past studies[2-5, 9], which have looked solely at the

effect of grain size and not the role of porosity in OB attachment. Hence, these measurements have been made on dense samples that have not needed to be morselized. It is not surprising then that our results from porous scaffolds are different when compared to the dense scaffolds used in these earlier studies. While using dense samples makes cell attachment measurements more straightforward, the dense surface of these samples is less biomimetic and not applicable in many *in vivo* applications.

REFERENCES

1. Smith IO, McCabe LR, Baumann MJ. MC3T3-E1 Osteoblast attachment and proliferation on porous hydroxyapatite scaffolds with nanophase powder. Int J Nanomed 2006;1:189-194.

2. Webster TJ, Ergun C, Doremus RH, Siegel RW, Bizios R. Nanocrystalline hydroxyapatite enhances osteoblast function. In: Proceedings of the First Joint BMES/EMBS Conference, Atlanta, GA; 1999. p744.

3. Webster TJ, Siegel RW Bizios R. Design and evaluation of nanophase alumina for orthopaedic/dental applications. Nanostruct Mater 1999;12:983-986.

4. Webster TJ, Siegel RW Bizios R. Osteoblast adhesion on nanophase ceramics. Biomaterials 1999;20:1221-1227.

5. Webster TJ, Ergun C, Doremus RH, Siegel SW, Bizios R. Enhanced functions of osteoblasts on nanophase ceramics. Biomaterials 2000;21:1803-1810.

6. McMullen, R. An in vitro investigation of MC3T3-E1 osteoblast proliferation and differentiation on hydroxyapatite based tissue-engineered scaffolds. Masters Degree Thesis. Department of Chemical Engineering and Materials Science. Michigan State University, East Lansing, MI; 2004. 181p.

7. Shu R, McMullen R, Baumann MJ, McCabe LR. Hydroxyapatite accelerates differentiation and suppresses growth of MC3T3-E1 osteoblasts. J Biomed Mater Res. 2003;67A:1196-1204.

8. Lu HH, Tang A, Oh SC, Spalazzi JP, Dionisio K. Compositional effects on the formation of a calcium phosphate layer and the response of osteoblast-like cells on polymer-bioactive glass composites. Biomaterials 2005;26:6323-6334.

9. Xie J, Baumann MJ McCabe LR. Osteoblasts respond to hydroxyapatite surfaces with immediate changes in gene expression. J Biomed Mater Res. 2004;71A:108-117.

10. Hench LL.. Bioceramics. J Am Ceram Soc 1998;81:1705-1728.

11. Hulbert SF, Morrison SJ, Klawitter JJ. Tissue response to three ceramics of porous and non-porous structures. J Biomed Mater Res 1972;6:347-374.

12. Hulbert SF, Young FA, Mathews RS, Klawitter JJ, Talbert CD, Stelling FH. Potential of ceramic materials as permanently implantable skeletal protheses. J Biomed Mater Res. 1970;4:433-456.

CHAPTER 5

MICROCRACKING AND POROSITY IN CALCIUM PHOSPHATES AND THE IMPLICATIONS FOR BONE TISSUE ENGINEERING

E.D. CASE, I.O. SMITH AND M.J. BAUMANN
Department of Chemical Engineering and Materials Science,
Michigan State University, East Lansing, MI 48824-1226 USA

PUBLISHED IN: Mater Sci Engin A 2005 390:246-254.

ABSTRACT

Calcium phosphates including hydroxyapatite (HA) have been widely studied as bone scaffold materials. However their mechanical properties are highly variable and may be a function of thermal expansion anisotropy (TEA) induced stresses and microcracking. There is confusion concerning the mechanisms and microscopic identification of microcracks in HA. This study presents clear evidence of microcracking from micrographs of as-sintered HA surfaces which avoids the complications of identifying TEA-induced microcracks on fracture surfaces. Additionally, the existing literature of TEA-induced microcracking is briefly reviewed and pertinent papers involving likely microcracking in HA are analyzed. The recent realization in the biomedical literature notes that microcracks are of critical importance in remodeling and repair of damaged bone tissue. Hence, the similarities between microcracking in HA used for scaffolds in bone tissue engineering and that in the normal bone repair process is of importance in designing HA scaffolds with improved mechanical properties and biocompatibility.

INTRODUCTION

When a material exhibits thermal expansion anisotropy (TEA), the coefficient of thermal expansion is a function of crystallographic direction. TEA occurs in all crystalline systems of lower symmetry than cubic [1]. In general, any material property described by a second rank tensor (such as the thermal expansion coefficient, α_{ij}) is isotropic in an amorphous material and in a cubic atomic lattice, but for tetragonal, hexagonal, orthorhombic, monoclinic and triclinic systems, α_{ij} is no longer isotropic.

Hydroxyapatite (HA) often crystallizes in a hexagonal lattice with space group P63/m [2, 3], although HA also may crystallize in a monoclinic lattice with space group $P2_1/b$ [4]. Thus, in either the hexagonal or monoclinic form, HA exhibits thermal expansion anisotropy. However, the important practical effects of TEA arise in polycrystalline bodies, since as polycrystalline materials cool from elevated temperatures, thermal expansion anisotropy results in contraction of individual grains from neighboring grains at differing rates, depending upon crystallographic direction. These differences in thermal contraction rates give rise to mechanical stresses.

The physical consequences of the thermal expansion anisotropy are mainly determined by the magnitude of the thermal expansion differences along the crystallographic axes, say α_1, α_2 and α_3. If the differences among the α_1, α_2 and α_3 values are sufficiently large, the TEA driven stresses can generate microcracks.

In this study, we briefly review the concept of TEA-induced microcracking and the critical grain size for microcracking. We also discuss the biomedical implications of microcracking in bone and HA and the concomitant implications for bone tissue engineering. Finally, we present a series of micrographs of dense HA specimens and carefully consider studies in the literature that deal with microcracking in HA.

BACKGROUND

Microcracking and critical grain size

An energy balance between a volumetric energy term (the stored elastic strain energy) and an area energy term (the surface energy corresponding to the newly created crack surface area) gives rise to a critical grain size for TEA-induced microcracking in brittle polycrystalline materials. If the specimen grain size is G, then the condition that $G > G_{CR}$ leads to microcracking in the specimen while if $G < G_{CR}$, then the specimen does not microcrack. The critical grain size, G_{CR}, can be estimated by [5, 6]

$$G_{CR} = \frac{14.4\gamma_f}{E(\Delta T)^2(\Delta\alpha_{max}{}^2)} \qquad (1)$$

where γ_f is the fracture surface energy, E is the Young's modulus of the material, and $\Delta\alpha_{max}$ is the maximum difference in the values of the thermal expansion coefficients along the crystallographic axes. The effective temperature interval over which TEA stresses accumulate in the specimen is given by ΔT. At

elevated temperatures, stresses can relax in the specimen, but during cooling the specimen will reach a temperature, T_U, at which the intergranular stresses no longer relax. ΔT is thus given by $(T_U - T_L)$, where T_L is the low temperature limit of the heating cycle (typically T_L is room temperature).

The value of the critical grain size for thermal expansion microcracking varies from ceramic to ceramic. For example, literature values of G_{CR} for ceramic oxides span nearly two orders of magnitude with a G_{CR} of approximately 100 μm for alumina [7], about 15 μm for gadolinum oxide [8], and roughly 3 μm for $FeTi_2O_5$ [6]. As is predicted by equation 1, the trend in G_{CR} tends to be dominated by $\Delta\alpha_{max}$, with G_{CR} decreasing rapidly as the degree of thermal expansion anisotropy (measured by $\Delta\alpha_{max}$) increases.

In addition to the existence of a critical grain size, a crucial aspect of TEA-induced stress and microcracking is related to the mechanical behavior based on whether G is smaller or larger than G_{CR}. As an example, consider grain size G_{S1}, where $G_{S1} << G_{CR}$. The residual stresses due to TEA would be relatively minimal in this case.

However, as the grain size increases toward G_{CR}, the local stresses can significantly alter the strength and fracture toughness of the material [9, 10]. If the grain size increases to G_{S2} where G_{S2} is slightly smaller than G_{CR}, then ideally the specimen would not microcrack but the residual stresses induced by TEA could be quite large and would in fact become sufficient to generate microcracks if the grain size is increased slightly, such that G_{S2} becomes equal to G_{CR} [10, 11].

For a grain size G_{L1} slightly larger than the critical grain size, microcrack damage begins to accumulate in the specimen [11, 12]. If the grain size is further increased such that $G_{L2} > G_{CR}$, then the observed magnitude of TEA-induced microcrack damage increases as the grain size increases [7, 8, 13, 14]. For $G > G_{CR}$, the resulting microcracking in polycrystalline specimens impacts the fracture behavior of the specimen, causing either a net increase or decrease in fracture toughness [15, 16].

In addition to changes in strength and fracture toughness when $G > G_{CR}$, volumetrically distributed microcrack damage within the specimen leads to changes in a wide variety of material parameters, including the elastic modulus [6-8, 10, 17] and thermal conductivity [18, 19].

Microcracking in Bone

It is well accepted that fatigue injuries such as stress fractures result in microcracking in the bone. There is in turn ample evidence linking these microcracks to bone healing and remodeling in both the human and veterinary literature [20, 21]. The ability of bone to microcrack improves its toughness by absorbing energy, thereby preventing or slowing down the propagation of a failure-inducing macrocrack [22, 23].

Examining the distal ends (the end furthest from the body) of the third metacarpal and metatarsal bones of Thoroughbred racehorses with condylar fractures, Radtke found that macrofracture and failure of the bone was correlated to the presence of microcracks [24]. In a separate study investigating the fatigue

damage in the greyhound central tarsal bone, Muir notes the presence of both linear microcracks (~30-110 μm in length) and clusters of ultra-microcracking (<10 μm in length) [21]. Linear microcracking was found to exist around areas of remodeled cortical and trabecular bone adjacent to a vascular supply, while ultra-microcracking under tensile loading was found at the attachment site of the plantar ligament.

While the exact functional relationships are not known between fatigue and stress fractures, bone remodeling and repair have been associated with the initiation of microcracks arising from fatigue damage and altered osteocytes activity in a study by Bentolila in adult rat long bones [25]. In humans, Burr et al. find that microcrack density increases with age, where the microcrack damage is initiated at the collagen fiber to bone matrix attachment sites and rapidly accelerates after 40 years of age [26].

There is a proven significant increase in remodeling sites that develop after the initiation of microcracking. However, if fatigue damage continues concomitant with bone remodeling (which involves an increase in the local bone porosity), the resulting loss of mechanical properties, such as strength and stiffness, likely is a cause of further microcracking. This would in turn, stimulate further remodeling and a loss of mechanical integrity until fracture finally occurs. Such a site specific response to fatigue damage is only just gaining acceptance in the biological community and has implications for understanding fracture and healing in the osteoporotic elderly and in human and animal athletes [27, 28].

HA in Bone Tissue Engineering

Each year ~300,000 bone grafts are performed in the U.S. [29]. Applications include bone loss from neoplasia, fracture repair, spinal surgery, and fracture treatment in the elderly. The model bone substitute is 1) osteogenic (direct bone formation via transplanted bone cells called osteoblasts, 2) osteoinductive (the ability to recruit bone forming cells), 3) osteoconductive (the scaffold supports bone in-growth), 4) mechanically stable and 5) readily available. Although autografts (bone transplants from the patients own bone supply) and allografts (same species transplants from a banked supply of bone) seem ideal to repair bone defects, they are limited in supply, carry additional surgical/patient risks and possess diminished properties [30, 31].

Because the mineral content of bone has a composition and crystal structure closely matching HA, porous calcium phosphates like HA (non-resorbable in vivo [32]), β-TCP (resorbable in vivo [32]) and BCP (a mixture of HA and β-TCP) are being investigated for use in bone tissue engineering applications. Dense calcium phosphates cannot support osteoblast in-growth or bone formation while porous calcium phosphates are osteoconductive, but lack the strength of dense HA.

EXPERIMENTAL PROCEDURE

Commercial HA and β-TCP powders[1], of vendor-specified medical grade purity, were obtained and used as manufactured. BCP powder was obtained by

[1] Berkeley Advanced Biomaterials Inc., San Leandro, Ca., USA

mixing 60% HA (particle diameter of 0.85 μm) with 40% β-TCP (particle diameter of 1.15 μm) powders by volume. This mixture was then shaken for one minute and thoroughly mixed by placing the container in an ultrasonic bath for 30 minutes. Green disc specimens were fabricated by uniaxially pressing 1.5 ± 0.002 g of dry powder in a 32 mm diameter pellet die at 6.9 MPa for one minute using a standard laboratory press. Discs were sintered in air for four hours at either 1360°C (for HA) or 1200°C (for β-TCP and BCP) in a high temperature sintering furnace (CM Rapid Temp Furnace) by heating from room temperature to the sintering temperature at a rate of ~10°C/min. Following sintering, samples were cooled to room temperature by a controlled furnace cool at a rate of ~10°C/min. The pore volume was determined using Archimedes method and the pore and grain size determined using the line-intercept method.

To determine phase composition and purity, X-ray diffraction (XRD) was performed on (1) unsintered powder specimens from each of the three starting powders (HA, β-TCP and BCP) as well as (2) powder specimens obtained by grinding the sintered disc specimens. All powders were mounted on a borosilicate glass slide and scanned in a powder diffractometer over the 2θ range from 20° to 50° using filtered Cu-Kα radiation. Sintered discs were ground with an agate mortar and pestle and the resulting powder was sieved to remove large particles.

Sintered specimens used for grain size analysis were polished to 1 μm with diamond paste followed by ultrasonic cleaning and thermal etching at

1200°C for four hours. Additional sintered discs were prepared for examination in the scanning electron microscope (SEM) by slicing each disc perpendicular to the circular face using a low speed diamond wafering saw or by fracturing the discs by the impact of a steel wedge on the specimen surface. The specimens were sectioned in order to produce samples small enough to fit into the SEM chamber. Specimens were cut using a Beuhler Isomet 1000 low speed saw with a diamond wafering blade at 200 rpm. This dry procedure was used to suppress possible microcracking or microcrack extension induced by liquid immersion. The surfaces were then prepared for examination in the SEM by mounting sections of each material on an Al stub with C adhesive tape and gold coating using an EMSCOPE SC500 Sputter Coater operated at 20 mA for 3 minutes resulting in a gold coating of 21 nm. SEM micrographs were taken at an accelerating potential of 15 KeV and a working distance of 15 mm on a JEOL JSM6400 SEM equipped with a LaB_6 emitter. During imaging, care was taken to ensure that micrographs were imaged of representative areas, at least 2 mm away from the cut or fractured edges.

RESULTS AND DISCUSSION

Microstructure of calcium phosphate specimens

Representative SEM photomicrographs of the as-sintered, polished and thermally etched surfaces of HA, β-TCP and BCP specimens are shown in Figs. 1 to 3. The line-intercept method was used to assess the grain size of these materials yielding values of 7.9 ± 1.5 μm for HA, 2.9 ± 0.6 μm for β-TCP and 1.3

± 0.1 μm for BCP. The density of the samples was measured using Archimedes method resulting in densities of 97.7% ± 0.7%, 63.9% ± 3.2% and 69.1% ± 1.4% for HA, β-TCP and BCP, respectively. The trend in relative density and grain size in the CaP specimens is consistent with the general observation that during processing of ceramic powders, densification typically proceeds with limited grain growth up to a relative density of about 0.9 and at higher relative densities, grain growth accelerates [33-36].

Broad peaks in the XRD patterns (data not shown) for the unsintered HA, BCP and β-TCP powders likely are due to the small particle size of the starting powders. Diffraction peaks were much sharper for the sintered specimens. The minor phases observed were α-TCP and β-TCP for the HA discs and α-TCP and HA for the β-TCP discs. For BCP, minor phases of HA and β-TCP, and α-TCP were present. The HA/β-TCP discs were determined to be 61% HA using

$$\%HA = \frac{I_{100,HA}}{I_{100,HA} + I_{100,\beta-TCP}} * 100 \qquad (2)$$

where $I_{100,\ HA}$ and $I_{100,\beta\text{-TCP}}$ are the intensities of the maximum intensity peaks of HA and β-TCP, respectively [37].

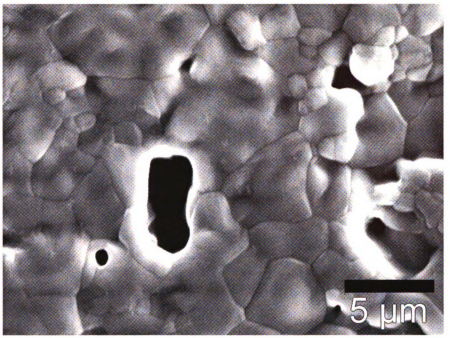

Figure 1: SEM micrograph of polished and thermal etched hydroxyapatite (5000x).

Microcracking in HA specimens

Porosity can suppress TEA-induced microcracking in ceramics when the volume fraction porosity (VFP) exceeds roughly 20% - 30% [14]. Since the β-TCP and BCP specimens included in this study have a VFP of about 31% and 39%, respectively, it is unsurprising that microcracks were not observed in these calcium phosphates.

In contrast, the SEM micrographs of the as-sintered HA surfaces (Figs. 4-6) clearly show microcracking. The microcracking is abundant and not correlated with areas of porosity, rather it is uniform across the HA surface. A careful examination of the micrographs illustrates that the microcracks are associated with what appear to be separated grain boundaries, emerging from the grain boundary corners to continue into adjacent grains as noted by the arrows. The

maximum crack opening displacement is roughly 0.35 μm with an average microcrack length of approximately 12.5 ± 9.9 μm.

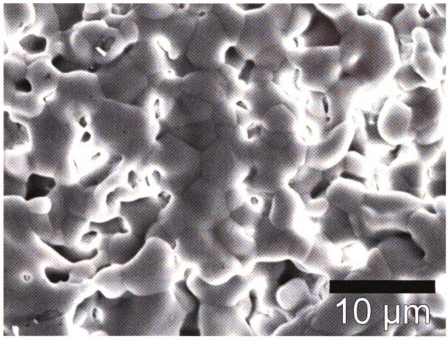

Figure 2: SEM micrograph of polished and thermal etched β-TCP (3000x).

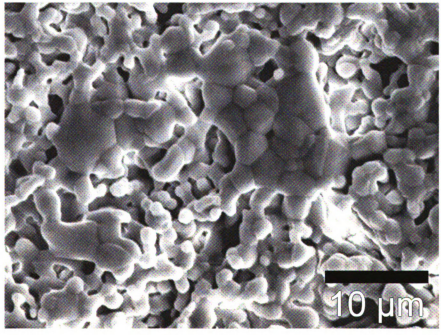

Figure 3: SEM micrograph of polished and thermal etched BCP (3000x).

For the as-sintered surface of the HA specimens sectioned by fracture (Fig. 4), microcracks transverse the grains (white arrows) and run along the grain boundaries (black arrows). Some of the microcracks that transverse grains appear to be connected to the grain boundary microcracks. For the as-sintered surface of the HA specimens sectioned by cutting (Figs. 5 and 6), the microcrack damage was similar to that observed in Fig. 4 for the specimen sectioned by fracture. Figs. 5 and 6 represent two different areas on a single specimen. Therefore, the microcrack damage appears to be independent of sectioning technique and in each of Figs. 4-6, the microcrack damage is quite similar.

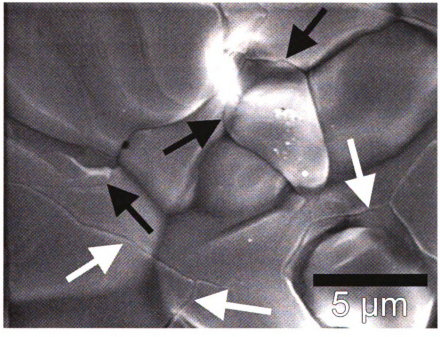

Figure 4: SEM micrograph of as-sintered hydroxyapatite specimen surface. Image was taken away from the fracture surface (6500x).

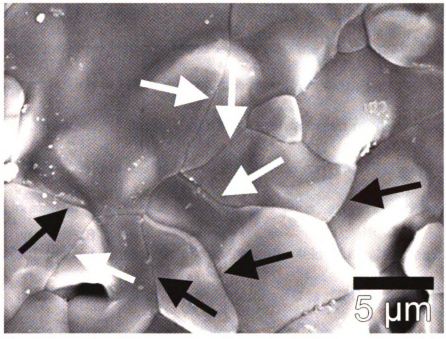

Figure 5: SEM micrograph of as-sintered hydroxyapatite specimen surface shown in Fig. 5. Image was taken away from the fracture surface (4500x) and at different location on the specimen.

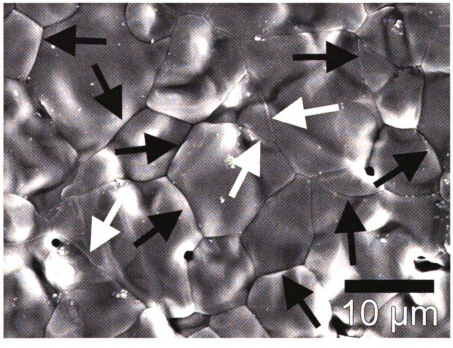

Figure 6: SEM micrograph of as-sintered hydroxyapatite specimen surface. Image was taken away from the fracture surface (2500x).

A re-evaluation of key results from the literature on microcracking in HA

As discussed by Hoepfner and Case [38], the critical grain size for TEA induced microcracking in HA is difficult to estimate, in large part due to the large uncertainty in the value of $\Delta\alpha_{max}$ that arises from a broad range of single crystal thermal expansion values found in the literature. From Eq. (1), we see that the critical grain size is proportional to $1/(\Delta\alpha_{max})^2$. Thus, as reviewed by Hoepfner and Case [38], the available x-ray diffraction data yields $\Delta\alpha_{max}$ values for HA that vary by as much as a factor of 10, and therefore it is difficult to make a precise estimate of HA's critical grain size. (Hoepfner and Case [38] base an estimate of G_{CR} on the value of $\Delta\alpha_{max}$ that is most consistent with the average thermal expansion values.)

For the HA literature, damage that has been attributed to other mechanisms can perhaps be attributed to TEA-induced microcrack damage. For example, in a study of sintered HA, Ruys et al. [39] observed that as the specimen density increased from that of the original powder compact to a relative density of ~ 0.95, the specimens' fracture strength increased monotonically. However, beginning at a relative density of about 0.95, the fracture strength dropped with further increases in density. Ruys et al. [39] attributed the observed strength decrease to dehydroxylation of the HA (where dehydroxylation refers to the loss of hydroxyl groups during heating, which can lead to the decomposition of HA to oxyhydroxyapatite or in the extreme, to TCP [2].)

To evaluate the concept advanced by Ruys et al. [39] that dehydroxylation during sintering was responsible for the microcracking observed in their HA

specimens, it is critical that we examine several aspects of sintering, including the generation of volatiles during sintering and related questions of the evolution of pore shape, pore size and grain size during sintering. In general, it is true that if volatiles are generated during sintering (via mechanisms such as thermal decomposition [36, 40] or debinding [41]) then those volatiles must be removed before local pore closure commences, otherwise pressure from the encapsulated gases can result in cracking, bloating and blistering of the sintered component [36, 40, 41].

However, it is important to note that the initiation of local pore closure is just one step along the evolutionary path experienced by the ceramic compact as pore shape, pore size and grain size change during sintering [33-36]. In particular, the process of local pore closure begins early in the intermediate stage of sintering (at relative density, ρ, values of approximately 0.7 to 0.8 [33]) as tubular pores along the grain edges begin pinching off into closed, spherical pores. When the sintered component reaches a ρ value of about 0.9 to 0.95, the intermediate stage of sintering is complete and essentially the entire inventory of pores within the specimen has pinched off into isolated spherical pores [33-36].

Thus, for the sake of interpreting the experimental results of Ruys et al. [39], it is critical to distinguish between (1) the beginning of the pore pinch-off process (at roughly $0.7 < \rho < 0.8$) which can lead to cracking due to entrapped gases and (2) the end of the pore pinch-off process at ρ values of about 0.9 to 0.95. If dehydroxylation did spawn the microcracks in the HA specimens studied by Ruys et al. [39], then the microcracking (and possibly blistering and bloating of

the specimens) would have likely commenced at the relatively modest ρ values of 0.7 to 0.8, rather than at the much higher ρ value of 0.95 at which Ruys et al. [39] actually observed both the microcracking and the associated drop in strength.

These considerations of pore pinch-off and microcracking beg the following question, "If dehydroxylation did not cause the microcracking observed by Ruys et al. [39] for their HA specimens with densities > 0.95, then what did"? The answer likely is again found within the context of microstructural evolution during sintering, namely the widely observed phenomenon that grain growth accelerates when the sintered compact reaches a ρ value of about 0.90 to 0.95 [42-45].

As depicted in Fig. 7, during the initial and intermediate stages of sintering, considerable densification occurs (especially during the intermediate stage). Despite the densification, very little grain growth occurs until the end of the intermediate stage. Thus for densities below $\rho \sim 0.90$, grains in the densifying specimen are roughly comparable in size to the powders that made up the original powder compact [44]. Only at the onset of the final stage of sintering (at a relative density of ~ 0.90 - 0.95) does grain growth accelerate dramatically (Fig. 7). This behavior was been widely observed in metals and ceramics, for example, in powder compacts of TiO_2 [42], Al_2O_3, BeO, ZnO and copper [43], MgO-doped alumina [44] and silica doped, ultrapure Al_2O_3 [45].

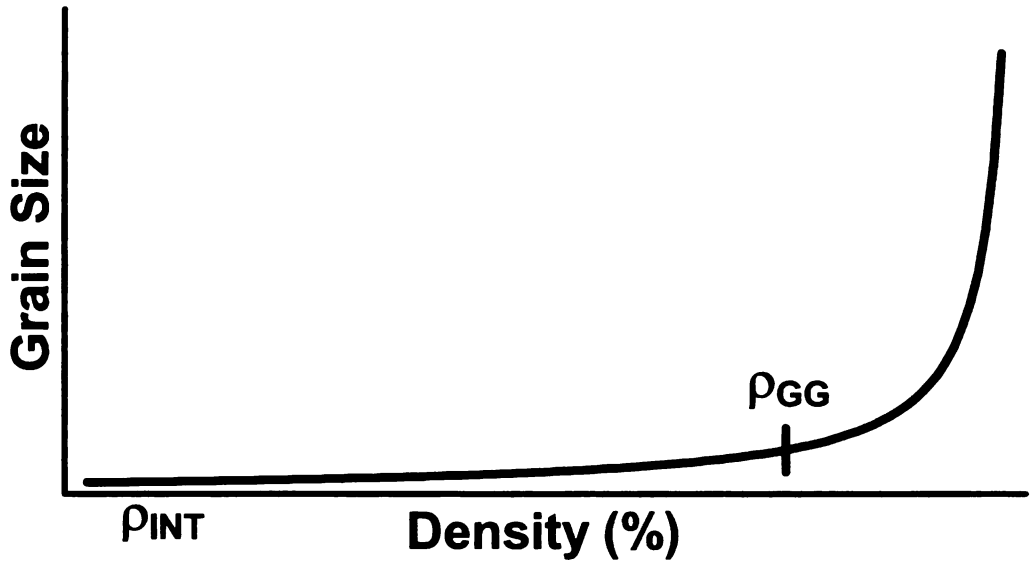

Figure 7: Schematic showing the relationship between relative density and grain size for ceramic powders.

Thus, in the study by Ruys et al. [39], at a relative density of about 0.95 the grain growth process likely accelerated such that the grain size G became larger than the critical grain size G_{CR}. In general, for $G > G_{CR}$, microcracking ensues and the strength and fracture toughness drop, which also is consistent with the particular observations recorded for HA by Ruys et al. [39]. Given these considerations of pore/grain size evolution during sintering, it is likely that the microcracking observed in HA by Ruys et al. [39] was due to TEA-induced stress rather than dehydroxylation.

In addition to the Ruys et al. paper [39], another paper from the literature that is critical to examine is one by Halquani et al. [46] concerning microcracking in HA. Although Halquani et al. [46] made strength and fracture toughness measurements on HA specimens that are consistent with the presence of microcrack-induced damage, there are some questions associated with their

microscopy of the surface features they identified as TEA-generated microcracks.

Via hot pressing, Halquani et al. [46] obtained nearly-dense polycrystalline HA specimens with grain sizes ranging from roughly 0.15 -1.2 μm. Two grain-size-dependent regimes of mechanical behavior were observed. For G < 0.4 μm, the fracture strength, σ, increased monotonically from σ ~ 75 MPa (grain size of 0.15 μm) to a maximum strength of σ = 137 MPa (grain size of 0.4 μm). Thus, the strength (σ) increased by about 83% over the grain size interval from 0.15 μm to 0.4 μm. In contrast, for G > 0.4 μm, σ decreased monotonically from the maximum at G = 0.4 μm to a σ of ~100 MPa at G = 1.2 μm. Also at a grain size of 0.4 μm, the fracture toughness, K_C, passed through a maximum, although the maximum K_C value of 1.2 $MPam^{1/2}$ was only roughly 20% larger than the K_C values at the smallest and the largest grain sizes.

Halquani et al. [46] interpreted the maximum in both fracture strength and fracture toughness as being due to TEA-induced microcracking with a critical grain size of about 0.4 μm. However, Halquani et al. [46] only identified structures they interpreted as being microcracks on the fracture surfaces of their HA specimens. Furthermore, the microstructural features that Halquani et al. [46] identify as microcracks in fact seem very similar to cleavage steps that are nearly always present on the transgranular fracture surfaces in brittle materials. Furthermore, Halquani et al. [46], state that microcracks in their HA specimens

are difficult to observe since they "can only be seen when perpendicular to the rupture plane on a mirror area (i.e. on regions of transgranular failure)". Thus, it is possible that the features identified as microcracks by Halquani et al. [46] may actually be cleavage steps.

In contrast to the Halquani et al. study [46], in this study, the micrographs that document the microcracks in our HA specimens (Figs. 4-6) were taken on the as-sintered specimen surfaces, thus avoiding the possible complication of fracture-surface artifacts. Thus, the micrographs presented in this study (Figs. 4-6) are the first unequivocal evidence for microcracking in polycrystalline HA to appear in the literature.

If we continue to examine the observations of Halquani et al. [46], we find that the magnitude of the fracture toughness increase in HA observed by Halquani et al. [46] is consistent with other researchers' theoretical calculations and experimental observations of TEA-stress and microcracking induced changes in ceramics. For example, for specimens with grain sizes smaller than the critical grain size, Shum [47] calculated that stresses produced by thermal expansion anisotropy and elastic anisotropy stresses can increase the fracture toughness by up to about 1.3 or perhaps as much as 3 in some cases. In Sarno and Tomozawa's [48] study of a TEA-induced microcracking in a zirconia-lithium aluminosilicate glass ceramic , the experimentally-determined increases in fracture toughness are of the same magnitude that Shum predicts for $G < G_{CR}$. As was the case for the HA specimens studied by Halquani et al. [46], for $G > G_{CR}$ the Sarno and Tomozawa [48] glass ceramic materials experienced a

dramatic decrease in toughness accompanied by a fracture strength that dropped to essentially zero. Similar behavior (that is a rise in strength and fracture toughness for $G < G_{CR}$ and a drop for $G > G_{CR}$) also has been observed for TEA-induced behavior in alumina, TiO_2, iron titanate, and Nb_2O_5 [15].

In addition to TEA as the mechanism for inducing microcracks in CaP materials, two additional mechanisms to be considered are (i) thermal shock [10, 49] and (ii) thermal expansion mismatch [10, 50, 51]. For thermal shock, the stresses required for microcracking are generated by a rapid change in the specimen's ambient temperature [10, 49]. In this study, the rate of change in ambient temperature is relatively modest, in that the most rapid temperature changes experienced by the specimens occur during processing when the specimens are heated at ~10°C/min up to the sintering temperature, followed by cooling, again at about 10°C/min to room temperature. As calculated by Halquani et al. [46], our cooling rate is not sufficient to induce the microcracking observed in the HA specimens included in this study.

Additionally, microcracking may be generated by thermal expansion mismatch, which is similar to TEA, except that thermal expansion mismatch involves the differing coefficients of thermal expansion between two or more phases in a given material [10, 51]. Thermal expansion mismatch microcracking has been both modeled theoretically [51] and observed experimentally in a variety of ceramic systems [50, 52-54]. To investigate the possibility that thermal expansion mismatch caused microcracking in, for example, HA specimens with a minor β-TCP phase, we can examine studies of BCP (biphasic calcium

phosphate - HA/β-TCP) materials. As an example, for hot-pressed BCP (90 wt% HA/10 wt% β-TCP) specimens having a homogeneous distribution of β-TCP grains within the HA matrix, Raynaud et al. [55] obtained a fracture strength of 150 MPa, which was double the strength Raynaud et al. measured in the same study [55] for similarly prepared pure HA specimens. Thus, Raynaud et al.'s [55] two-phase mixture of HA/β-TCP was obviously not badly microcracked, compared to the pure HA. Otherwise, the BCP strength would have been lower than that of the strength of the pure HA specimens. Furthermore, based on the x-ray diffraction results, the β-TCP phase fraction was likely less than 10% for the HA specimens included in this study. Thus, for HA specimens with a minor β-TCP phase (such as those in this study), thermal expansion mismatch induced stresses are not likely to result in significant microcracking,

Since thermal shock, thermal expansion mismatch and dehydroxylation are unlikely sources of microcracking for the specimens in this study, and because HA is known to crystallize in a non-cubic atomic lattice, the likely source of the microcracks observed in our specimens is therefore TEA.

CONCLUSIONS AND SUMMARY

HA is an important biomedical material. Although HA should display thermal expansion anisotropy, the existence and effects of TEA-induced microcracking are somewhat uncertain based on the current literature. For example, microcracking in HA was attributed to dehydroxylation by Ruys et al.

[39], although given considerations of microstructural evolution; the observations are more consistent with microcracking due to TEA. Also, while Halquani et al. [46] presented micrographs of surface features that they interpreted as TEA-induced microcracks, Halquani et al. stated that these features were only observed on the surfaces of HA grains that had been fractured transgranularly.

In contrast, in this study, microcracks in HA are presented for a series of specimens with as-sintered surfaces, to avoid the complication of attempting to separate surface features induced by TEA-microcracks from those features generated during the macrofracture of the specimen. Furthermore, building upon a close examination of the HA studies by Ruys et al. [39] and Halquani et al. [46], we have employed pertinent literature on sintering in ceramics and microcracking in ceramics to construct arguments that the observations of Ruys et al. [39] and Halquani et al. [46] strongly support the case for TEA-induced microcracking in HA. The micrographs included in this study (Figs. 4-6) bolster those arguments.

A difficulty in developing HA for biomedical use has been, in part, the fact that its properties can vary greatly from researcher to researcher as a result of for example, differences in sintering temperature or heat treatments [39, 46, 55]. Property changes that are associated with TEA-induced microcracking have been studied widely in the general ceramics literature [5-8, 10]. Putting the dizzying variation of properties into context (that is, with the observation that TEA-induced stresses and microcracking may play a major role in the variability

of properties) is a significant step toward fully utilizing hydroxyapatite as a biomedical material, specifically for use as a scaffold in bone tissue engineering.

ACKNOWLEDGMENTS

The authors acknowledge J.A. Meganck (graduate of the Michigan State University Mechanical Engineering Department) and M. Soto (a graduate of the Chemical Engineering and Materials Science (CHEMS) Department at MSU) for their assistance in this study with sample preparation and XRD studies. The authors gratefully acknowledge funding from the National Science Foundation (DMR0074439) and the MSU Foundation for support of I.O. Smith as well as for equipment and space in the MSU College of Engineering's new Tissue Engineering laboratories.

REFERENCES

[1] J. F. Nye, Physical properties of crystals, their representation by tensors and matrices, Clarendon Press, Oxford, 1985, p. 22-23, 131-149.

[2] J. C. Elliot, Structure and chemistry of the apatites and other calcium orthophosphates, Elsevier Science, Amsterdam, 1994, p. 29.

[3] D. E. C. Corbridge, Phosphorus: An outline of its chemistry, biochemistry, and technology, Elsevier Science, Amsterdam, 1995, p. 455.

[4] Y. Suetsugu, T. Ikoma, J. Tanaka, Key Eng Mat 192 (2001) 287-290.

[5] J. A. Kuszyk, R. C. Bradt, J Am Ceram Soc 56 (1973) 420-423.

[6] J. J. Cleveland, R. C. Bradt, J Am Ceram Soc 61 (1978) 478-481.

[7] E. D. Case, J. R. Smyth, O. Hunter, Mater Sci and Eng 51 (1981) 175-179.

[8] E. D. Case, J. R. Smyth, O. Hunter, J Nuclear Mater 102 (1981) 135-142.

[9] J. J. Mecholsky, Toughening in glass ceramics through microstructural design, fracture mechanics of ceramics, Plenum Press, New York, 1981, p. 15-17.

[10] E. D. Case, The saturation of thermomechanical fatigue in brittle materials, WIT Press, Southampton, UK, 2002, p. 137-208.

[11] S. W. Paulik, M. H. Zimmerman, K. T. Faber, E. R. Fuller, J Mater Res 11 (1996) 2795-2803.

[12] E. D. Case, J. R. Smyth, O. Hunter, Microcrack healing during temperature cycling of single phase ceramics, Plenum Press, New York, 1983, p. 507-530.

[13] Y. Fu, A. G. Evans, W. M. Kriven, J Amer Ceram Soc 67 (1984) 626-630.

[14] W. R. Manning, O. Hunter, Jr., J. W. Calderwood, D. W. Stacy, J Am Ceram Soc 55 (1972) 342-347.

[15] R. W. Rice, J Mater Sci 31 (1996) 1969-1983.

[16] A. G. Evans, K. T. Faber, J. Amer. Ceram. Soc. 67 (1984) 255-260.

[17] E. D. Case, J. R. Smyth, O. Hunter, J Mater Sci 15 (1980) 149 153.

[18] D. P. H. Hasselman, J. Amer. Ceram. Soc. 76 (1993) 2180-2184.

[19] M. Hirai, J. Nuclear Mater. 173 (1990) 247-254.

[20] S. Mori, D. B. Burr, Bone 14 (1993) 103-109.

[21] P. Muir, K. A. Johnson, C. P. Ruaux-Mason, Bone 25 (1999) 571-576.

[22] G. C. Reilly, J. D. Currey, A. E. Goodship, J Orthop Res 15 (1997) 862-868.

[23] M. W. Stepnik, C. L. Radtke, M. C. Scollay, P. E. Oshel, R. M. Albrecht, E. M. Santschi, M. D. Markel, P. Muir, Vet Surg 33 (2004) 2-10.

[24] C. L. Radtke, N. A. Danova, M. C. Scollay, E. M. Santschi, M. D. Markel, T. D. Gomez, P.Muir, AJVR 64 (2003) 1110-1116.

[25] V. Bentolila, T. M. Boyce, D. P. Fyhrie, R. Drumb, T. M. Skerry, M. B. Schaffler, Bone 23 (1998) 275-281.

[26] D. B. Burr, M. R. Forwood, D. P. Fyhrie, R. B. Martin, M. B. Schaffler, C. H. Turner, J Bone Miner Res 12 (1997) 6-15.

[27] D. B. Burr, Bone 30 (2002) 2-4.

[28] K. A. Johnson, G. A. Skinner, P. Muir, AJVR 62 (2001) 787-793.

[29] D. L. Wheeler, K. E. Stokes, H. M. Park, J. O. Hollinger, J Biomed Mater Res 35 (1997) 249-254.

[30] L. D. Quarles, D. D. Yohay, L. Lever, R. Canton, R. Wenstrup, J Biomed Mater Res 7 (1992) 683-692.

[31] D. J. Mooney, A. G. Mikos, Scientific American 280 (1999) 60-67.

[32] R. Z. LeGeros, S. Lin, R. Rohanizadeh, D. Mijares, J. P. LeGeros, J Mat Sci: Mat Med 14 (2003) 201 - 209.

[33] R. M. German, Sintering theory and practice, John Wiley and Sons, New York, 1996, p. 99-101.

[34] R. M. German, Powder Metallurgy Science, Metal Powders Industries Federation, Princeton, 1994, p. 244-259.

[35] M. W. Barsoum, Fundamentals of Ceramics, McGraw-Hill, New York, 1997, p. 411 - 416.

[36] D. W. Richerson, Modern Ceramic Engineering, Marcel Dekker, Inc., New York, 1992, p. 549 - 550.

[37] J. M. Toth, W. M. Hirthe, W. G. Hubbard, W. A. Brantley, K. L. Lynch, J Appl Biomater 2 (1991) 37-40.

[38] T. P. Hoepfner, E. D. Case, Materials Letters 58 (2004) 489-492.

[39] A. J. Ruys, M. Wei, C. C. Sorrell, M. R. Dickson, A. Brandwood, B. K. Milthorpe, Biomaterials 16 (1995) 409-415.

[40] W. D. Kingery, H. K. Bowen, D. R. Uhlmann, Introduction to Ceramics, Wiley, New York, 1976, p. 504 - 505.

[41] M. N. Rahaman, Ceramic Processing and Sintering, Marcel Dekker, Inc., New York, 2003, p. 416 - 418.

[42] M. F. Yan, Mater. Sci. and Eng. 48 (1981) 55 - 72.

[43] T. K. Gupta, J. Am. Ceram. Soc. 55 (1972) 276 - 277.

[44] K. A. Berry, M. P. Harmer, J Am Ceram Soc 69 (1986) 143-149.

[45] I.-J. Bae, S. Baik, J. Am. Ceram. Soc. 80 (1997) 1149 - 1156.

[46] R. Halquani, D. Bernache-Assolant, E. Champion, A. Ababou, J. Mater. Sci. Mater. Med. 5 (1994) 563 - 568.

[47] D. K. M. Shum, J. Mater. Sci. Mater. Med. 30 (1995) 5281-5286.

[48] R. D. Sarno, M. Tomozawa, J. Mater. Sci. Mater. Med. 30 (1995) 4380-4388.

[49] W. J. Lee, E. D. Case, Mater Sci and Eng A119 (1989) 113-126.

[50] R. W. Davidge, D. J. Green, J. Mater. Sci. Mater. Med. 3 (1968) 629-634.

[51] A. Zimmermann, E. R. Fuller, J. Rodel, Materials Science Forum 347 (2000) 211- 216.

[52] J. Luo, R. Stevens, J. European Ceram. Soc. 48 (1997) 1565-1572.

[53] M. Kon, W. J. O'Brien, S. T. Rasmussen, K. Asaoka, J. Dent. Res. 80 (2001) 1758 - 1763.

[54] J. R. Mackert, S. W. Twiggs, C. M. Russell, A. L. Williams, J. Dent. Res. 80 (2001) 1574-1579.

[55] S. Raynaud, E. Champion, J. P. Lafon, D. Bernache-Assollant, Biomaterials 23 (2002) 1081 - 1089.

CHAPTER 6

INDUCED MICROCRACKING AFFECTS OSTEOBLAST ATTACHMENT ON HYDROXYAPATITE SCAFFOLDS FOR TISSUE ENGINEERING

I.O. SMITH, M.J. BAUMANN, E.D. CASE
Department of Chemical Engineering and Materials Science, College of Engineering, Michigan State University, 2527 Engineering Building, East Lansing, Michigan, 48824, USA

PUBLISHED IN: J Am Biochem Biotechnol 2006;2:105-110.

ABSTRACT

Bone microdamage caused by routine activity plays an important role in triggering targeted and nontargeted bone remodeling. Targeted remodeling occurs near localized areas of microdamage[1-4]. We hypothesize that bone remodeling may be directly and positively influenced by inducing microcracks in hydroxyapatite (HA) scaffolds for bone tissue engineering. A study by Case et al. showed microcracking in HA discs having >98% theoretical density[5]. These microcracks occurred without the application of external stress, likely as a result of thermal expansion anisotropy (TEA). TEA generates microcracks only when the specimen grain size exceeds a critical value (G_{CR}). Due to conflicting data in the literature on the thermal expansion along the crystallographic axes of HA, it is difficult to estimate G_{CR} precisely for HA, but G_{CR} likely ranges from a few tenths of microns to several microns[6]. As the grain size of a polycrystalline specimen increases above the critical grain size, the number of microcracks also increases but the number density of microcracks is difficult to control. Therefore, in this study we used Vickers microindentation to induce controlled microcracks in

>99% dense HA discs. The effect of microcracking on the osteoblast (OB) attachment was then quantified. Control HA discs and microcracked HA were seeded with MC3T3-E1 OBs and cultured for 4 hours. The OBs were then stained with Rhodamine-Phalloidin and Hoechst fluorescent dyes to identify the actin fibers and nuclei, respectively. OB attachment was quantified using fluorescent light microscopy. OB attachment at 4 hours was 29% ± 7.6% of the initial seeded OBs for the microcracked HA specimens and 18% ± 6.1% of initial seeded OBs for the non-microcracked control HA specimens. The difference in these OB attachment values was statistically significant as determined via the Student t-test ($p = 0.004$, with $p < 0.05$ taken to indicate significance).

INTRODUCTION

Microcracking in Bone

In a 1960 study of cracks located primarily in the cement line of human rib bones, Frost[7] first suggested that microcracking in bone results from mechanical fatigue. These cracks were not exclusively an artifact of specimen preparation, but rather an inherent characteristic of the bone. More recently, similar cracks have been observed in human[8-10], bovine[10,11], canine[1,12] and equine bone[13,14]. Zioupos et al. report the size of these cracks as 10 – 50 μm in length with an apparent opening of 2 – 5 μm[11].

Bone exposed to routine activity undergoes repeated cyclic strain, on the order of 0.0003 to 0.0008 and 0.0008 to 0.0012 for walking and running, respectively[15, 16]. While these values are lower than the maximum strain allowed by bone in a single cycle, their repetitive nature leads to an accumulation of microcracks[17]. Left unchecked, this microdamage coalesces into macrocracks that can cause failure of the bone[8,18,19]. The process of microcrack accumulation to produce macrocracks is especially pronounced in aged individuals[9]. Frost also suggested a relationship between bone microcracking and subsequent bone remodeling[7]. Microdamage in bone likely triggers both targeted and nontargeted remodeling[20]. Nontargeted remodeling is not site dependant and occurs less frequently[21], while targeted remodeling occurs at sites of localized microdamage as observed in studies by Johnson et al., Burr et al. and Mori et al.[2-4, 13]. In these cases, remodeling was significantly more focused around regions of microdamage[22]. Remodeling

occurs when osteoclasts resorb damaged bone, including osteocytes[22]. The resorption process is regulated by the osteocyte syncytium in local regions of remodeling[23-25]. Osteocyte damage and subsequent apoptosis leads to increased osteoclast activity followed by subsequent osteoblast activity. Because microcracks occur with routine fatigue loading, the dynamic repair of microdamage is therefore an integral part of maintaining the integrity of the bone[2].

Microcracking in Hydroxyapatite

Case et al. were the first to definitively identify microcracking in dense (>98% theoretical density) HA which occurred in the absence of an external applied stress[5]. This microcracking was likely a result of thermal expansion anisotropy (TEA), since non-cubic crystalline materials such as HA have dissimilar thermal expansion coefficients along the crystallographic axes. As a polycrystalline body cools following sintering, TEA causes neighboring grains to shrink at differing rates and in turn generates a stress that is sufficient to cause microcracking if the mean grain size exceeds a critical grain size, G_{CR}. Although TEA generated microcracks were observed in the dense HA specimens (average grain size of 7.9 μm ± 1.5 μm) examined by Case et al.[5], it is difficult to precisely estimate G_{CR} for HA. As discussed by Hoepfner et al., there are large disparities among the values reported in the literature for the thermal expansion coefficient as a function of crystallographic direction, which lead to large uncertainties in calculating G_{CR} for HA[6].

In general, the number density of microcracks increases with increasing grain size, but in the absence of extensive measurements, it is difficult to precisely predict changes in TEA-induced microcracks. Furthermore, there is no control over the spatial distribution of TEA-induced microcracks. Therefore in our HA specimens, in order to control both the number density and placement, microcracks were induced by Vickers micro-indentation where the microcrack length was controlled by varying the indentation load. The following relationships were used to predict the microcrack length (2c) and the indentation impression diagonal length (2a)

$$K_C = \alpha\left(\frac{E}{H}\right)^{1/2}\left(\frac{P}{C^{3/2}}\right) \qquad (1)$$

$$H = 1.8544\left(\frac{P}{2a^2}\right) \qquad (2)$$

where K_C is fracture toughness, E is elastic modulus, H is hardness, P is indentation load, and α is a calibration constant, using values of K_C = 1 MPa$\sqrt{m}$, E = 115 GPa and α = 0.016[26, 27].

The array of Vickers indentations resulted in an areal distribution of microcracks. Cell counting was used to quantify OB attachment on both the microcracked and the nonmicrocracked HA specimens. The effect of microcracking on OB morphology was assessed by direct observation using optical fluorescence microscopy. A spindle shaped or polygonal spread OB

morphology was then used as an indicator of typical OB attachment to the HA specimen surfaces[28-31].

MATERIALS AND METHODS

Powder processing

Dense HA discs were fabricated using high purity powder (Taihei Chemical, Osaka, JP) with a vendor-specified mean particle size of 1 - 3 μm. In a binderless process developed by McMullen, HA powder was uniaxially pressed into discs at 35 MPa for 1 minute using a KBr pellet die (International Crystal Laboratories, Garfield, NJ) or a hydraulic press (Carver Inc, Wabash, IN)[32]. The resulting HA powder discs (diameter = 32 mm, thickness = 2 – 3 mm) were sintered in air at 1360°C for 4 hours, at a heating/cooling rate of ~10°C/minute resulting in HA discs of 23 mm in diameter and 1 - 2 mm in thickness and >99% theoretical density as determined by Archimedes method (n = 5). The sintered HA specimen grain size was 4.8 μm ± 1.0 μm, determined by the line-intercept method (n = 5).

The surfaces of the HA discs were ground flat using 30 μm (600 grit) SiC wet abrasive paper and then all were sequentially polished using 30 μm, 12 μm, 9 μm, 6 μm and 1 μm diamond abrasive suspension or paste for 5 minutes at each grade. A Buehler EcoMet 3 variable speed grinder/polisher and an AutoMet 2 power head were used to grind and polish. Polished specimens were ultrasonically cleaned by submersion in reverse osmosis

(RO) water followed by pulsing with an ultrasonic probe at 20 kHz and 250 Watts for 5 minutes.

Microcrack Induction

Surface-breaking microcracks were induced by indenting each specimen 196 times using a Buehler Micromet II microindenter (Buehler, Lake Bluff, IL), with a load of 4.9 N, a load time of 5 seconds and a loading rate of 70 μm/sec. These loading parameters were found by the authors to be the optimum set of conditions for inducing microcracks with minimal spalling and chipping of the HA specimens.

Indentations were made over a single 14 mm x 14 mm grid, with a one mm indentation spacing, across each specimen surface. The square-based pyramidal diamond indenter tip used for Vickers indentations creates diamond-shaped impressions on the HA disc surface. Microcracks are formed by the radial cracks originating from the corners of these indentation impressions (See Figure 1, where white arrows indicate radial cracks). Following indentation, each HA disc was submerged in RO water for 8 hours to insure crack growth saturation. The average indentation size and crack size were determined by optical microscopy for a representative selection of indentations (n = 20) on each HA specimen. A preliminary study of the effect of HA specimen immersion in RO water was conducted, in which 8 indentations were applied to a single dense HA disc, which was submerged in RO water, to determine the effectiveness of this treatment in assisting crack

growth. Crack length was measured at t = 30 seconds immediately following indentation, as well as at submersion times of 8 and 24 hours. The results of this trial are mentioned in addition to the average indent size and post-saturation crack length in the results section.

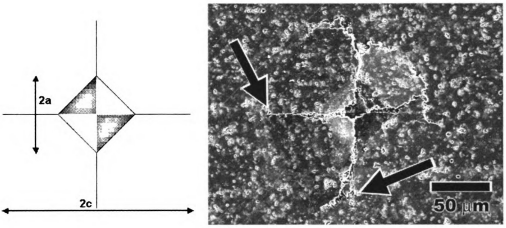

Figure 1: SEM micrograph of microindentation on HA specimen surface (right). "2a" indicates the diagonal length of the indentation impression and "2c" indicates crack length (left).

MC3T3-E1 culture

MC3T3-E1 osteoblasts (OBs) of subclone 14, obtained from ATCC (Manassas, VA) were thawed and plated. The OBs were cultured using alpha minimum essential media (α-MEM, Invitrogen Grand Island, NY) supplemented with 10% fetal bovine serum (FBS, Atlanta Biologicals, Lawrenceville, GA), incubated in a humid atmosphere at 37°C and 5% CO_2. The OBs were split regularly with cell passages 25-29 used for this study.

OB attachment study

Microcracked HA and control HA disc specimens were autoclave sterilized, collared and placed into 6-well polystyrene cell culture plates in preparation for OB seeding. Prior to seeding, OBs were removed by trypsinization (Trypsin/EDTA, Invitrogen, Grand Island, NY), counted with a hemacytometer, centrifuged and resuspended in fresh complete α-MEM. Following standard procedures, OBs were seeded onto the HA discs at a density of 11,320 cells/cm^2 and enough media was added to account for evaporation[33]. After 4 hours incubation at 37°C and 5% CO_2 in a humid environment, the media was removed and each HA specimen washed using 1X phosphate buffered saline (PBS), to remove any non-attached OBs. OB seeding was done in triplicate, with n = 3 for a total of nine microcracked HA and nine control HA specimens.

OBs were fixed using 3.7% formaldehyde (H_2CO) (JT Baker, Phillipsburg, NJ) and permealized with a solution of 0.1% Triton X-100 (Sigma-Aldrich, St. Louis, MO). Prior to staining, OB seeded HA specimens were pre-incubated in 1% bovine serum albumin (BSA, Invitrogen).

The actin cytoskeleton was stained using Rhodamine-Phalloidin while the nucleus was stained using Hoechst 33342 stain (Invitrogen)[32]. Stained OB seeded HA specimens were mounted in glycerol solution (JT Baker) and viewed using a Leica DM IL fluorescence microscope (Leica Microsystems, Wetzlar, GER) and optical micrographs recorded using the Spot RT camera (Diagnostic Instruments, Inc., Sterling Heights, MI). Rhodamine-Phalloidin

stain fluoresces at a wavelength of $\lambda_{emmision}$ = 565 nm when exposed to light of wavelength $\lambda_{excitation}$ = 542 nm while the Hoechst stain fluoresces at a wavelength of $\lambda_{emmision}$ = 465 nm when exposed to light with wavelength of $\lambda_{excitation}$ = 355 nm.

OB attachment was quantified by counting nuclei over the microscope's field of view. Ten fields of view were randomly selected and counted for each specimen. The student's t-test was used to determine statistical significance, with $p < 0.05$ taken as significant.

The effect of induced microcracking in HA specimens on OB morphology was assessed by staining the actin fibers and observing the OB shape using optical fluorescence microscopy.

RESULTS AND DISCUSSION

Vickers indentation impressions in the dense HA specimens had an average diagonal length $2a_{AVE}$ = 54.7 μm ± 3.6 μm (Fig. 1). After crack saturation, the mean crack length was $2c_{AVE}$ = 176.3 μm ± 23.8 μm (Fig. 1).

Immersing microcracked HA specimens in RO water resulted in an increase in crack length from 143 μm ± 23.8 μm to 158 μm ± 17.4 μm after 8 hours and to 167 μm ± 14.0 μm after 24 hours (n = 8). This is consistent with previous findings that H_2O assists crack growth[34]. Student t-test determined that the increase in microcrack length between 8 and 24 hours was not significant.

Figure 2 is a plot of OB attachment at four hours for microcracked HA specimens (n = 9) and control HA specimens with no microcracking (n = 9), showing the significant difference in OB attachment between the two. Error bars indicate standard deviation. After 4 hours in culture, OB attachment on the microcracked HA specimens was 29% ± 7.6% of initial seeded OB number compared to 18% ± 6.1% of initial on the control HA specimens. This represents a 60% increase in OB attachment with microcracking. Student's t-test produced a p-value of 0.004, presence of microcracks on the HA surface had a positive and significant influence on OB attachment.

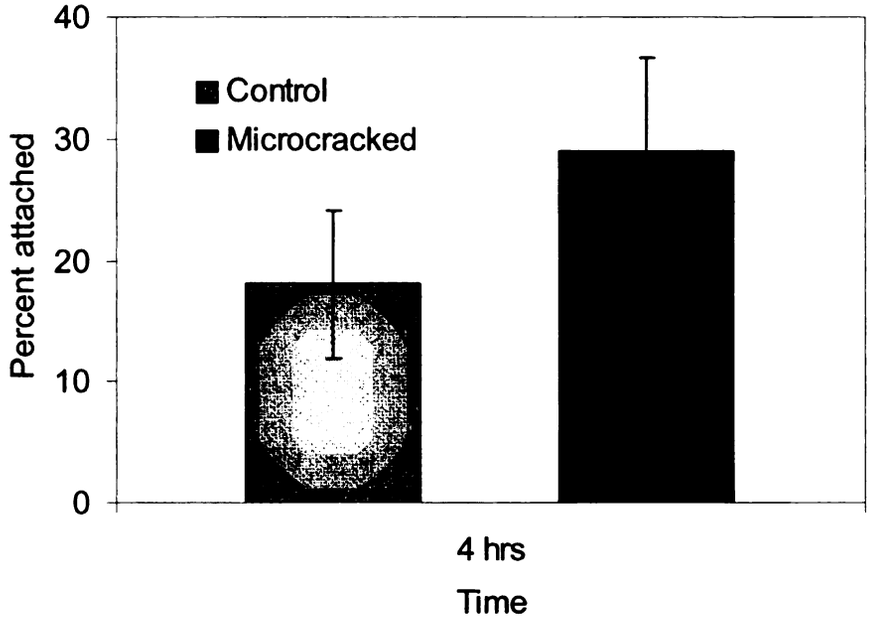

Figure 2: Osteoblast attachment at 4 hours on microcracked and non microcracked dense HA discs

The role of the Vickers indentations in increased OB attachment on HA specimens should be addressed. If we consider each indentation impression

as a surface breaking pore of an average size 2a = 54.7 μm ± 3.6 μm, then we can compare this size to that of typical pores designed to promote OB ingrowth. OBs respond to a bimodal system of pores, with pore sizes of 200 – 400 μm for macropores and < 70 μm for interconnecting micropores[35-37]. Since the Vickers indentation impressions do not approach this scale and do not include any interconnections, it is unlikely that they are the governing factor in increasing OB attachment.

Figure 3 includes optical micrographs showing OB attached to the surface of a control HA specimen (Fig. 3A) and OB attachment on a microcracked HA specimen (Fig. 3B). In addition to Hoechst stain to illuminate the cell nucleus, Rhodamine-Phalloidin stain was used to illuminate the actin fibers within the OBs The OBs attached to the surface of control HA have spread morphology (Fig. 3A), indicated by the either spindle-shaped or polygonal appearance of each cell. This spread morphology is consistent with the morphology of MC3T3-E1 OBs reported by Sudo et al. and others[28-31], and infers strong adhesion of the OBs to the HA substrate[38]. The presence of some spindle-shaped OBs and some polygonal OBs is consistent with observations of OB attachment on HA substrates at 4 hours by McMullen[39]. Figure 3B also shows the spread spindle-shaped morphology of the OBs on the surface of microcracked HA, indicating that the induction of microcracks on HA specimens does not change the shape of the attached OBs.

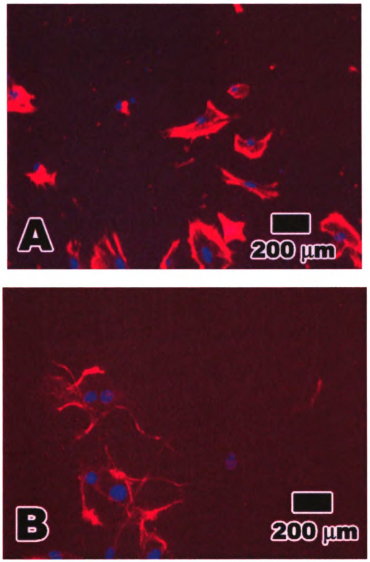

Figure 3: 3A shows MC3T3-E1 osteoblasts with both spindle-shaped and polygonal morphology on HA control specimen, stained to highlight actin fibers (red – Rhodamine-Phalloidin) and nuclei (blue – Hoechst). 3B shows MC3T3-E1 Osteoblasts with spindle shaped morphology on HA microcracked specimen, stained to highlight actin fibers (red – Rhodamine-Phalloidin) and nuclei (blue – Hoechst).

CONCLUSION

Microcracked HA specimens showed 60% greater OB attachment *in* vitro compared to non-microcracked control HA specimens (Figure 2). To capture early attachment events, future studies to assess OB attachment at earlier times will be done. Additional studies are also needed to determine whether the

induction of microcracks positively affects OB proliferation, differentiation and mineralization over time *in vitro*. However, the initial findings presented in this study indicate that microcracks enhance OB attachment activity. By mimicking the naturally occurring damage process that triggers bone remodeling, microcracks induced by Vickers indentation positively and significantly influenced the initial OB response to HA scaffolds.

REFERENCES

1. Johnson, K. A., Skinner, G. A. and Muir, P., 2001. Site-specific adaptive remodeling of Greyhound metacarpal cortical bone subjected to asymmetrical cyclic loading. Am J Vet Res, 62: 787-793.

2. Burr, D. B., Martin, R. B., Schaffler, M. B. and Radin, E. L., 1985. Bone remodeling in response to in vivo fatigue microdamage. J Biomech, 18: 189-200.

3. Burr, D. B. and Martin, R. B., 1993. Calculating the probability that microcracks initiate resorption spaces. J Biomech, 26: 613-616.

4. Mori, S. and Burr, D. B., 1993. Increased intracortical remodeling following fatigue microdamage. Bone, 14: 103-109.

5. Case, E. D., Smith, I. O. and Baumann, M. J., 2005. Microcracking and porosity in calcium phosphates and the implications for bone tissue engineering. Mat Sci and Eng A, 390: 246-254.

6. Hoepfner, T. P. and Case, E. D., 2004. An estimate of the critical grain size for microcracks induced hydroxyapatite by thermal expansion anisotropy. Mater Lett, 58: 489-492.

7. Frost, H. L., 1960. Presence of microscopic cracks in vivo in bone. Henry Ford Hospital Med Bull, 8: 27-35.

8. Blickenstaff, L. D. and Morris, J. M., 1966. Fatigue fracture of the femoral neck. J Bone Joint Surg, 48A: 1031-1047.

9. Schaffler, M. B., Choi, K. and Milgrom, C., 1995. Aging and matrix microdamage accumulation in human compact bone. Bone, 17: 521-525.

10. Lee, T. C., O'Brien, F. J. and Taylor, D., 2000. The nature of fatigue damage in bone. Int J Fatigue, 22: 847-853.

11. Zioupos, P. and Currey, J. D., 1994. The extent of microcracking and the morphology of microcracks in damaged bone. J Mat Sci, 29: 978-986.

12. Muir, P., Johnson, K. A. and Ruaux-Mason, C. P., 1999. In vivo matrix microdamage in a naturally occurring canine fatigue fracture. Bone, 25: 571-576.

13. Stepnik, M. W., Radtke, C. L., Scollay, M. C., Oshel, P. E., Albrecht, R. M., Santschi, E. M., Markel, M. D. and Muir, P., 2004. Scanning electron microscopic examination of third metacarpal/third metatarsal bone failure

surfaces in thoroughbred racehorses with condylar fracture. Vet Surg, 33: 2-10.

14. Da Costa Gomez, T. M., Radtke, C. L., Kalscheur, V. L., Swain, C. A., Scollay, M. C., Edwards, R. B., Santschi, E. M., Markel, M. D. and Muir, P., 2004. Effect of focused and radial extracorporeal shock wave therapy on equine bone microdamage. Vet Surg, 33: 49-55.

15. Lanyon, L. E., Hampson, W. G. J., Goodship, A. E. and Shah, J. S., 1975. Bone deformation recorded in vivo from strain gauges attached to the human tibial shaft. Acta Orthop Scand, 46: 256-268.

16. Burr, D. B., Milgrom, C., Fyhrie, D. P., Forwood, M., Nyska, M., Finestone, A., Hoshaw, S., Saiag, E. and Simkin, A., 1996. In vivo measurement of human tibial strains during vigorous activity. Bone, 18: 405-410.

17. Park, J. B. and Lakes, R. S., 1992. Biomaterials: An Introduction. 2nd, Plenum Press, New York.

18. Schaffler, M. B., Radin, E. L. and Burr, D. B., 1989. Mechanical and morphological effects of strain rate on fatigue of compact bone. Bone, 10: 207-214.

19. Schaffler, M. B., Radin, E. L. and Burr, D. B., 1990. Long-term fatigue behavior of compact bone at low strain magnitude and rate. Bone, 11: 321-326.

20. Burr, D. B., 2002. Targeted and nontargeted remodeling. Bone, 30: 2-4.

21. Bentolila, V., Boyce, T. M., Fyhrie, D. P., Drumb, R., Skerry, T. M. and Schaffler, M. B., 1998. Intracortical remodeling in adult rat long bones after fatigue loading. Bone, 23: 275-281.

22. Bronckers, A. L. J. J., Goei, W., Luo, G., Karsenty, G., D'Souza, R. N., Lyaruu, D. M. and Burger, E. H., 1996. DNA fragmentation during bone formation in neonatal rodents assessed by transferase-mediated end labelling. J Bone Miner Res, 11: 1281-1291.

23. Colopy, S. A., Benz-Dean, J., Barrett, J. G., Sample, S. J., Lu, Y., Danova, N. A., Kalscheur, V. L., Vanderby Jr., R., Markel, M. D. and Muir, P., 2004. Response of osteocyte syncytium adjacent to and distant from linear microcracks during adaptation to cyclic fatigue loading. Bone, 35: 881-891.

24. Noble, B. S., Peet, N., Stevens, H. Y., Brabbs, A., Mosely, J. R., Reilly, G. C., Reeve, J., Skerry, T. M. and Lanyon, L. E., 2002. Mechanical loading:

biphasic osteocyte survival and targeting of osteoclasts for bone destruction in rat cortical bone. Am J Physiol Cell Physiol, 284: 934-943.

25. Verborgt, O., Gibson, G. J. and Schaffler, M. B., 2000. Loss of osteocyte integrity in association with microdamage and bone remodeling after fatigue in vivo. J Bone Miner Res, 15: 60-67.

26. Wachtman, J. B., 1996. Mechanical Properties of Ceramics. 1, John Wiley and Sons, Inc., New York.

27. Suchanek, W., Yashima, M., Kakihana, M. and Yoshimura, M., 1996. Processing and mechanical properties of hydroxyapatite reinforced with hydroxyapatite whiskers. Biomaterials, 17: 1715-1723.

28. Du, C., Su, X. W., Cui, F. Z. and Zhu, X. D., 1998. Morphological behaviour of osteoblasts on diamond-like carbon coating and amorphous C-N film in organ culture. Biomaterials, 19: 651-658.

29. Puleo, D. A., Holleran, L. A., Doremus, R. H. and Bizios, R., 1991. Osteoblast response to orthopedic implant materials in vitro. J Biomed Mater Res, 25: 711-723.

30. Itakura, Y., Kosugi, A., Sudo, H., Yamamoto, S. and Kumegawa, M., 1988. Development of a new system for evaluating the biocompatibility of implant materials using an osteogenic cell line (MC3T3-E1). J Biomed Mater Res, 22: 613-622.

31. Sudo, H., Kodama, H. A., Amagai, Y., Yamamoto, S. and Kasai, S., 1983. In vitro differentiation and calcification in a new clonal osteogenic cell line derived from newborn mouse calvaria. J Cell Biol, 96: 191-198.

32. McMullen, R., 2004. An in vitro investigation of MC3T3-E1 osteoblast proliferation and differentiation on hydroxyapatite based tissue engineered scaffolds. Masters Degree Thesis, Michigan State University, page 43.

33. Shu, R., McMullen, R., Baumann, M. J. and McCabe, L. R., 2003. Hydroxyapatite accelerates differentiation and suppresses growth of MC3T3-E1 osteoblasts. J Biomed Mater Res, 67A: 1196-1204.

34. Case, E. D. and Kim, W. S., 1995. Comparison of thermal fatigue damage in unreinforced and reinforced alumina ceramics: crack lengths and macroscopic properties. 11th Annual Advanced Composites Conference, The Engineering Society, Ann Arbor, MI.

35. Flautre, B., Descamps, M., Delecourt, C. and Blary, M. C., 2001. Porous HA ceramic for bone replacement: role of the pores and interconnections - experimental study in rabbit. J Mat Sci: Mat Med, 12: 679-682.

36. Lu, J., Flautre, B., Anselme, K., Hardouin, P., Gallur, A., Descamps, M. and Thierry, B., 1999. Role of interconnections in porous bioceramics on bone recolonization in vitro and in vivo. J Mater Sci: Mater Med, 10: 111-120.

37. Yuan, H., Kurashina, K., deBruijn, J. D., Li, Y., deGroot, K. and Zhang, X., 1999. A preliminary study on osteoinduction of two kinds of calcium phosphate ceramics. Biomaterials, 20: 1799-1806

38. Locci, P., Becchetti, E., Pugliese, M., Rossi, L., Belcastro, S., Calvitti, M., Pietrarelli, G. and Staffolani, N., 1997. Phenotype expression of human bone cells cultured on implant substrates. Cell Biochem Funct, 15: 163-170.

39. McMullen, R., 2004. An in vitro investigation of MC3T3-E1 osteoblast proliferation and differentiation on hydroxyapatite based tissue engineered scaffolds. Masters Degree Thesis, Michigan State University, page 119.

CHAPTER 7

Early Stage MC3T3-E1 osteoblast attachment on microcracked hydroxyapatite scaffolds for tissue engineering

IAN O. SMITH, MELISSA J. BAUMANN, ELDON D. CASE
Department of Chemical Engineering and Materials Science, The College of Engineering, Michigan State University, East Lansing, MI 48824

SUBMITTED TO: J Biomed Mater Res, Dec 2006.

ABSTRACT

The effect of Vickers indentor-induced microcracking on osteoblast (OB) attachment on dense hydroxyapatite (HA) scaffolds for tissue engineering was assessed at four hours by the current authors.[1] This study extends our earlier work to early stage (one hour) OB attachment on such scaffolds. A population of > 3500 microcracks was induced across nine dense HA discs and omitted in nine control HA discs. MC3T3-E1 murine OBs were seeded onto these HA specimens and the OB attachment was then quantified and OB morphology assessed at one hour using fluorescent staining and fluorescent optical microscopy. The results were compared to our earlier four-hour OB attachment data.[1] Early stage (one-hour) OB attachment on HA was not significantly affected by the presence of microcracks, which resulted in attachment of 31.3% ± 12.7% versus 25.1% ± 8.9% on control HA surfaces. This is in contrast to the 61.1% increase at 4 hours increasing from 18% ± 6.1% to 29% ± 7.6% for microcracked versus control, shown in our earlier work.[1] Therefore, while microcracking does have a statistically meaningful

effect at four hours attachment time, there is no significant effect on the early stage (1 hour) OB attachment on HA.

INTRODUCTION

The work presented in this paper differs from our earlier work[1], where osteoblast (OB) attachment was assessed at four hours, because we are now observing early stage (one hour) OB attachment. A triplicate model was utilized with three microcracked HA specimens and three non-microcracked control HA specimens in each trial, for a total of nine microcracked and nine control specimens. MC3T3-E1 murine OBs were seeded onto these HA specimens and the subsequently attached OBs were then counted at one hour and their morphology assessed using fluorescent staining and fluorescent optical microscopy. The results were compared to those previously collected at four hours[1] in order to first assess the effect of microcracking in the early phase of OB attachment and then to evaluate the overall potential of microcracking on OB activity.

Bone microdamage occurs in the form of microcracks in humans[2-4], thoroughbred racing horses[5,6] and greyhounds[7,8] following repetitive physical activity. For example, while the strain levels in human bone during walking reach $\varepsilon = 3 \times 10^{-4}$ to 8×10^{-4}, and during running reach $\varepsilon = 8 \times 10^{-4}$ to 1.2×10^{-3}, this is less than the threshold failure strain in a single cycle. However, the repetitive nature of these activities leads to an accumulation of microdamage.[9,10] Unless such activity ceases or declines dramatically, this

microdamage can coalesce into macrocracks, leading to catastrophic fracture.[2,11,12] The connection between bone microcracks and repetitive physical activity was first postulated by Frost in 1960, who used Fuchsin staining to detect their presence.[13] More recently, microcracks have been identified in bone using increasingly sophisticated techniques including optical and confocal laser scanning microscopy (CLSM) using Fuchsin[3,4,8,6] haematoxylin and eosin[7] and fluorescent staining[4,14], scanning electron microscopy (SEM)[5] and radiography[2].

In most cases, if the physical activity that causes the damage is reduced, catastrophic failure is prevented because bone has the ability to dynamically remodel following the onset of microdamage. Osteoclasts (OCs) are specialized bone cells, which resorb bone while OBs generate new bone in the vicinity of the microcracks.[15] OC and OB activities are increased when the syncytium, adjacent to areas of bone microdamage, signals for remodeling to begin through increased osteocyte apoptosis. This coupling between remodeling and microcracking may paradoxically result in a lower incidence of initial catastrophic fracture because of the ability of the microcracks to dissipate energy through crack formation, which in turn signals bone healing.

While the links between microcracking, osteocyte damage, apoptosis and subsequent *in vivo* bone remodeling in bone are known[16-20], the relationships between the degree of microcrack damage in hydroxyapatite (HA) and OB attachment is not yet fully understood. HA is a calcium

phosphate-based ceramic with a crystal structure and composition close to that of the mineral component of bone which which leads to HA's use as a bone replacement scaffold material.[21,22] We have previously shown that OB attachment at 4 hours increased significantly in microcracked dense HA samples compared to dense HA control specimens.[1] It is noteworthy that this increase occurred in the absence of the osteocyte syncytium instrumental to the *in vivo* bone remodeling process. These results indicate that osteocyte signaling is likely not the sole mechanism for initiating bone remodeling. Therefore microcracked HA scaffolds may offer promise as a synthetic bone scaffold material for enhanced bone tissue repair.

In our earlier study, microcracks were created by placing 196 Vickers indentations in the HA specimens. The indentations were arranged in a 14x14 grid with the indentation centers located 1 mm apart.[1] Each indentation produced two perpendicular microcracks for 392 microcracks per specimen on a total of nine specimens.

Vickers indentation is a method used to assess hardness in brittle materials. Vickers indentation uses a square-based pyramidal diamond indenter tip, which, upon loading, leaves a diamond-shaped impression with radial microcracks extending into the material from the corners of that impression. Figure 1 is a SEM micrograph of a single Vickers indentation on a HA surface, showing the induced radial cracks (labeled as "R"). The microcrack length (2c) and indent width (2a) are indicated on this micrograph using white arrows.

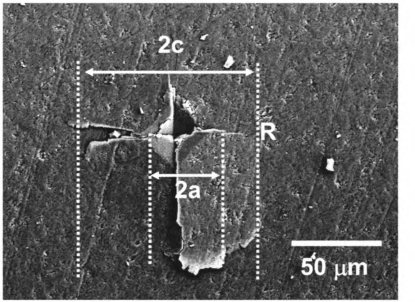

Figure 1: SEM micrograph of microindentation on HA specimen surface. "R" indicates radial cracks, the distance "2a" indicates the diagonal length of the indentation impression and the distance "2c" indicates crack length.

The grid of Vickers indentations created a uniform microcrack density across the HA scaffold surface. In contrast, thermal expansion anisotropy (TEA) induced microcracks, such as those identified in our earlier work, are more difficult to control.[23] TEA-induced microcracks form during cooling in non-cubic crystalline materials when the average grain size is above a critical value ($G > G_{CR}$). This value is difficult however to estimate for HA because of variations in reported values of the thermal expansion coefficient, α.[24] While we were the first to definitively identify microcracking without an externally applied stress in dense HA[23], it was not until our more recent work that we were able to control the size and number of these microcracks.[1]

MATERIALS AND METHODS

HA disc specimens were fabricated using medical-grade purity HA powder with a manufacturer-reported particle diameter of 1 – 3 μm (Taihei Chemical, Osaka, Japan), which was die-pressed into 32 mm disc-shaped green compacts. These green specimens were sintered in air at 1360°C for 4 hours, at a heating/cooling rate of ~10°C/min. Specimens were then subjected to further heat treatment, not related to the current study, at 1100°C for 45 minutes at a heating/cooling rate of ~10°C/min.[2] Using this process, we fabricated specimens of > 99% theoretical density (determined by Archimedes method) that are ~23 mm in diameter and 1 – 2 mm thick, with an average grain diameter of 4 μm ± 1 μm. A total of 18 specimens were used in this study, nine microcracked and nine controls.

Immediately prior to their use, these HA discs were ultrasonically cleaned, ground using 600 grit (30 μm) silicon carbide abrasive paper and sequentially polished using 30 μm, 12 μm, 9 μm, 6 μm and 1 μm diamond abrasive suspensions for 5 minutes each. Grinding and polishing was completed using a Buehler EcoMet 3 polishing wheel with an AutoMet 2 polishing head (Buehler, Lake Bluff, IL). Following the final polishing step, specimens were cleaned by pulsing with an ultrasonic probe while submerged in reverse osmosis distilled (RO) H_2O.

---

* This second heat treatment was necessary to induce grain-boundary grooving vital to an earlier, yet unpublished study. This grooving was eliminated during the grinding process, prior to OB seeding in the current study.

Microcracks were induced, following methods established in our previous study[1], across the surface of half of the specimens using a Buehler MicroMet II Vickers indentor. The placement of Vickers indentations using this established load magnitude, loading time and loading speed resulted in cracks with the least amount of spalling and chipping, which are counterproductive to microcrack formation. The indentations were arrayed in a 14x14 grid, 1 mm apart, with two perpendicular radial microcracks emerging from each indentation pyramid for a total of 392 cracks/specimen and > 3500 cracks total across all nine specimens. Following indentation, each HA disc was submerged in RO distilled H_2O for eight hours in order to facilitate crack growth saturation prior to cell seeding.[1]

For this study, MC3T3-E1 clonal murine OBs of subclone 14 (American Type Culture Collection, Manassas, VA) were thawed from frozen stock (-180°C) and plated onto polystyrene tissue culture dishes. OB cultures were fed using complete media; a combination of 90% α-minimum essential media (α-MEM, Invitrogen, Grand Island, NY) and 10% fetal bovine serum (FBS, Atlanta Biologicals, Lawrenceville, GA). OB cultures were then placed into an incubator at 37°C and 5% CO_2 in a humid atmosphere and split every two days. OBs were split until a sufficient cell number was reached for this study (passages 28-29) first by trypsinizing the OBs (trypsin/EDTA, Invitrogen, Grand Island, NY) and then dividing them to be replated at a lower OB density, to allow room for the OBs to divide.

The control (nine discs) and microcracked (nine discs) HA specimens were autoclave sterilized at 125°C for one hour prior to OB seeding. The OBs were seeded onto sterile HA substrates at a cell density of 11,320/cm^2 and 1 ml complete media added to each well.[25] Prior to seeding, each HA substrate was surrounded by a commercially pure Al foil collar to control cell density by preventing the OBs from falling off the specimen surface. These seeded specimens were then incubated at 37°C and 5% CO_2 in a humid atmosphere for one hour.

After incubation, the OB-seeded HA discs were removed from the incubator and rinsed twice with 1x phosphate buffered saline (PBS) to remove any non-attached cells. The attached OBs were then fixed and stained using Rhodamine-Phalloidin, which acts to illuminate the cell cytoskeleton, and Hoechst, which allows the cell nucleus to be imaged.[26]

Attached OBs were imaged using an optical fluorescence microscope (Leica DM IL, Leica Microsystems, Wetzlar, GER) and a Spot RT camera (Diagnostic instruments, Inc, Sterling Heights, MI). Rhodamine-Phalloidin fluoresces at λ = 565 nm and specifically stains the actin fibers within the OB cytoskeleton. This provides a clear image of the morphology of each OB. Hoechst stains the cell nuclei and fluoresces at λ = 465 nm, providing an image of each OB nucleus. Ten randomly selected fields of view were imaged per specimen surface and the number of OB nuclei counted in each. Statistical significance in cell counts was determined using Student's t-test, with $p < 0.05$ taken to indicate a significant difference. The effect of

microcracking on OB morphology was assessed after staining for actin fibers by observing the shape of the cytoskeleton, imaged using optical fluorescence.

RESULTS AND DISCUSSION

Vickers indentations were produced as described earlier and the indentation diagonal lengths measured.[1] The indenter-induced impressions on the surface of dense HA had an average diagonal length of $2a_{AVE}$ = 47.3 μm ± 4.6 μm and yielded an average post-saturation crack length of $2c_{AVE}$ = 124.4 μm ± 21.1 μm.

Figure 2a is a plot of OB attachment at one hour for both control HA (n = 9) and microcracked HA (n = 9) specimens. For comparative purposes, Figure 2b includes four-hour time point attachment data reported in our earlier study.[1] Error bars represent the standard deviation and "#" indicates a statistically significant difference.

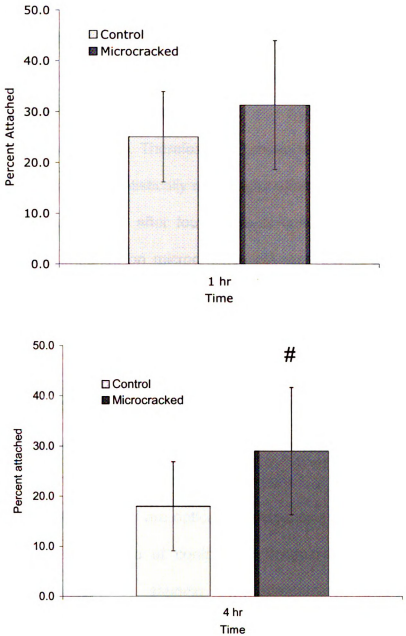

Figure 2: A) MC3T3-E1 OB attachment at 1 hour on control and microcracked HA specimens. B) MC3T3-E1 OB attachment at 4 hours on control and microcracked HA specimens. 4-hour attachment data was taken with permission from previous work by Smith et al.[1] # indicates that difference in OB attachment between control HA and microcracked HA at 4 hours is significant ($p = 0.004$).

OB attachment at one hour was 25.1% ± 8.9% of OBs plated on the control HA and 31.3% ± 12.7% of OBs plated on the microcracked HA. Student's t-test gave a p-value of 0.25, meaning that there was no significant difference between the OB attachment on microcracked and non-microcracked HA specimens. Therefore the presence of microcracks on HA surfaces does not have a statistically meaningful effect on early stage 1-hour OB attachment. In contrast, after four hours of culture, the percentage of plated OBs which attached on microcracked HA was 61.1% greater, when compared to non-microcracked HA, increasing from 18% ± 6.1% to 29% ± 7.6% of OBs plated.[1] Student's t-test showed that this increase in the percentage of OB attachment was significant ($p = 0.004$). Since data for each time point is taken from a different study, using a different batch of the same MC3T3-E1 OB subclone, a direct quantitative comparison between the one and four-hour attachment data cannot be made here.

The images in Figure 3 are optical fluorescence micrographs showing OBs attached to the surface of control and microcracked HA scaffolds. Images were enhanced by staining with Rhodamine-Phalloidin, which illuminated the actin fibers within the OB cytoskeleton, and Hoechst stain to highlight the OB nuclei. Figure 3A is a photomicrograph of the control HA surface, showing six attached OBs. These cells exhibit either spread or polygonal morphology, which is consistent with the MC3T3-E1 OB morphology reported by Sudo et al.[27,28] For OBs, both the spread and polygonal morphology is indicative of strong adhesion to the underlying

substrate.[29] Figure 3B is a photomicrograph of the microcracked HA surface having seven attached OBs, all of which also exhibit either spread or polygonal morphology, indicating that microcracks do not change the attached OB morphology. This OB morphology is consistent with that in our earlier findings, showing both the spread and polygonal OB morphology was present at four hours attachment time, indicating that microcracks do not change OB morphology at four hours attachment time either.[1]

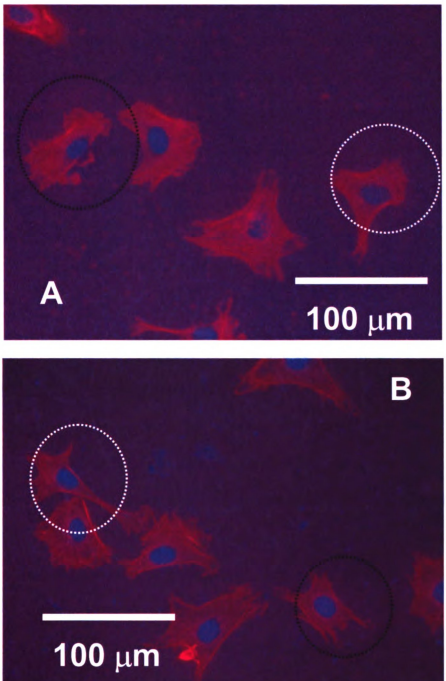

Figure 3: A) MC3T3-E1 OBs with spread (white circle) and polygonal (black circle) morphology on HA control specimen. B) MC3T3-E1 OBs with similar spread (white circle) and polygonal (black circle) morphology on microcracked HA specimen. OBs have been stained to highlight actin fibers (red – Rhodamine-Phalloidin) and cell nuclei (blue – Hoechst).

CONCLUSIONS

We have assessed the effect of induced microcracking on early, 1-hour OB. Microcracks were induced on the surface of nine HA discs by indenting each disc 196 times using a Vickers microindenter. This resulted in 392 radial cracks per specimen on nine specimens for a total of 3528 induced microcracks. This large population of microcracks is in contrast to the nine non-indented, non-microcracked control HA disc surfaces. While the grain diameter of the specimens used in this study (4 $\mu m \pm 1$ μm) is larger than G_{CR} for TEA-induced microcracking as estimated for HA (1.1 μm)[24], surface breaking microcracks were not observed in these specimens under SEM.

MC3T3-E1 OB attachment data shows that this large population of microcracks does not significantly increase OB attachment at one-hour attachment times in comparison to non-microcracked samples. This result is in contrast to the 61.1% improvement in mean OB attachment at four hours reported previously.[1]

Additionally, the presence of microcracks did not affect OB morphology on the HA surface. Both microcracked and control HA surfaces led to either spread or polygonal attached osteoblasts, pointing to strong attachment to the underlying substrate.[29] This finding is in agreement with our four-hour attachment data, which found a no significant link between microcracking and resulting OB morphology.

While enhanced OB attachment at a time of four hours may preview improved cell differentiation and production of mineral matrix by mimicking the

naturally occurring damage mechanism that brings about bone repair, one hour is too early for this phenomenon to be observed.

Our future work will focus on assessing the effect of induced microcracking on OB growth and differentiation.

REFERENCES

1. Smith IO, Baumann MJ, Case ED. Induced microcracking affects osteoblast attachment on hydroxyapatite scaffolds for tissue engineering. Am J Biochem Biotechnol 2006; 2: 105-110.

2. Blickenstaff LD, Morris JM. Fatigue fracture of the femoral neck. J Bone Joint Surg 1966; 48A: 1031-1047.

3. Schaffler MB, Choi K, Milgrom C. Aging and matrix microdamage accumulation in human compact bone. Bone 1995; 17: 521-525.

4. Lee TC, O'Brien FJ, Taylor D. The nature of fatigue damage in bone. Int J Fatigue 2000; 22: 847-853.

5. Stepnik MW, Radtke CL, Scollay MC, Oshel PE, Albrecht RM, Santschi EM, Markel MD, Muir P. Scanning electron microscopic examination of third metacarpal/third metatarsal bone failure surfaces in thoroughbred racehorses with condylar fracture. Vet Surg 2004; 33: 2-10.

6. Da Costa Gomez TM, Radtke CL, Kalscheur VL, Swain CA, Scollay MC, Edwards RB, Santschi EM, Markel MD, Muir P. Effect of focused and radial extracorporeal shock wave therapy on equine bone microdamage. Vet Surg 2004; 33: 49-55.

7. Johnson KA, Skinner GA, Muir P. Site-specific adaptive remodeling of Greyhound metacarpal cortical bone subjected to asymmetrical cyclic loading. Am J Vet Res 2001; 62: 787-793.

8. Muir P, Johnson KA, Ruaux-Mason CP. In vivo matrix microdamage in a naturally occurring canine fatigue fracture. Bone 1999; 25: 571-576.

9. Lanyon LE, Hampson WGJ, Goodship AE, Shah JS. Bone deformation recorded in vivo from strain gauges attached to the human tibial shaft. Acta Orthop Scand 1975; 46: 256-268.

10. Burr DB, Milgrom C, Fyhrie DP, Forwood M, Nyska M, Finestone A, Hoshaw S, Saiag E, Simkin A. In vivo measurement of human tibial strains during vigorous activity. Bone 1996; 18: 405-410.

11. Schaffler MB, Radin EL, Burr DB. Mechanical and morphological effects of strain rate on fatigue of compact bone. Bone 1989; 10: 207-214.

12. Schaffler MB, Radin EL, Burr DB. Long-term fatigue behavior of compact bone at low strain magnitude and rate. Bone 1990; 11: 321-326.

13. Frost HL. Presence of microscopic cracks in vivo in bone. Henry Ford Hospital Med Bull 1960; 8: 27-35.

14. Zioupos P, Currey JD. The extent of microcracking and the morphology of microcracks in damaged bone. J Mat Sci 1994; 29: 978-986.

15. Burr DB. Targeted and nontargeted remodeling. Bone 2002; 30: 2-4.

16. Burr DB, Martin RB, Schaffler MB, Radin EL. Bone remodeling in response to in vivo fatigue microdamage. J Biomech 1985; 18: 189-200.

17. Bronckers ALJJ, Goei W, Luo G, Karsenty G, D'Souza RN, Lyaruu DM, Burger EH. DNA fragmentation during bone formation in neonatal rodents assessed by transferase-mediated end labelling. J Bone Miner Res 1996; 11: 1281-1291.

18. Colopy SA, Benz-Dean J, Barrett JG, Sample SJ, Lu Y, Danova NA, Kalscheur VL, Vanderby Jr. R, Markel MD, Muir P. Response of osteocyte syncytium adjacent to and distant from linear microcracks during adaptation to cyclic fatigue loading. Bone 2004; 35: 881-891.

19. Noble BS, Peet N, Stevens HY, Brabbs A, Mosely JR, Reilly GC, Reeve J, Skerry TM, Lanyon LE. Mechanical loading: biphasic osteocyte survival and targeting of osteoclasts for bone destruction in rat cortical bone. Am J Physiol Cell Physiol 2002; 284: 934-943.

20. Verborgt O, Gibson GJ, Schaffler MB. Loss of osteocyte integrity in association with microdamage and bone remodeling after fatigue in vivo. J Bone Miner Res 2000; 15: 60-67.

21. Hench LL. Bioceramics: From Concept to Clinic. J Am Ceram Soc 1991; 74: 1487-1510.

22. DeGroot K. Effect of porosity and physicochemical properties on the stability, resorption, and strength of calcium phosphate ceramics. In: Bioceramics: Material characteristics versus *in vivo* behavior, Vol. 523. Ed. Duscheyne , lemons J. Annals of the New York Academy of Sciences, New York, 1988.

23. Case ED, Smith IO, Baumann MJ. Microcracking and porosity in calcium phosphates and the implications for bone tissue engineering. Mat Sci and Eng A 2005; 390: 246-254.

24. Hoepfner TP, Case ED. An estimate of the critical grain size for microcracks induced hydroxyapatite by thermal expansion anisotropy. Mater Lett 2004; 58: 489-492.

25. Shu R, McMullen R, Baumann MJ, McCabe LR. Hydroxyapatite accelerates differentiation and suppresses growth of MC3T3-E1 osteoblasts. J Biomed Mater Res 2003; 67A: 1196-1204.

26. McMullen R. An in vitro investigation of MC3T3-E1 osteoblast proliferation and differentiation on hydroxyapatite based tissue engineered scaffolds. Masters Degree Thesis, Michigan State University 2004: p. 86.

27. Sudo H, Kodama HA, Amagai Y, Yamamoto S, Kasai S. In vitro differentiation and calcification in a new clonal osteogenic cell line derived from newborn mouse calvaria. J Cell Biol 1983; 96: 191-198.

28. Itakura Y, Kosugi A, Sudo H, Yamamoto S, Kumegawa M. Development of a new system for evaluating the biocompatibility of implant materials using an osteogenic cell line (MC3T3-E1). J Biomed Mater Res 1988; 22: 613-622.

29. Locci P, Becchetti E, Pugliese M, Rossi L, Belcastro S, Calvitti M, Pietrarelli G, Staffolani N. Phenotype expression of human bone cells cultured on implant substrates. Cell Biochem Funct 1997; 15: 163-170.

CHAPTER 8

THE EFFECT OF GRAIN BOUNDARY GROOVING ON MC3T3-E1 OSTEOBLAST ATTACHMENT ON DENSE HYDROXYAPATITE

INTRODUCTION

Grain boundary grooving is an artifact of thermal etching, a phenomenon that occurs in polycrystalline materials that have been heated to elevated temperatures ($T \sim 1/2 - 2/3T_M$). Thermal etching is the result of the system moving towards equilibrium, where the grain boundary and surface energy are related as shown below in Equation 1

$$\gamma_{SS} = 2\gamma_{SV}\cos(\psi/2) \quad (1)$$

where γ_{SS} = the energy of the solid-solid interface between grains, γ_{SV} = the solid-vapor interfacial energy and ψ = the angle of thermal etching.[1]

While the surface roughness associated with nano-scale ceramic substrates has been associated with improved osteoblast (OB) attachment[2-4], the contribution of grain boundaries to this relationship is not fully understood. We investigated the relationship between grain boundaries and OB attachment, by determining whether the presence of grain boundary grooves, independent of a change in grain size, significantly affects OB attachment and morphology on dense hydroxyapatite (HA) substrates.

MATERIALS AND METHODS

Specimen Fabrication

We used medical grade hydroxyapatite (HA) powder (Taihei Chemical, Osaka, JP) with a manufacturer's reported mean particle diameter of 1 - 3 μm to fabricate dense HA discs. Eighteen specimens were fabricated using a binderless powder pressing technique developed earlier.[5] For each HA disc, powder was poured into a 32 mm diameter KBr pellet die (International Crystal Laboratiries, Garfield, NJ) and uniaxially pressed at 35 MPa for one minute, yielding a green powder compact 2 – 3 mm in thickness. As-pressed discs were then sintered in air at 1360°C (1633 K) for 4 hours, at a heating/cooling rate of ~10°C per minute. Sintered specimen density was determined to be > 99%, determined by Archimedes method and the average grain diameter was determined to be 4 μm ± 1 μm using the line-intercept method. X-ray diffraction verified that the sintered specimens were in fact HA (Appendix B).

Sintered specimens were wet ground using 600 grit (30 μm) SiC abrasive paper and sequentially polished using 30 μm, 12 μm, 9 μm, 6 μm and 1 μm diamond abrasive paste and/or polishing suspension for 5 minutes at each level. Grinding and polishing were done at 200 rpm using a Buehler EcoMet 3 polishing wheel equipped with an AutoMet 2 automated head

(Buehler, Lake Bluff, IL). Specimens were thoroughly rinsed with reverse osmosis (RO) water between steps and cleaned by pulsing (20 kHz, 250 Watts) with an ultrasonic probe in RO water for five minutes following the final step.

Half (9) of the polished discs were thermally etched at 1100°C (1373 K) for 45 minutes, with a heating/cooling rate of 10°/min in order to induce grain boundary grooving. All specimens were then stored in a vacuum dessicator until cell culture.

This processing protocol yielded two groups of equally dense HA discs, both with an average grain diameter of 4 μm ± 1 μm, in which one group is polished to 1 μm (control) and the other includes grain boundary grooves. Figure 1 is a scanning electron micrograph showing the surface of a grain boundary grooved specimen.

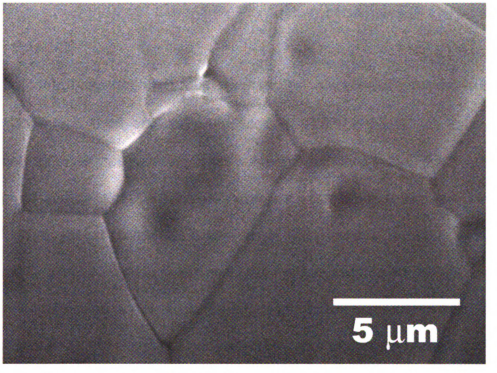

Figure 1: SEM micrograph of the surface of a grain boundary grooved HA specimen.

Cell Culture

MC3T3-E1 osteoblasts (OBs) of subclone 14 obtained from ATCC (Manassas, VA) were used for this study. OBs were thawed from frozen stock (-180°C/ 93 K) and plated onto polystyrene tissue culture dishes. α-minimum essential media (α-MEM, Invitrogen, Grand island, NY) supplemented with 10% fetal bovine serum (FBS, Atlanta Biologicals, Lawrenceville, GA) was added to the thawed OBs (complete media). OBs were then incubated at 37°C (310 K) and 5% CO_2 in a humid atmosphere and split approximately every two days. Cells were split by trypsinization (trypsin/EDTA, Invitrogen, Grand Island, NY) and re-plated onto polystyrene plates until the OB

population reached the level needed for the number of samples in this study (passages 24-26).

The control and grain boundary grooved HA discs were removed from the dessicator and then autoclave sterilized at 125°C (398 K) for 1 hour immediately prior to cell seeding. OBs were plated onto these discs at a density of 11,320 cells/cm^2, where cell confluency has been shown to occur, after which 1 ml of complete media was then added to each well.[6] Commercially pure Al collars were used during cell seeding to prevent the media from leaving the specimen surfaces, giving a constant surface area for OB attachment. OB-seeded discs were then placed into commercially pure Al collars and incubated in a humid atmosphere of 5% CO_2 at 37°C (310 K) for four hours.

Cell imaging

Following incubation, the media was removed and each OB-seeded HA specimen was rinsed twice with 1X phosphate buffered saline (PBS) to remove any non-adherent OBs. The adherent cells were then fixed using 3.7% formaldehyde (H_2CO) (JT Baker, Phillipsburg, NJ), permeabilized for 5 minutes using 0.1% Triton X-100 (Sigma-Aldrich, St. Louis, MO) and pre-incubated in 1% bovine serum albumin (BSA, Invitrogen, Grand Island, NY). The OBs were then stained using two different dyes; Rhodamine-Phalloidin was used to stain the actin fibers of the OB cytoskeleton and Hoescht was used to stain the nuclei (Invitrogen, Grand Island, NY). Rhodamine-Phalloidin

stain fluoresces at a wavelength of $\lambda_{emmision}$ = 565 nm when exposed to light of wavelength $\lambda_{excitation}$ = 542 nm, while the Hoechst stain fluoresces at a wavelength of $\lambda_{emmision}$ = 465 nm when exposed to light with wavelength of $\lambda_{excitation}$ = 355 nm. This characteristic absorption/emission behavior is suited for use with our imaging equipment.

Stained specimens were mounted in glycerol solution (JT Baker) and the cells imaged using a Leica DM IL optical fluorescence microscope (Leica Microsystems, Wetzlar, GER) equipped with a Spot RT camera (Diagnostic Instruments, Inc., Sterling Heights, MI). Twenty systematic fields of view, selected in a pattern covering the entire specimen surface, were imaged and the cell nuclei were counted and the counts tallied in each. Students t-test was used to determine the statistical significance in the cell counts, with $p < 0.05$ taken as significant.

The effect of thermal etching of HA specimens on OB morphology was assessed by imaging the actin fibers to assess the OB shape using optical fluorescence microscopy.

Following OB imaging, the HA discs were cleaned, repolished and half (9) of the discs were thermally etched once again. The entire procedure was then repeated for an attachment time of one hour.

RESULTS AND DISCUSSION

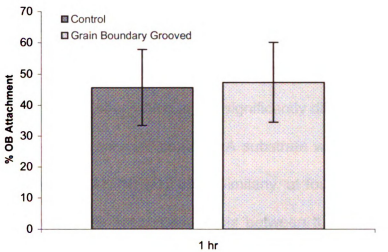

A

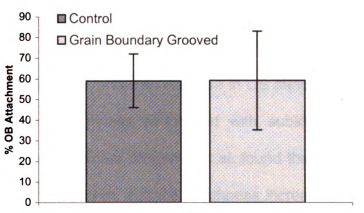

B

Figure 2: MC3T3-E1 OB attachment at 1 (Figure 2A) and 4 (Figure 2B) hours on thermally etched and control HA specimens.

Figure 2 shows the percent of MC3T3-E1 OB attachment as a fraction of the total number of OBs plated as a function of time for both control HA and

thermally etched HA discs. Since the one-hour and four-hour data sets represent separate experiments using different OB populations, the data cannot be directly compared. However, attachment data for both the control and grain boundary grooved specimens can be compared at each time point. The mean OB attachment on HA surfaces with grain-boundary grooving is 45.6% ± 12.2% at one hour which is not significantly different from the mean OB attachment on the polished control HA substrate with no grain-boundary grooving at one hour (47.3% ± 12.8%). Similarly, at four hours no significant change in the mean OB attachment exists between the HA substrates with grain boundary grooving (59.0% ± 13.0%) and the polished control HA substrates (59.3% ± 23.9%) with no grain-boundary grooving.

These results show that the presence of grain boundary grooving on dense HA substrates does not significantly affect OB attachment. Earlier studies by Webster et al. show an increase in OB attachment as a function of increased surface roughness associated with substrates processed from nano-scale ceramic powders. Webster et al. found that decreasing the grain size from 177 nm to 23 nm, surface roughness increased from 17 nm to 20 nm (Al_2O_3).[4] Our findings indicate that the grain boundary grooving does not result in as pronounced a surface roughness (R_a = 10.23 ± 1.8 nm) and are not a factor in this increased OB attachment. Rather, decreasing grain size in unpolished specimens increases surface roughness by creating a larger number of surface asperities. This phenomenon is apparent in AFM images published by Webster et al.[4]

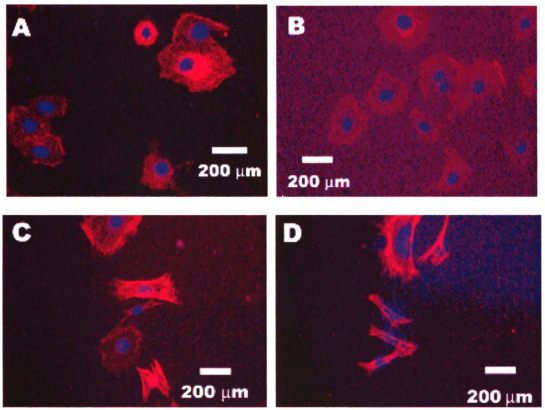

Figure 3: This set of four optical micrographs shows attached OBs at one hour on the surface of a control specimen (Figure 3A) and a grain boundary grooved specimen (Figure 3B), and also at four hours on the surface of a control specimen (Figure 3C) and a grain boundary grooved specimen (Figure 3D).

These results show that grain boundary grooving also has no effect on the morphology of attached OBs. The attached OBs shown in Figure 3A and 3B exhibit a similar morphology (average spicule length of 13.6 μm ± 10 μm for control and 10.4 μm ± 5.4 μm for grain boundary grooved), as do the OBs shown in Figure 3C and 3D (average spicule length of 24.8 μm ± 10.3 μm for control and 28.8 μm ± 9.4 μm for grain boundary grooved). The lower degree of OB spreading (Average spicule length of 12 μm ± 8 μm versus 18 μm ± 8

μm) on the one-hour as compared to the four-hour attachment photomicrographs is likely due to the earlier stage of OB attachment. At four hours attachment, OBs on the control specimen (Figure 3C) and the grain boundary grooved specimen (Figure 3D) both exhibit a spindle-shaped spread morphology. This is consistent with that of two of our earlier studies, where the microcracks on the HA substrate surface did not change the OB morphology.

While the mechanism by which microcracks form in HA is fundamentally different than that by which grain boundary grooves are formed, these surface features are of the same order of magnitude in size. By looking at the micrograph in Figure 1, the grain boundary groove width can be measured to be approximately 0.1 μm. From our earlier work[7] induced microcracks in HA are approximately 0.5 μm in width. These dimensions should be verified statistically and using a higher magnification, but from these estimates it is apparent that surface features between 0.1 and 0.5 μm in width do not have an effect on OB morphology. In these previous studies, as well as the present one, the OBs have a spread polygonal and/or spindle-shaped morphology, which is consistent with that shown for healthy OBs by Sudo et al.[8]

REFERENCES

1. Kingery WD, Bowen HK, Uhlmann DR. Introduction to Ceramics. New York: John Wiley and Sons; 1960. 1032p.

2. Webster TJ, Ergun C, Doremus RH, Siegel RW, Bizios R. Nanocrystalline hydroxyapatite enhances osteoblast function. In: Proceedings of the First Joint BMES/EMBS Conference, Atlanta, GA; 1999. p744.

3. Webster TJ, Siegel RW, Bizios R. Design and evaluation of nanophase alumina for orthopaedic/dental applications. Nanostruct Mater 1999;12:983-986.

4. Webster TJ, Siegel RW, Bizios R. Osteoblast adhesion on nanophase ceramics. Biomaterials 1999;20:1221-1227.

5. McMullen, R. An in vitro investigation of MC3T3-E1 osteoblast proliferation and differentiation on hydroxyapatite based tissue-engineered scaffolds. Masters Degree Thesis. Department of Chemical Engineering and Materials Science. Michigan State University, East Lansing, MI; 2004. 181p.

6. Shu R, McMullen R, Baumann MJ, McCabe LR. Hydroxyapatite accelerates differentiation and suppresses growth of MC3T3-E1 osteoblasts. J Biomed Mater Res. 2003;67A:1196-1204.

7. Smith, I.O., McCabe, L.R., Baumann, M.J., MC3T3-E1 Osteoblast attachment and proliferation on porous hydroxyapatite scaffolds with nanophase powder, Int J Nanomed, 1[2], 189-194 (2006).

8. Sudo H, Kodama HA, Amagai Y, Yamamoto S, Kasai S. In vitro differentiation and calcification in a new clonal osteogenic cell line derived from newborn mouse calvaria. J Cell Biol 1983; 96: 191-198.

CHAPTER 9

SUMMARY AND CONCLUSIONS

Summary of Work Completed for this Dissertation

This research quantified the effect of two phenomena associated with grain boundaries in hydroxyapatite (HA), microcracks and grain boundary grooving, on osteoblast (OB) attachment. These findings tie into the larger question of why a reduction in particle size in polycrystalline ceramics (HA in this case) leads to an increase in OB attachment *in vitro*.

While Webster et al. have studied the link between decreased grain size and improved OB behavior on *dense* scaffolds, an ideal bone tissue engineering scaffold should be a more biomimetic surface where interconnected macroporosity is of primary importance in bone tissue ingrowth. Therefore, we investigated whether grain size affects OB development in foamed porous HA scaffolds with bimodal porosity (Figure 1). Bimodal porosity encompasses both macropores and micropores that link the macropores in order to provide nutrient transmission (Figure 2), in a manner similar to that found in cancellous bone. In Chapters 3 and 4, porous scaffolds with an average porosity of 59% ± 2.2% and 72% ± 8.3% were fabricated with micron-HA powder (having an average manufacturer-reported particle diameter of 10 μm and an average sintered grain diameter of 8.6 μm ± 1.9 μm) and nano-HA powder (having an average manufacturer-reported particle diameter of 20 nm and an average sintered grain diameter of 588 nm ± 55 nm), respectively.

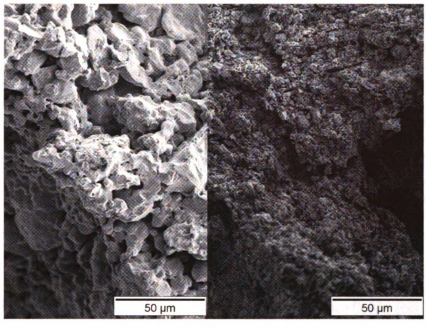

Figure 1: Comparison of SEM micrographs of the surface of bimodally porous scaffolds fabricated using micro HA (left) and nano HA (right). Scaffolds were fabricated by foaming a suspension of HA powder using H_2O_2 as a foaming agent, drying at 125°C for 1 hour and sintering either at 1360°C for 4 hours (micro HA) or 1100°C for 1 hour (nano HA). Image taken from Smith et al., Int J Nanomed 2006;1:189-194.

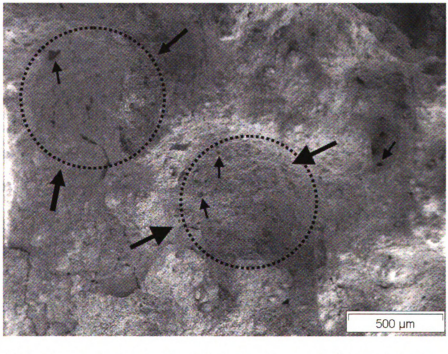

Figure 2: SEM micrograph showing the surface of porous scaffold fabricated using nano HA, including macropores (large arrows noting approximate boundary of a macropore) and micropores (small arrows emphasizing the <60 µm interconnecting pores). Image taken from Smith et al., Int J Nanomed 2006;1:189-194.

Using a hemacytometer, MC3T3-E1 murine OB attachment was quantified at 0.5, 1, 2 and 4 hours and OB proliferation (growth) was quantified at 1, 3 and 5 days. This original data is shown in Figures 3 and 4. Background counts were also taken to eliminate the contribution of OB-sized HA particles and to increase the OB count accuracy. Adjusted data from background counts is shown in Figure 5. We found that OB attachment is not significantly different between 0.5 and 4 hours and that OB proliferation was not significantly different from 1 to 5 days. This suggests that surface topography within the walls of these bimodally porous scaffolds (on the scale of the grain size) is not a significant contributor to OB attachment and proliferation and that bimodal porosity, is a greater factor in promoting OB attachment. However, high hemacytometer cell counts indicate that further inaccuracies exist in these results and a more accurate method must be employed to measure OB attachment.

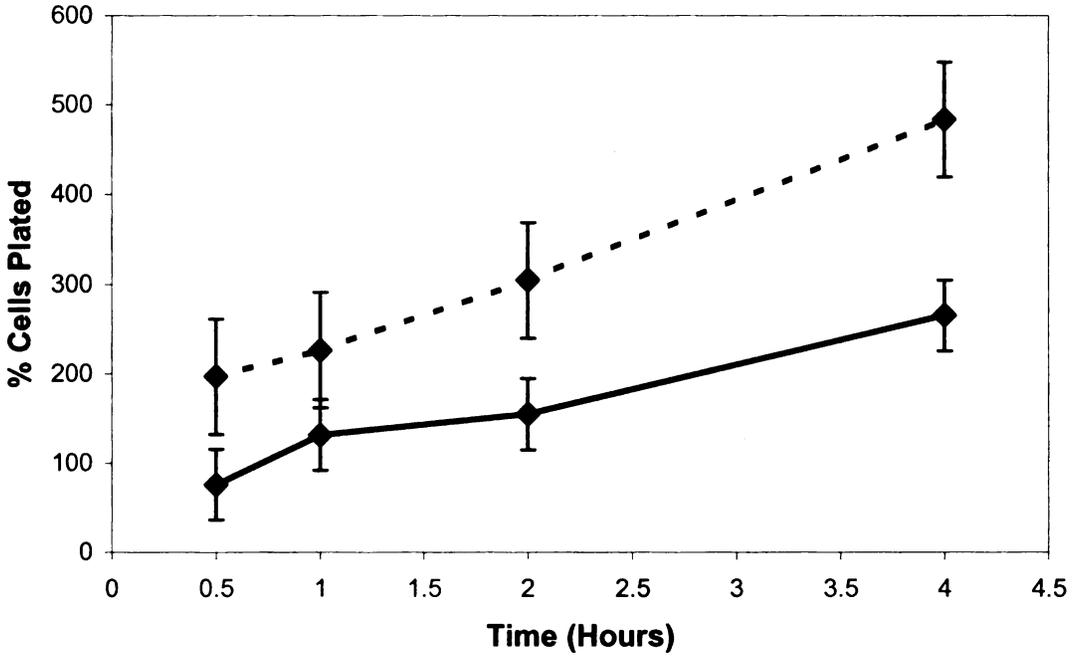

Figure 3: MC3T3-E1 OB attachment on micro HA (dashed line) and nano HA (solid line) scaffolds as a function of time. OBs were seeded onto porous scaffolds (n = 3 with each trial run in triplicate) at a density of 11,320 cells/cm^2 and counted at intervals of 0.5, 1, 2 and 4 hours. Counts were completed after trypsinizing, morselizing and using a hemacytometer. Values are mean ± SE, $p < 0.05$ at all time intervals for comparison of nano HA to micro HA. Figure taken from Smith et al., Int J Nanomed 2006;1:189-194.

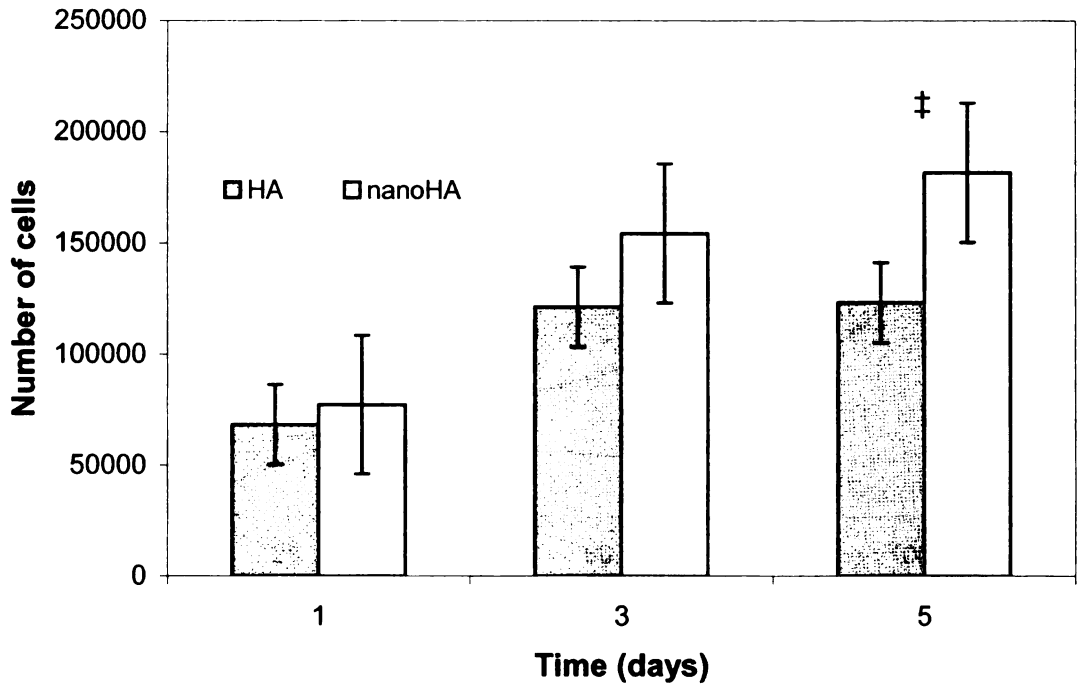

Figure 4: MC3T3-E1 Osteoblast proliferation on micro HA and nano HA. OBs were seeded onto porous scaffolds (n = 3 with each trial run in triplicate) at a density of 11,320 cells/cm^2 and counted after periods of 1, 3 and 5 days. Counts were completed after trypsinizing, morselizing and using a hemacytometer. Values are mean ± SE. $p > 0.05$ for comparison of nano HA to micro HA porous scaffold for 1 and 3 days. $p < 0.05$ for 5 days (‡). Figure taken from Smith et al., Int J Nanomed 2006;1:189-194.

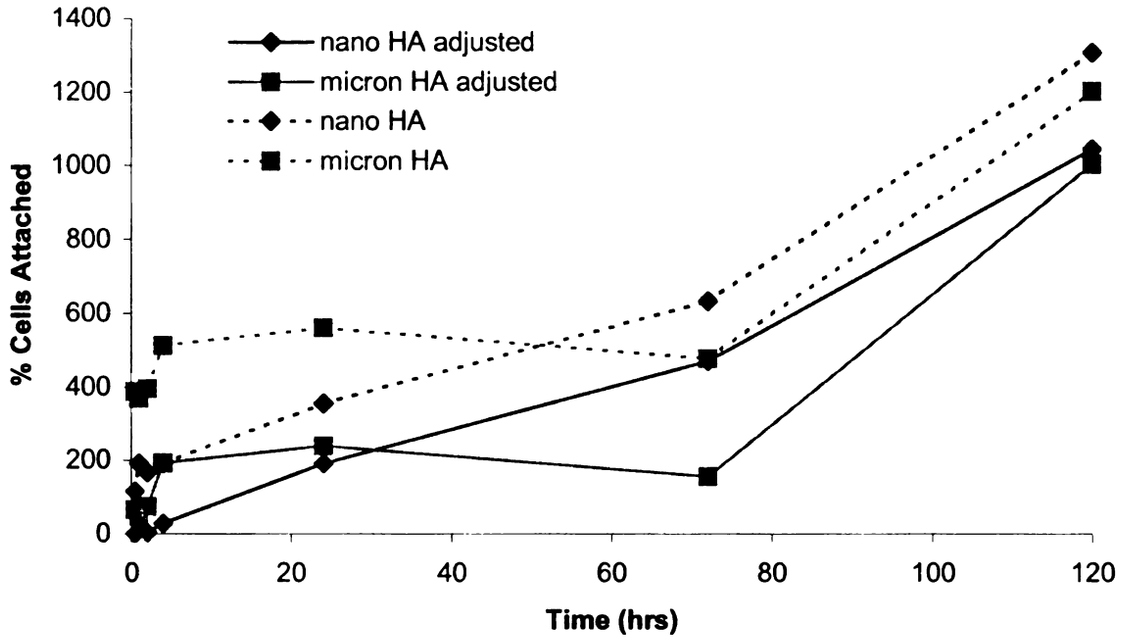

Figure 5: MC3T3-E1 OB attachment (0.5, 1, 2 and 4 hrs) and proliferation (24, 72 and 120 hrs) on porous nano-HA and micron-HA scaffolds. Again, OBs were seeded onto porous scaffolds (n = 3 with each trial run in triplicate) at a density of 11,320 cells/cm^2 and counted at intervals of 0.5, 1, 2 and 4 hours. Counts were completed after trypsinizing, morselizing and using a hemacytometer. Background counts were completed using scaffolds morselized in the absence of OBs and subtracted from the raw data (dotted lines), to yield adjusted values (solid lines). Figure taken from Chapter 4.

The question remains, however, as to what feature(s) associated with reduced grain size in HA lead(s) to increased OB attachment. Therefore, two different grain boundary-associated phenomena in dense HA scaffolds were investigated. In Chapters 5 - 7, the effect of microcracking on OB attachment was evaluated, by inducing microcracks of a known size using a Vickers indentor and in Chapter 8 at the contribution of grain boundary grooving on OB attachment was assessed.

Microcracks resulting from thermal processing of HA were first identified in our work reported in Chapter 5, Part A.[1] In this study, three different CaP materials were sintered and examined using scanning electron

microscopy (SEM). Dense HA specimens (97.7 ± 0.7% of theoretical) with an average grain diameter of 7.9 ± 1.5 μm contained microcracks both along grain boundaries and traversing individual grains.

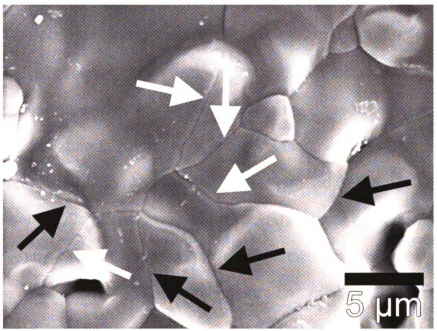

Figure 6: SEM micrograph of an as-sintered hydroxyapatite specimen surface. Image was taken away from the fracture surface (4500x). This micrograph shows multiple examples of microcracking due to thermal expansion in HA, indicated by arrows. White arrows indicate cracks crossing the grain bulk and black arrows indicate cracks along grain boundaries. This type of microcracking is not easily controlled. Image taken from Case et al., Mater Sci Eng A 2005;390:246-254.

Naturally, we wished to study the effect of these microcracks on OB behavior *in vitro*. Bone microdamage including microcracking, has been shown to play a significant role in triggering bone remodeling and we therefore hypothesize that microcracked scaffolds would show improved OB activity. However, the microcracks found in this study resulted from thermal expansion anisotropy (TEA), and only occur above a critical grain size (G_{CR}) for a given material. For HA in particular, the G_{CR} is difficult to estimate and,

therefore, the degree of microcracking due to TEA is difficult to control. We needed to create microcracked HA specimens, where the microcrack number and size could be controlled.

Therefore, we induced controlled microcracks ($2c_{AVE}$ = 124.4 μm ± 21.1 μm) in dense HA, using Vickers microindentation (Figure 7). In Chapters 6 and 7, we observed the effect of this induced microcracking on OB attachment for dense HA at one and four hours. These results are shown again here, in Figure 8. At one hour, the OB attachment was 25.1 ± 8.9% of the total number of OBs plated on the control HA and 31.3% ± 12.7% of the total number of OBs plated on the microcracked HA, with a p-value of 0.25 as determined by Student's t-test. This shows that there was no significant difference between the OB attachment on microcracked and non-microcracked HA specimens. In contrast, in a separate trial at four hours, 29% ± 7.6% of the total OBs attached to the microcracked HA versus 18% ± 6.1% on the control HA, a 61.1% increase. Student's t-test showed that this was a significant increase in the percentage of OB attachment ($p = 0.004$).

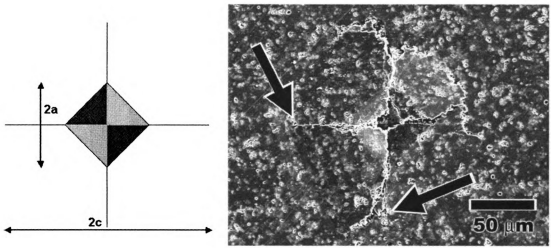

Figure 7: SEM micrograph of microindentation on HA specimen surface (right). "2a" indicates the diagonal length of the indentation impression and "2c" indicates crack length (left). This indent was created using a Vickers microindentor with a load of 4.9 N, a load time of 5 secnds and a loading rate of 70 µm/sec. This method of microcrack induction created microcracks of an average size of $2c_{AVE}$ = 124.4 µm ± 21.1 µm and is more easily controlled compared to TEA-induced microcracking. Indents such as this one were placed in a 14x14 grid across the specimen surface. Image taken from Smith et al., Am J Biochem Biotechnol 2006;2:105-110.

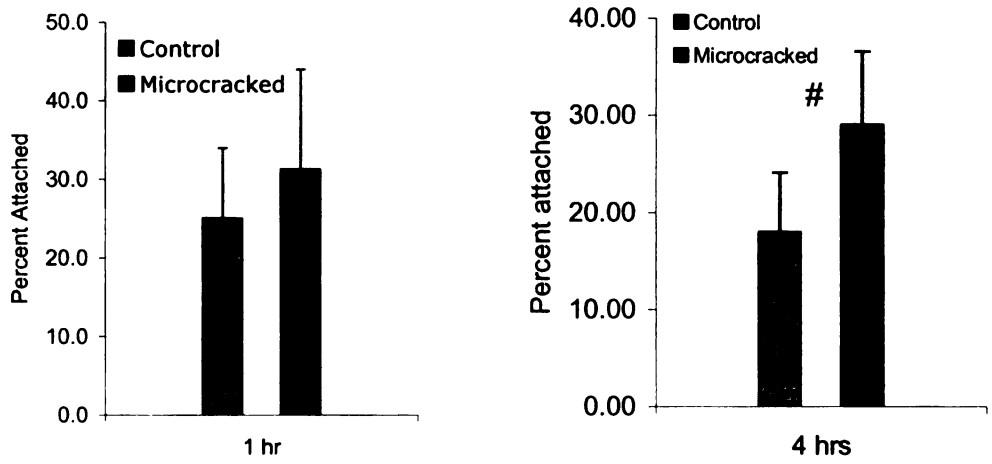

Figure 8: Osteoblast attachment at 1 and 4 hours on microcracked and non-microcracked dense HA discs. OBs were seeded onto dense microcracked and control HA scaffolds (n = 3 with each trial run in triplicate) at a density of 11,320 cells/cm^2 and counted at 1 and 4 hours. Counts were completed after fixing the cells using formaldehyde and staining with both Rhodamine/Phalloidin and Hoescht. Stained cells were viewed under an optical fluorescence microscope and counted in 10 fields of view. Counts were then averaged for each group of 9 specimens (control and microcracked) and the results shown here, with the error bars indicating standard deviation (as opposed to SE, used in Figures 3 and 4). "#" indicates that difference in OB attachment between control HA and microcracked HA at 4 hours is significant ($p = 0.004$). Figure taken from Smith et al., submitted to J Biomed Mater Res, December 2006.

At both 1 and 4 hours, the presence of microcracks at the HA surface did not have a significant effect on OB morphology was shown in figures 9 and 10. In Figure 9, OBs possess either a spread or polygonal morphology on both control and microcracked specimens. In Figure 10, this morphology is also apparent for both groups.

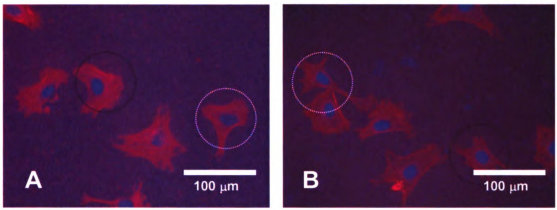

Figure 9: A) MC3T3-E1 OBs with spread (white circle) and polygonal (black circle) morphology on HA control specimen. B) MC3T3-E1 OBs with similar spread (white circle) and polygonal (black circle) morphology on microcracked HA specimen. OBs have been fixed and stained to highlight actin fibers (red – Rhodamine-Phalloidin) and cell nuclei (blue – Hoechst). Images taken from Smith et al., submitted to J Biomed Mater Res, December 2006.

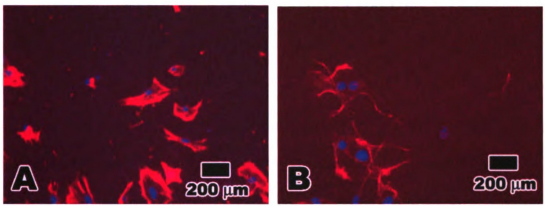

Figure 10: 10A shows MC3T3-E1 osteoblasts with both spindle-shaped and polygonal morphology on HA control specimen after 4 hours culture. OBs were fixed and stained to highlight actin fibers (red – Rhodamine-Phalloidin) and nuclei (blue – Hoechst). 10B shows MC3T3-E1 Osteoblasts with spindle shaped morphology on HA microcracked specimen at 4 hours, again stained to highlight actin fibers (red – Rhodamine-Phalloidin) and nuclei (blue – Hoechst). Images were taken using an optical fluorescence microscope. Images taken from Smith et al. J Am Biochem Biotechnol 2006;2:105-110.

These findings indicate that microcracking does indeed have a positive effect on OB attachment *in vitro* at four hours, and should be investigated further in order to understand its effect on later stage OB behavior, including proliferation, differentiation and calcium production.

While the presence of surface-breaking microcracks in HA scaffolds positively influences OB attachment, it is not likely that this phenomenon contributed to increased OB attachment on the nano-grained dense scaffolds investigated by Webster et al. who found increased OB attachment in nano-scale grain diameter materials (grain diameter < 67 nm). This grain size is below the G_{CR} for TEA-induced microcracking in HA. Since Webster et al. did not induce microcracking, it is unlikely that any microcracks were present in their specimens, due to their very small grain size (< 100 nm).

The second grain boundary phenomenon investigated in this dissertation is grain boundary grooving in dense HA, brought on by thermal etching at 1100°C for 45 minutes following sintering (Figure 11). Grain boundary grooving is estimated to be on the order of 0.5 μm. The surface roughness of grain boundary grooved HA was 10.23 ± 1.8 nm, which is lower than the R_a = 19 - 32 nm reported earlier for nanophase ceramics[2-4].

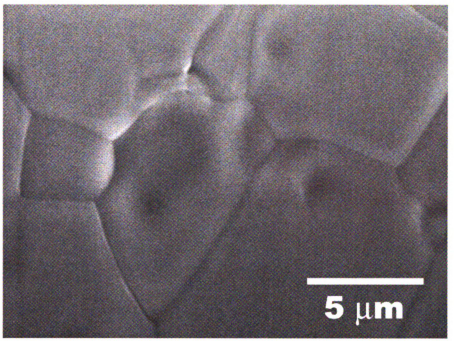

Figure 11: SEM micrograph of the surface of a grain boundary grooved HA specimen. Grain boundary grooving was accomplished by thermally etching sintered dense HA through heating at 1100°C for 45 minutes. Grain boundary grooves shown here are estimated to be approximately 0.5 μm in width (hillock to hillock). Image taken from Chapter 8.

MC3T3-E1 OBs were seeded onto grain boundary grooved and control dense HA discs for one and four hours. The results are shown in Figure 12. At one hour, the mean OB attachment was 45.6 ± 12.2% on control HA and 47.3 ± 12.8% on grain-boundary grooved HA, a non-significant difference ($p = 0.78$). Similarly, at four hours no significant change in the mean OB attachment occurs between the control HA (59.0 ± 13.0%) and grain boundary grooved HA (59.3 ± 23.9%) ($p = 0.98$). This finding indicates that the contribution of grain boundary grooving to the increased OB attachment found for nano-scale HA versus micron-scale HA is not significant.

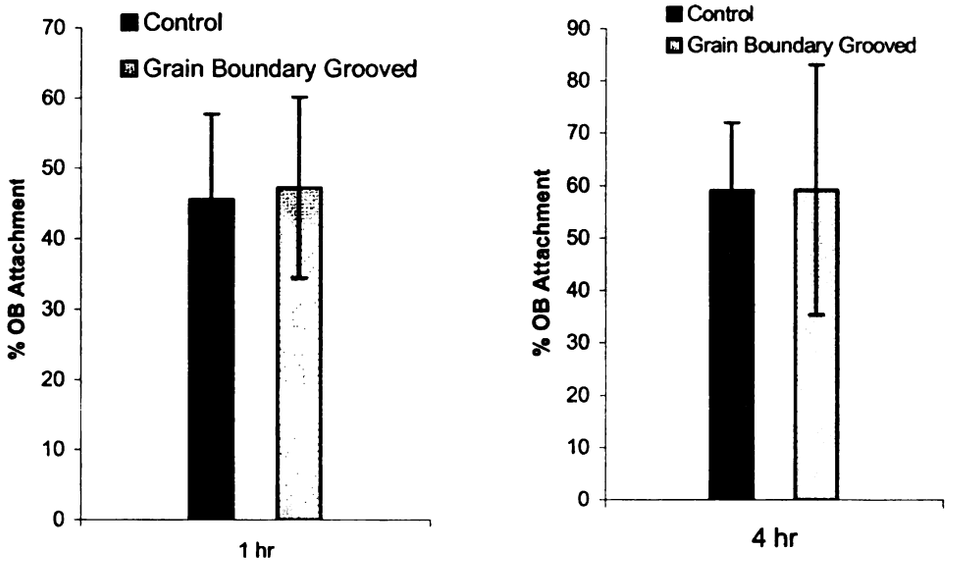

A **B**

Figure 12: MC3T3-E1 OB attachment at 1 (Figure 2A) and 4 (Figure 2B) hours on thermally etched and control HA specimens. OBs were seeded onto dense grain boundary grooved and control HA scaffolds (n = 3 with each trial run in triplicate) at a density of 11,320 cells/cm^2 and counted at 1 and 4 hours. Counts were completed after fixing the cells using formaldehyde and staining with both Rhodamine/Phalloidin and Hoescht. Stained cells were viewed under an optical fluorescence microscope and counted in 20 fields of view. Counts were then averaged for each group of 9 specimens (control and microcracked) and the results shown here, with the error bars indicating standard deviation (as opposed to SE, used in Figures 3 and 4). At both time intervals there is no significant difference between groups. Figure taken from Chapter 8.

This study also found that grain boundary grooving had no significant effect on OB morphology, as shown in Figure 13. While the OB spicule length is shorter at 1 hour than at 4 hours (12 μm ± 8 μm for control and 18 μm ± 8 μm on grain boundary grooved at 1 hour. 24.8 μm ± 10.3 μm for control and 28.8 μm ± 9.4 μm for grain boundary grooved at 4 hours.) there is no difference in OB morphology between control and grain boundary grooved groups at either time point.

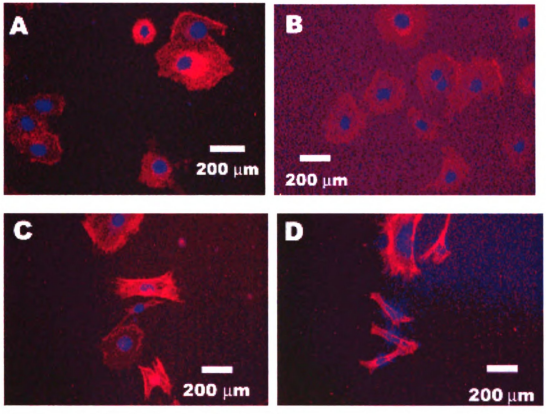

Figure 13: This set of four optical micrographs shows attached OBs at one hour on the surface of a control specimen (Figure 3A) and a grain boundary grooved specimen (Figure 3B), and also at four hours on the surface of a control specimen (Figure 3C) and a grain boundary grooved specimen (Figure 3D). OBs were fixed and stained to highlight actin fibers (red – Rhodamine-Phalloidin) and nuclei (blue – Hoechst). The lesser degree of OB spread in both groups at 1 hour is a result of the shorter culture time. Images were taken using an optical fluorescence microscope. Images taken from Chapter 8.

Conclusions

These results rule out microcracking and grain boundary grooving as contributing factors in increased OB attachment on nano-scale HA substrates, as microcracking due to TEA does not occur at the grain size reported and grain boundary grooving does not significantly increase OB attachment. However, this does mean that a porous nano-grained scaffold may not exhibit increased OB attachment were cracks introduced via other means, such as an applied mechanical force. This indicates that the role that grain boundaries

play in increased OB attachment for nano-grained HA is related to either the presence of a grain boundary phase or variation in surface charge associated with those regions.

Ceramic grain boundaries often possess a precipitated solute or a separate phase.[5,6] An amorphous phase has been shown to form during sintering in several polycrystalline ceramics including Si_3N_4[7], high alumina ceramics[8] and ZrO_2[9]. As the grain size is reduced, the grain boundary length per unit area increases. With the presence of a continuous amorphous grain boundary phase the surface area fraction of this glassy phase increases as well. Glassy biomaterials have been shown to increase appositional bone growth when compared to crystalline biomaterials[10] where the presence of a continuous amorphous phase has been linked to enhanced OB attachment and eventual bone growth. Glassy biomaterials, such as 45S5 Bioglass, have been shown to promote bone formation *in vivo* and are being evaluated for potential applications.[11] Recently, it was discovered that nano-crystalline and nano-amorphous HA elicited similar OB responses to RGD functionalized conventional HA.[12] Even without the presence of an amorphous grain boundary phase, the decrease in crystallinity associated with decreased grain size may promote OB attachment and should be investigated further.

Using transmission electron microscopy (TEM), an amorphous, glassy grain boundary phase was found on nano-grained HA taken from dental enamel.[13] This amorphous phase did not develop as a result of sintering and observation of *non*-biological HA using TEM found no evidence of an

amorphous grain boundary phase. This is consistent with the lack of amorphous grain boundary grain observed in sintered HA by Kleebe et al, where high-resolution electron microscopy (HREM) was used to image grain boundaries in sintered undoped HA.[14]

Increased surface roughness resulting from decreased grain size is a likely contributor to improved OB behavior. In addition to several studies by Webster et al., in which increased surface roughness in ceramic materials led to increases in OB attachment and proliferation, OB behavior has been shown to improve with increased surface roughness on various biomedical alloys, including Ti alloys[15,16] and 316L stainless steel.[17]

When viewed in concert with prior work, and by effectively ruling out microcracking and grain boundary grooving as determining factors in OB attachment on nanograined dense HA, our research suggests that increased OB attachment may result from increased porosity and surface topography. The nanometer-scale roughness found in nano-grained ceramics is most similar to that found in living bone.[18] Therefore, while grain boundaries may not directly improve OB attachment, they are another surface feature within a more biomimetic topography.

REFERENCES

1. Case ED, Smith IO, Baumann MJ. Microcracking and porosity in calcium phosphates and the implications for bone tissue engineering. Mat Sci and Eng A. 2005;390:246-254.

2. Webster TJ, Ergun C, Doremus RH, Siegel, RW Bizios R. Nanocrystalline hydroxyapatite enhances osteoblast function. In: The Proceedings of the First Joint BMES/EMBS Conference, Atlanta, GA; 1999. p744.

3. Webster TJ, Siegel RW, Bizios R. Design and evaluation of nanophase alumina for orthopaedic/dental applications. Nanostruct Mater 1999;12:983-986.

4. Webster TJ, Siegel RW, Bizios R. Osteoblast adhesion on nanophase ceramics. Biomaterials 1999;20:1221-1227.

5. Kingery WD. Plausible concepts necessary and sufficient for interpretation of ceramic grain-boundary phenomena: I, Grain-boundary characteristics, structure, and electrostatic potential. J Am Ceram Soc 1974;57:1-8.

6. Kingery WD. Plausible concepts necessary and sufficient for interpretation of ceramic grain-boundary phenomena: II, Solute segregation, grain-boundary diffusion, and general discussion. J Am Ceram Soc 1974;57:74 - 83.

7. Jin Q, Ning XG, Wilkinson DS, Weatherly GC. Redistribution of a grain-boundary glass phase during creep of silicon nitride ceramics. J Am Ceram Soc.1997;80:685–691.

8. Powell-Dogan CA, Heuer AH. Devitrification of the grain boundary glassy phase in a high-alumina ceramic substrate. J Am Ceram Soc 1994;77:2593–2598.

9. Kobayashi S. X-ray microanalysis of the boundary phase in partially stabilized zirconia (PSZ). J Mat Sci Letters 1985;4:268-270.

10. Fujishiro Y, Hench LL, Oonishi H. Quantitative rates of in vivo bone generation for Bioglass and hydroxyapatite particles as bone graft substitute Journal of Materials Science: Materials in Medicine 1997;8:649 - 652.

11. Lu HH, Pollack SR, Ducheyne P. Temporal zeta potential variations of 45S5 bioactive glass immersed in an electrolyte solution J Biomed Mater Res 2000;51:80-87.

12. Anselme K, Bigerelle M, Noel B, Dufresne E, Judas D, Iost A, Hardouin P. Qualitative and quantitative study of human osteoblast adhesion on materials with various surface roughnesses. J Biomed Mater Res 2000;49: 155-166.

13. Kleebe HJ, Bres EF, Berache-Assolant D, Ziegler G. High-resolution electron microscopy and convergent-beam electron diffraction of sintered undoped hydroxyapatite. J Am Ceram Soc 1997;80:37–44.

14. Balasundaram G, Sato M, Webster TJ. Using hydroxyapatite nanoparticles and decreased crystallinity to promote osteoblast adhesion similar to functionalizing with RGD. Biomaterials 2006;27:2798-2805.

15. Wen S, Liu Q. High resolution electron microscopy investigations of interface and other structure defects in some ceramics. Microsc Res Tech 1998;40:177-186.

16. Webster TJ, Ejiofor JU. Increased osteoblast adhesion on nanophase metals: Ti, Ti6Al4V, and CoCrMo. Biomaterials 2004;25:4731–4739.

17. Hao L, Lawrence J, Phua YF, Chian KS, Lim GC, Zheng HY. Enhanced human osteoblast cell adhesion and proliferation on 316 LS stainless steel by means of CO_2 laser surface treatment J Biomed Mater Res B: Appl Biomat 2005;73: 148-156.

18. Kaplan FS, Hayes WC, Keaven TM, Boskey A, Einhorn TA, Iannotti JP. In: Simon, SR, editor. Orthopaedic basic science. Columbus, OH: American Academy of Orthopaedic Surgeons, 1994: p127.

CHAPTER 10

FUTURE WORK

Our results naturally suggest two paths of future study. The first is a further investigation into why a decrease in grain size leads to an increase in OB attachment. Although this work has ruled out microcracking and grain boundary grooving as contributing factors to increased OB attachment in HA, and others have shown no evidence of a separate grain boundary phase in non-biological HA, this reduction in grain size has still been shown to positively affect OB attachment *in vitro*.[1-3] Specifically future work will determine whether this relationship is due to differences in surface charge associated with grain boundaries in HA.

The second path is to further study the effect of microcracking on bone regeneration. We have determined that the presence of induced microcracks in HA increases OB attachment and we hypothesize that this is an indication that the presence of microcracks is initiating the bone remodeling process. In living bone, remodeling begins with damage to adjacent osteocytes, which apoptose, signaling continued remodeling. Future work will investigate whether induced microcracking leads to osteocyte apoptosis. Additionally, *in vitro/in vivo* studies using porous, nano-grained scaffolds with induced microcracking will be conducted.

Surface charge variation and OB attachment on HA

A factor which has not yet been linked to increased OB attachment is nanoscale surface charge variation associated with grain boundaries in ceramics. In the 1974 Sosman Memorial Lecture at the American Ceramics Society, Kingery supported the concept that grain boundaries carry an electric charge, by measuring associated space-charge clouds in NaCl (-), Al_2O_3 (+) and MgO (-).[4]

In our own work[6-8] (Appendix E-F), as well as numerous other studies[9-11] electrophoresis has been used to measure the ζ-potential, which is an estimate of the surface potential, associated with particulate biomaterials. This technique works well to quantify the average potential across a material surface, but does not effectively quantify the charge variations associated with grain boundaries. Vandiver et al. have more recently employed high-resolution force spectroscopy to measure directly the force required to separate the probe tip from the surface in HA.[12] By collecting these measurements across several grains at the HA surface, the surface charge was approximated and found to be higher near grain boundaries. This increase in surface charge with finer grain sizes should more effectively attract the negatively charged OBs[6], and explains the increase in OB attachment found in nano-grained HA.

To determine whether this is true, dense HA substrates will be fabricated using the techniques described in Chapters 5 - 8. By using a nano-scale starting HA powder and varying the sintering time, HA discs will be

fabricated in two distinct groups: 100 nm grain diameter and 1 μm grain diameter (as determined by SEM). These grain sizes are below the accepted values of G_{CR} for HA and have been chosen to prevent TEA-induced microcracking. Both specimen groups will be polished to > 1 μm and the average surface roughness determined using atomic force microscopy (AFM). By assuring that that the difference in mean surface roughness between these two groups is not significant, the effect of increased surface roughness on OB attachment is eliminated.

MC3T3-E1 OBs will then be seeded onto both specimen groups and cell attachment quantified at 0.5, 1, 2 and 4 hours, using optical microscopy. OBs will be fixed and stained using Hoescht (to image cell nuclei) and Rhodamine-Phalloidin (to image cell morphology) fluorescent stains, then imaged using a Leica DM IL optical fluorescence microscope (Leica Microsystems, Wetzlar, Germany) equipped with a SPOT RT camera system (SPOT Diagnostic Instruments, Sterling Heights, MI). OBs from 20 fields of view will be counted, to create an accurate representation of OB attachment across the HA surface. Students t-test will be used to determine the significant difference between groups.

Future work in microcracking and OB attachment on HA

The findings included in the previous chapter effectively rule out microcracking and grain boundary grooving as phenomena that contribute to increased osteoblast (OB) attachment associated with reduced grain size in

dense hydroxyapatite (HA).[10-12] However, microcracking has a positive effect on OB attachment when it is present in larger-grained HA. This new finding[13] merits a further investigation into this relationship, and whether or not the observed increase is tied to the role of microdamage in bone regeneration.

The idea that microcracking in bone results from fatigue and is linked to the remodeling process was originally presented by Frost in 1960[14] and is discussed in detail in Chapters 6 and 7. Targeted remodeling[15] occurs at sites of localized microdamage as observed in studies by Johnson et al., Burr et al. and Mori et al.[16-19] where osteoclasts act to resorb damaged bone, including osteocytes.[20] This resorption is regulated by the condition of the osteocyte synctinium in these local regions and osteocyte damage and subsequent apoptosis leads to increased osteoclast activity.

The osteocyte is one of three bone cell-types. The other two are the osteoblast (bone-forming cell) and osteoclast (bone-eroding cell).[21] Osteocytes begin life as osteoprogenitors, which differentiate into osteoblasts. These osteoblasts help in the formation of osteoid. Some osteoblasts become trapped within the newly formed osteoid and become osteocytes, residing within the lacunae. As the osteoid matrix forms, the mineralization front surrounds the osteocytes. Once surrounded, the cells extend long, thin processes toward the vasculature. It is through these processes, as well as gap junctions, that the osteocytes form a functional syncytium.[22]

The osteocyte syncytium is the subject of interest in the proposed study. It is theorized that a relationship exists between osteocyte health and

bone volume, with a higher cell number causing increased extracellular matrix volume.[23] Osteocyte number density has also been tied to the amount of microdamage accumulated in bone.[24] It has also been theorized that osteocytes undergo apoptosis with the incidence of linear microcracking, prior to bone remodeling[25-28] leading to the supposition that apoptosis is a key part of the resorption process, by serving to direct osteoclasts to damaged sites.[29]

To determine whether this process is initiated by induced microcracking in HA, discs will be prepared by uniaxial pressing as described in Chapters 5 - 8. A starting powder with a diameter small enough to yield a sintered grain size > G_{CR} will be used to avoid TEA-induced microcracking[30,31]. Rather, controlled microcracks will be induced using a Vickers microindentor as described in Chapters 6 - 7.

To determine the spatial relationship between osteocyte apoptosis and microcracking, samples will be prepared by creating discreet regions of microcracking, using Vickers indentation.

Osteocytes will be cultured in the presence of these dense HA discs. The number of apoptotic cells will be assessed after a prescribed time and cell density and apoptosis will be reported as a function of average microcrack length (mm) and density (cracks/mm^2). Cell density will be determined by staining and counting with an optical microscope. Statistical significance will be determined using the Student's t-test.

Additionally, the proximity of apoptotic cells to regions of microcracking will be assessed using scanning electron microscopy (SEM), confocal laser scanning microscopy (CLSM) or fluorescent light microscopy.

REFERENCES

1. Webster TJ, Ergun C, Doremus RH, Siegel RW, Bizios R. Nanocrystalline hydroxyapatite enhances osteoblast function. In: Proceedings of the First Joint BMES/EMBS Conference, Atlanta, GA; 1999. p744.

2. Webster TJ, Siegel RW, Bizios R. Design and evaluation of nanophase alumina for orthopaedic/dental applications. Nanostruct Mater 1999;12:983-986.

3. Webster TJ, Siegel RW, Bizios R. Osteoblast adhesion on nanophase ceramics. Biomaterials 1999;20:1221-1227.

4. Kingery WD. Plausible concepts necessary and sufficient for interpretation of ceramic grain-boundary phenomena: I, Grain-boundary characteristics, structure, and electrostatic potential. J Am Ceram Soc 1974;57:1-8.

5. Kingery WD. Plausible concepts necessary and sufficient for interpretation of ceramic grain-boundary phenomena: II, Solute segregation, grain-boundary diffusion, and general discussion. J Am Ceram Soc 1974;57:74-83.

6. Smith IO, Baumann MJ, McCabe LR. Electrostatic interactions as a predictor for osteoblast attachment to biomaterials J Biomed Mater Res 2004;70:436-441.

7. Smith IO, Soto MK, Baumann MJ, McCabe L. In vitro stability predictions of osteoblast interaction with hydroxyapatite and β-tricalcium phosphate In: Sundar V, Rusin RP, Rutiser CA. Bioceramics: Materials and Applications IV, Proceedings of the 105th Annual Meeting of the American Ceramic Society, Nashville, TN; 2003. p121-131.

8. Smith IO, Baumann MJ, Obadia L, Bouler JM. Surface potential and osteoblast attraction to calcium phosphate compounds is affected by selected alkaline hydrolysis processing. J Mater Sci Mater Med 2004;15:841-846.

9. Ducheyne P, Kim CS, Pollack SR. Effect of phase differences on the time-dependent variation of the zeta potential of hydroxyapatite J Biomed Mater Res 1992;26:147-168.

10. Lu HH, Pollack SR, Ducheyne P. Temporal zeta potential variations of 45S5 bioactive glass immersed in an electrolyte solution J Biomed Mater Res 2000;51:80-87.

11. Knowles JC, Callcut S, Georgiou G. Characterization of the rheological properties and zeta potential of a range of hydroxyapatite powders. Biomaterials 2000;21:1387-1392.

12. Vandiver J, Dean D, Patel N, Bonfield W, Ortiz C. Nanoscale variation in surface charge of synthetic hydroxyapatite detected by chemically and spatially specific high-resolution force spectroscopy. Biomaterials 2005;26:271-283.

13. Smith IO, Baumann MJ, Case ED. Induced microcracking affects osteoblast attachment on hydroxyapatite scaffolds for tissue engineering. Am J Biochem Biotechnol 2006;2:105-110.

14. Frost HL. Presence of microscopic cracks in vivo in bone. Henry Ford Hospital Med Bull 1960;8:27-35.

15. Burr DB. Targeted and nontargeted remodeling. Bone 2002;30:2-4.

16. Johnson KA, Skinner GA, Muir P. Site-specific adaptive remodeling of Greyhound metacarpal cortical bone subjected to asymmetrical cyclic loading. Am J Vet Res 2001;62:787-793.

17. Burr DB, Martin RB, Schaffler MB, Radin EL. Bone remodeling in response to in vivo fatigue microdamage. J Biomech 1985;18:189-200.

18. Burr DB, Martin RB, Martin PA. Lower extremity loads stimulate bone formation in the vertebral column: implications for osteoporosis. Spine. 1983;8:681-686.

19. Mori S, Burr DB. Increased intracortical remodeling following fatigue damage. Bone 1993;14:103-109.

20. Bronckers ALJJ, Goei , Luo G, Karsenty G, D'Souza RN, Lyaruu DM, Burger EH. DNA fragmentation during bone formation in neonatal rodents assessed by transferase-mediated end labeling. J W Bone Miner Res 1996;11:1281-1291.

21. Young B, Heath JW. Wheater's Functional Histology. Edinburgh: Churchill Livingstone; 2000. 413p.

22. Knothe Tate ML, Adamson JR, Tami AE, Bauer TW. The osteocyte. Int J Biochem Cell Biol 2004;36:1-8.

23. Vashishth D. Rising crack-growth-resistance behavior in cortical bone: implications for toughness measurements. J Biomech 2004;37:943-946.

24. Vashishth D, Verborgt O, Divine G, Schaffler MB, Fyhrie DP. Decline in osteocyte lacunar density in human cortical bone is associated with accumulation of microcracks with age. Bone 2000;26:375-380.

25. Noble BS, Stevens H, Loveridge N, Reeve J. Identification of apoptotic changes in osteocytes in normal and pathological human bone. Bone 1997;20:273-282.

26. Qiu S-J, Hoshaw SJ, Gibson GJ, Lundin-Cannon KD, Schaffler MB. Osteocyte apoptosis in reaction to matrix damage in compact bone. In: Proceedings of the 43rd Annual Meeting of the Orthopedic Research Society, San Francisco, CA; 1997. p89.

27. Verborgt O, Gibson GJ, Schaffler MB. Loss of osteocyte integrity in association with microdamage and bone remodeling after fatigue in vivo. J Bone Min Res 2000;15:60-67.

28. Noble BS, Peet N, Stevens HY, Brabbs A, Mosely JR, Reilly GC, Reeve J, Skerry TM, Lanyon LE. Mechanical loading: biphasic osteocyte survival and targeting of osteoclasts for bone destruction in rat cortical bone. Am J Physiol Cell Physiol 2003;284:934-943.

29. Colopy SA, Benz-Dean J, Barrett JG, Sample SJ, Lu Y, Danova NA, Kalscheur VL, Vanderby Jr R, Markel MD, Muir P. Response of the osteocyte syncytium adjacent to and distant from linear microcracks during adaptation to cyclic fatigue loading. Bone 2004;35: 881-891.

30. Case ED, Smith IO, Baumann MJ. Microcracking and Porosity in Calcium Phosphates and the Implications for Bone Tissue Engineering. Mater Sci Eng A 2005;390:246-254.

31. Hoepfner TP, Case ED. An estimate of the critical grain size for microcracks induced hydroxyapatite by thermal expansion anisotropy. Mater Lett 2004;58:489-492.

APPENDIX A

THREE-DIMENSIONAL MICROSTRUCTURAL CHARACTERIZATION OF POROUS HYDROXYAPATITE USING CONFOCAL LASER SCANNING MICROSCOPY (CLSM)

FEI REN, IAN O. SMITH, MELISSA J. BAUMANN AND ELDON D. CASE
Department of Chemical Engineering and Materials Science Department
Michigan State University, East Lansing, MI 48824

PUBLISHED IN: International J Appl Ceram Technol 2005;2:200-211.

ABSTRACT

The characterization of porosity is crucial in the development and commercialization of ceramic bone replacement technology, since the pore size and interconnectivity play a central role in both biological function (bone ingrowth and nutrient flow) as well as mechanical properties of bone scaffolds. The ability of Confocal Laser Scanning Microscopy (CLSM) to image three-dimensional structures with large vertical depths (~ 2 mm) and fine vertical resolution (~ 1 μm) is utilized in this paper to characterize the 3-D microstructures of hydroxyapatite (HA) bone scaffold specimens with porosity ranging from roughly 60 to 70 volume percent. Various CLSM techniques are applied to image and interpret the HA pore structure, including Z-series stacking, topographic profiling, and Phi-Z scanning and contour mapping.

INTRODUCTION

The Confocal Laser Scanning Microscope (CLSM) has become, over the last 10 to 15 years, a standard instrument for the study of soft biological tissues. Many studies of normal and tumor cells[1], biofilms [2], proteins [3], brain tissue [4], skin tissue [5], corneal tissue [6], etc. are published each year. Despite the widespread use of CLSM for soft tissue research, there is still very limited use of CLSM for "hard biomaterials" (such as bone and teeth) or more generally for the field of materials science. This study utilizes the CLSM to characterize the porosity in hydroxyapatite (HA) that is the major component in the burgeoning demand for ceramic bone tissue engineering replacement materials.

Disease and traumatic injury result in a critical need for bone replacement materials, as evidenced by the large number of bone grafts (more than 500,000 annually in the U. S. [7]. While bone tissue harvested from alternate sites in the patient (autograft) may often be an ideal replacement for the case of spongy (cancellous) bone, load bearing autografts are problematic because removing load bearing (cortical) bone from a donor site in a patient *may require* a repair/replacement at that site. Although bone harvested from other donors (allograft from cadavers) can be ground and used as part or all of such replacement material, the possibility of disease transmission makes the use of allograft bone tissue problematic. Thus, as an attractive alternative, there has been considerable work done to develop artificial bone replacement materials consisting of bioceramics such as hydroxyapatite (HA). Currently,

approximately 60% of the bone graft materials use calcium phosphate-based materials which are commercially available as a paste, putty, solid matrix and as granules [7] and are supplied by all of the world's major orthopaedic corporations. Because of the biological and mechanical necessity of forming a strong bone/bioceramic interface, the development and long term success of these synthetic bone tissue scaffolds is highly dependent on characterizing the pore size, morphology and interconnectivity, since both the biological and mechanical functions of such scaffolds depends on the details of the pore microstructure of these materials.

In this study, we utilize the CLSM confocal reflection mode to characterize the surface topology of both macropores and micron-scale features in porous HA bone scaffold materials. In addition, we use the confocal fluorescence mode to image surface features. As part of this study, we have begun the process of modifying the experimental procedures developed by Fredrich et al. (to study porous geological materials) [8] so that the fluorescence mode can be applied to the considerably larger pores found in our bone scaffold materials. In total, we have examined 11 HA bone scaffold specimens (6 with epoxy impregnation and staining and 5 in the as-sintered state). This study presents CLSM images from 11 specimens having approximately 60 to 70 volume percent porosities.

BACKGROUND

Porous HA ceramics: biological and mechanical implications of porosity

To underscore the importance of characterizing the porosity of HA scaffolds, we shall first discuss the central role that porosity plays on both the biological and mechanical properties of these materials. Moreover, for the biological function of bone, a bimodal pore architecture is needed. The bone tissue engineering community classifies pores about 200 - 400 μm across as macropores and interconnecting pores roughly 60-70 μm in diameter as "micropores".

Biological implications of porosity

For synthetic bioceramic bone scaffolds, bimodal porosity is essential for bone-ingrowth as well as the attachment of the ceramic scaffold to the bone [9-12]. These pores assist the process of bone ingrowth into the synthetic bone scaffold materials (fabricated from porous HA) where the newly forming bone penetrates into the pores of the scaffold and if a resorbable phase of HA is used for the scaffold, eventually replace the ceramic with neobone [13]. Hing et al. have found that microporosity is especially important for the early stages of bone ingrowth (osseointegration), in that increasing the volume fraction of microporosity can improve the bioactivity of the porous HA [11]. In addition to the "early biological response", the "mechanical properties of a porous

hydroxyapatite bone graft substitute are highly sensitive to its pore structure" [12].

A bimodal pore size distribution also is important in the controlled release of antibiotics from porous HA bone scaffold materials [14], especially in terms of interconnective pores between the micro and macro porosity [10].

Impact of porosity on mechanical properties of bone scaffolds

For ceramic materials, including bioceramics, porosity leads to exponential decreases in the elastic modulus [15-19], hardness [20] and fracture strength [18, 19, 21, 22] along with dramatic decreases in fracture toughness [23] and the critical strain energy release rate [23]. For bioceramics, such as HA in particular, porosity directly affects the tensile strength [24], the compressive strength [24, 25] and the hardness [20]. Thus, the mechanical integrity and viability of the bone scaffold materials is also closely linked with the details of the pore architecture.

Using the CLSM to characterize porous HA specimens

One method of examining the pore distribution (size and spatial arrangement) is by means of serial sectioning. Typically, this is done by mechanical sectioning, where the specimen is sectioned (cut) by a saw to reveal the sub-surface pore structure. Disadvantages of serial sectioning by mechanical means of course include the inevitable damage caused by the sectioning process, including the portions of the specimen that are destroyed

in the saw kerf. (For a typical low speed diamond blade that is on the order of 0.35 mm thick, 10 diamond saw cuts will destroy the equivalent of a 3.5 mm thick slab of the specimen). Mechanical sectioning also is tedious and time consuming and in addition to the damage caused by the saw kerf, additional specimen damage is incurred in brittle materials due to chipping and spalling near the cut.

Of course, it would be preferable if the specimen could be sectioned either by optical or electronic means, thus eliminating the damage generated by repeatedly cutting the specimen. For the CLSM, since the image is constructed from a series of images taken at slightly different focal planes, the image (rather than the specimen) can be sectioned or rotated electronically.

For topology studies using the CLSM, no surface preparation is required. However, for standard scanning electron microscope samples, coating the surface is required as well as placing the specimens in a vacuum. Even for the environmental scanning electron microscope (ESEM), the specimen needs to be viewed from within a chamber that requires partial vacuum. In contrast, specimens can be examined in the CLSM at one atmosphere ambient pressure, at room temperature and without a conductive coating. Of course, for the CLSM, if one desires to immerse the specimen in water or place the specimen in a particular atmosphere, this can be done in principle using an environmental chamber. In addition, the shape and size of specimens observed using CLSM are much more flexible than those using SEM.

In addition to the CLSM, there are alternative methods to image porous bioceramic and bone materials. For example, micro-computed tomography (μCT) is utilized for non-destructive two-dimensional[26, 27] and three-dimensional[28] image of bone and HA, with resolutions ranging from about 1 to 100 μm. The best resolution (about 1 μm) for μCT is possible only using extremely high-flux sources, such as x-ray synchrotron radiation. For example, the European Synchrotron Radiation Facility was recently used to image bone ingrowth in calcium phosphate bioceramics in three dimensions.[29] The effective resolution was approximately 1.4 μm for long rod specimens 0.6 mm X 0.6 mm X 10 mm, examined perpendicular to the long axis of the rods.[29] (It is relatively typical that for three-dimensional images formed by x-ray synchrotron radiation that the characteristic dimension of the specimen is on the order of 1 mm or less). Also, it should be noted that synchrotron x-ray radiation facilities are large, centralized facilities for which one competes with other researchers to schedule beamtime on the facility. Thus, with synchrotron radiation, the specimen sizes are relatively small, the equipment is available only at centralized facilities and the high x-ray flux rules out applying the technique to studies of bioceramics or bone on which there are living cell cultures. In contrast, the CLSM is a relatively inexpensive, the specimen size is quite flexible, the maximum axial and radial resolutions are on the order of a few microns, depending on the wavelength of the laser source and the numerical aperture of the objective lens (Section 3.3). In addition, the CLSM is widely used for *in-vivo* studies in biological and

biomedical applications[30, 31], thus the CLSM offers the potential to study, for example, osteoblast cell cultures on bioceramics such as HA.

Magnetic resonance (MR) techniques, including high resolution MR (hrMR) and micro-MR (μMR) are also used to image HA and bone specimens. However, in 2005, Hudelmaier et al. noted that "clinical high-resolution (hr) MRI scanners have recently reached a sufficient spatial resolution (around 100 - 200 μm) to quantify microstructural parameters of trabecular bone at peripheral skeletal sites *in* vivo." Also, current hrMR and μMR does not easily allow for the compositing of two-dimensional image slices in order to form for three-dimensional images.[32] Thus, while the hrMR and the micro-MR have the ability to study cells *in* vivo, these techniques lack the resolution of μCT or the CLSM.

EXPERIMENTAL PROCEDURE

Materials and specimen preparation

The porous hydroxyapatite (HA) specimens used in this study were fabricated using medical grade, sintered HA powder (HiMed, Old Bethpage, New York) with an initial particle size of approximately 10μm. For the most porous samples, approximately 28.5 g of HA powder was combined with 13.7 ml 10^{-3} M KNO_3 solution, forming a slurry. To this slurry, 1.1 ml of 30% H_2O_2 was added. The modified slurry was then placed into silicone cylindrical molds. The molds were covered with aluminum foil and placed in a gravity convection oven at 125°C for 1hr to dry the cylinders. After drying, the molds

were removed and the (green) samples ejected. The green (unfired) cylindrical specimens were approximately 1.3 cm in diameter and 1.6 cm in length. Cylinders were then sintered in air for 4 hours at 1360°C, with a heating/cooling rate of approximately 10°C/min. This procedure was repeated for differing sample porosities, with modifications, as discussed below.

The HA specimens included in this study having porosities ranging from approximately, 60 to 70 volume percent. Porosity was varied by altering the concentration of H_2O_2 used in foaming, as well as the HA/KNO_3 ratio in the slurry. Porosity was determined either by Archimedes method or by comparing the theoretical mass to the actual mass. For specimens having the highest porosity, the specimens were foamed using a 30% H_2O_2 solution and an HA/KNO_3 ratio of approximately 2:1. Less porous specimens were foamed using a higher HA/KNO_3 ratio and a lower concentration of H_2O_2 [33].

The specimens were foamed and then sintered. The sintered specimens were cylindrical, approximately 3 cm in length and about 1 cm in diameter. The tops of the molds were open during foaming, so that a mushroom-like dome formed on top of the specimen as it foamed in the mold. Using a diamond abrasive wafering saw at ~200 rpm, the domed-ends of the sintered specimens were sliced off and the remaining cylinder roughly sectioned into 2 cm lengths. The dome section was not utilized because of inconsistent porosity. These highly porous samples were either mounted whole or sectioned further using a padded specimen holder to avoid crumbling. For reflective CLSM mode, specimens were sectioned to 1 cm lengths prior to

viewing while the specimens viewed in fluorescence were cut to 2 mm lengths. Thus, in this study, the maximum dimensions of the specimens were determined by the size of the molds used to form the specimens. The subsequent sectioning was carried out to conserve the amount of epoxy used in the fluorescence mode specimens and hydroxyapatite used for both the fluorescence and reflection mode specimens. Viewing much larger samples is possible with the CLSM (Section 3.2).

Following a procedure developed by Fredrich [8] for imaging the pore structure in 3-D geological specimens, a dye-impregnated epoxy was prepared by dissolving Rhodamine B into a Spurr resin kit. The Spurr kit is a four-part epoxy, consisting of Noneyl Succinic Anhydride (NSA), Vinyleyclohexane (VCD), Dow Epoxy Resin 736 (DER) and Dimethylaminoethanol (DMAE) normally combined at a ratio of 120:20:12:1 to form the epoxy. The viscosity of the epoxy can be customized to the porosity of the sample, increasing the amount of DMAE increases the viscosity. By increasing the proportion of DMAE by a factor of 3 relative to that used by Fredrich [8], we achieved an epoxy with the desired viscosity, allowing for more effective pore intrusion. These components are then combined at 30:5:3:1 and Rhodamine added to the resulting mixture at 1:2000 by weight. The dye was incorporated by stirring with a metal spatula for 5 minutes, followed by transferring the mixture to a centrifuge tube and mixing via vortex for 1 minute. Any air incorporated during mixing was removed by centrifugation at 2000 rpm for 5 minutes resulting in an epoxy ready for use.

Ring-shaped sections of polyvinyl chloride pipe (PVC: OD = 2.15 cm, ID = 1.5 cm) were cut to 2.5 cm in length using a coping saw, then attached to small petri dishes (Becton Dickinson, Franklin Lakes, NJ) using super glue. HA samples were next placed into the newly formed reservoirs and the epoxy preparation poured onto the HA. Care was taken to completely cover the HA specimens with epoxy. The epoxy coated HA samples in their reservoirs were then placed into a dark vacuum chamber which was evacuated to 88 kPa (0.87 atm) for 12 hours. Following the time in the vacuum chamber, the specimens were placed into a gravity convection oven at 65 °C for 24 hours to completely cure the epoxy. The bottom of the Petri dish was cut along the outer circumference of the PVC ring without disturbing the super glue bond between the sample and the Petri dish leaving the sample attached to the flat Petri dish surface. Samples were then sectioned to 2 mm at the petri dish end, using a diamond wafering saw operating at 200 rpm. Exposed sample surfaces were next sequentially polished using a diamond abrasive paste at 6 μm, 1 μm, and 0.1 μm, rinsed with RO water and dried in air. Samples were stored in the dark to avoid photobleaching.

Two types of specimens were observed, namely (1) specimens that were mounted without epoxy impregnation or staining and (2) specimens that were both epoxy impregnated and stained.

CLSM Observation

Two different CLSM instruments were used for this study: (1) LSM 210 (Carl-Zeiss Inc. Jena, Germany) and (2) LSM 5 Pascal (Carl-Zeiss Inc. Jena, Germany).

The LSM 210 CLSM is equipped with 488 nm, 514 nm Ar laser and 633 nm HeNe laser illumination. In the study of topology, a confocal reflection mode was used with the 488 nm Ar laser illumination that has the shortest wavelength available for this instrument and in turn gives the highest resolution. To increase the signal to noise ratio, a low pass filter program was applied to the topographical images after the images were collected.

The LSM 5 Pascal has the following laser sources: Ar laser (458 nm, 488 nm, and 514 nm) and HeNe laser (543 nm and 633 nm). For the study of pore space impregnated with epoxy and stain, the 488 nm Ar laser was used. The emission fluorescence was collected via a long pass filter LP560. A line average of 4 was applied when collecting images to reduce noise.

All images included in this paper are composed of 512 pixels x 512 pixels. The aspect ratio (X: Y) of the LSM 210 is 3:2, thus images collected on this CLSM are thus elongated in X direction. The lateral resolution (LR) and axial resolutions (AR) of the two CLSMs are dependent on the wavelength of the laser and the numerical apertures (N. A.) of the objective lens. For LSM 5 Pascal CLSM, an objective lens of 20X magnification with N.A. of 0.5 was used, giving lateral and axial resolutions are 0.69 μm and 1.95 μm, respectively. For the LSM 210 CLSM, the following objectives lenses were

used: 5X (N.A. = 0.15, LR = 1.98 µm, AR = 21.7 µm), 10X (N.A. = 0.30, LR = 0.99 µm, AR = 5.42 µm), 20X (N.A. = 0.50, LR = 0.60 µm, AR = 1.95 µm), and 50X (N.A. = 0.50, LR = 0.60 µm, AR = 1.95 µm).

The specimen size that can be accommodated in CLSM is very flexible. The specimen stage of LSM 210 is 90 mm x 60 mm and the maximum distance between the stage and the objective lens is 30 mm, while the stage of LSM 5 Pascal is 80 mm x 60 mm large and the maximum distance between the stage and the objective is 20 mm. Since there are no impediments at the sides of the CLSM specimen stage, the CLSM could easily accommodate specimens with larger lateral dimensions that the stage dimensions, for example specimens on the order to 20 mm to 30 mm thick and 100 mm in each lateral dimension could easily be accommodated, which is a considerably larger specimen that can be placed in most SEM sample chambers. Furthermore, the CSLM stages can be replaced with modified stages or removed entirely in order to accommodate even larger specimens.

Scanning electron microscope comparison

A series of Scanning Electron Microscope (SEM) images were taken of several selected areas on the HA specimens that coincided with CLSM images using a JEOL 6400V SEM (JEOL Corporation, Japan) operated at an accelerating potential of 2 keV. The specimens viewed in the SEM were sputter coated with an approximately 21 nm layer of Au using a SC500 sputter coater (Emscope Laboratories, Ltd. Ashford, England).

RESULTS AND DISCUSSION

Using a variety of fluorescing labeling agents, CLSM has been used to image the morphology and focal adhesions of human osteoblast cells on HA [34], TiO_2/HA [35] and PMMA cement [36], locate focal cell adhesions of osteoblasts on HAPEX (HA in HDPE) [36, 37], HA microspheres [34], assess the effect of surface topography on osteoblast attachment for composites of HAPEX and AWPEX (a glass-ceramic apatite-wollastonite in HDPE) [38] and estimate the degree of bone ingrowth [39] on dense hydroxyapatite implants. In a related study, [40] a CSLM was used to investigate the interconnected nature of the defects arising in plasma sprayed hydroxyapatite coatings after immersion in simulated body fluid as a function of time. An SEM was used to detect the presence of cracks and pores but could not distinguish the degree of interconnectivity. The CSLM however was able to detect an interconnected defect network in the plasma sprayed HA coating.

However, while each of these studies demonstrates the usefulness of CSLM to image morphological aspects of HA-cell interactions, to date, there is little research examining the pore size and pore size distribution, including the degree of pore interconnectedness, which has been linked to improvements in neobone formation and ingrowth into 3D HA bioceramic scaffolds.

In this study, we employ two CLSM operational modes, namely the (i) confocal reflection mode and (ii) the confocal fluorescence mode. The reflection mode and the fluorescence mode allow different types of CLSM

images to be collected, that is, while the reflection mode is best suited for imaging the surface profile of rough or porous surfaces, the fluorescence mode allows one to highlight specific subsurface features by adding fluorescent tracers.

For example, the CLSM confocal reflection was used by Draeger and Case [41-43] to image surface channels about 500 to 900 μm in diameter in partially stabilized zirconia (PSZ) specimens. (Surface channels can be converted into bulk-penetrating channels by ceramic/ceramic joining [44-46] and such channels can in turn be used to transfer a variety of fluids including cooling fluids for electronic substrates [47].) For the surface channels in the PSZ specimens [41-43] it was essential to characterize the details of both the meso-scale channels dimensions and shape as well as the micron-scale topography of the channel surface since both (i) the meso-scale size and shape of the channel and (ii) the micron-scale projections on channel walls influence fluid flow and heat transfer in the channels. The ability of the CLSM to image meso-scale objects (the channels in the PSZ specimens or the macropores in the bone scaffolds) as well as micron-scale objects (pores and surface roughness on the walls of the PSZ channels and the pores in the bone scaffolds) is thus vital to characterizing ceramic components whose function depends simultaneously on structures at the meso and micro scale.

The interest in the flow and storage of liquids and of gases in rocks has led the geological community to employ the CLSM operated in fluorescence mode to characterize three-dimensional porosity in geological materials [8, 48-

[51]. As in this study, a porous specimen is impregnated with a low viscosity epoxy that contains a fluorescent stain. Since rocks and ceramics do not fluoresce, the stain can then help to delineate subsurface porosity when illuminated by the CLSM.

There are both important differences and similarities between the details of the pore architecture for rocks and bone scaffolds. The porosity in sedimentary rocks can range from roughly 20 volume percent for some sandstones to about 60 volume percent for diatomaceous rock [8], while the volume percent porosity of the bone scaffold specimens examined here is between about 60 and 70. In addition, the pore architecture for some geological materials is generally analogous to that observed for ceramics densified from powder compacts. For example, geologists refer to "nodal" pores at triple-grain junctions and label as "throats" the interconnecting pores (which are sometimes "sheet-like") that run along the grain edges [48]. This type of pore geometry is consistent with the general pore architecture described by German [52] for sintered powder compacts, although instead of the "sheet" shaped pores that connect nodal pores in geological materials, tubular pores tend to connect pores at triple grain junctions in sintered powder compacts [52].

In sandstones, the mean pore size is typically 25 to 40 μm, with a relatively small fraction of pores being as large as 100 to 250 μm [48], while in the bone scaffolds there is a macropore phase (pores having diameters of 200 μm and larger) and a "micropore" phase of interconnecting pores of diameter 60-70 μm. Thus, the successful use of CLSM for characterizing

subsurface porosity in geological materials [8, 48] indicates that these methods should be applicable to ceramic bone scaffolding materials. In this paper, we have begun the process of modifying and optimizing the geologists' procedures to accommodate the differences in porosity and surface structure characteristic of ceramic bone scaffold materials.

CLSM characterization of HA ceramic bone scaffold specimens

Each of the specimens described in this study (Figures 1 - 5) have been sectioned by a low speed diamond saw prior to observation by either the CLSM (all Figures except 4a) or a conventional SEM (Figure 4b). For the specimen shown in Figure 3, the specimen was first impregnated with epoxy and then sectioned while all of the other specimens depicted here were sectioned and observed without epoxy impregnation. This sectioning accounts for the "flat" profile that is observed at the highest points on each specimen.

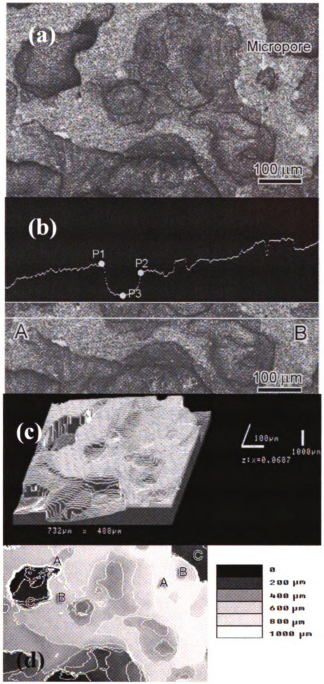

Fig. 1: A series of four reflection-mode confocal laser scanning microscopy images taken at a single location on hydroxyapatite (HA) specimen HA-70-AS-1: (a) an overlay image showing both macropores (B150–300 mm) and micropores (B60–70 mm), (b) a Phi-Z scan along "cut line" A–B, with pore dimensions labeled directly on the profile, (c) a "wire mesh" topographic three dimensional profile highlighting the larger surface features of the specimen while supressing the fine surface detail, and (d) a contour map that uses a gray scale to indicate depth relative to a basal plane.

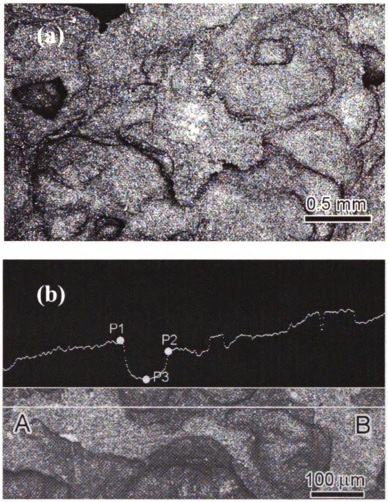

Fig. 2: A series of reflection-mode confocal laser scanning microscopy images of specimen HA-70-AS-2, taken at a single location on the specimen: (a) an overlay image, (b) a Phi-Z scan

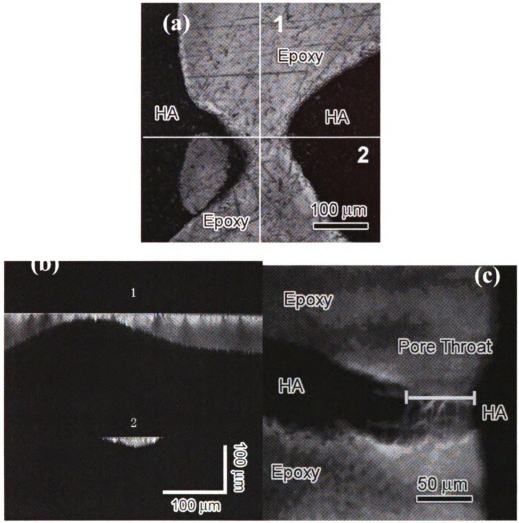

Fig. 3: For a single location on the epoxy-impregnated and stained specimen HA-70-ES-1, a series of fluorescent-mode confocal laser scanning microscopy images: (a) an overlay image, (b) a Phi-Z profiles along the cuts "1" and cut "2," where the bright regions correspond to the stained epoxy that fluoresces and the dark regions hydroxyapatite (HA), which does not fluoresce, and (c) a single z section image taken at a depth of about 40 mm beneath the specimen surface. A pore throat (opening between two adjacent pores) is labeled on the image.

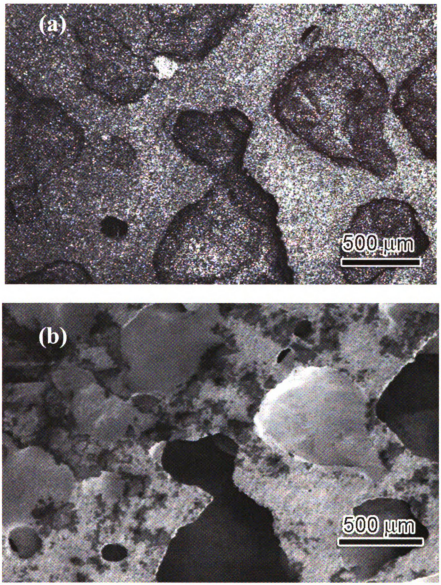

Fig. 4: A comparison between (a) an overlay confocal laser scanning microscopy (CLSM) image and (b) a conventional scanning electron microscoope (SEM) image taken at the same location with identical magnification. Although the SEM image has higher lateral resolution than the CLSM image, the SEM is unable to simultaneously image the specimen surface and within the pores because of the limited depth of field of the SEM.

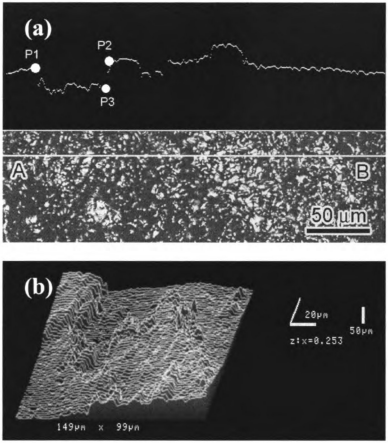

Fig. 5: A series of reflection-mode confocal laser scanning microscopy (CLSM) images of specimen HA-70-AS-2 taken with a higher lateral and vertical resolution than the CLSM images in Figs. 1–5, including a: (a) Phi-Z scan and (b) topographical profile. All images were taken at the same location on the specimen.

HA-70-AS-1, an as-sectioned (not epoxy impregnated and unstained) hydroxyapatite specimen with about 70 volume percent porosity, was observed using a Zeiss 210 CLSM operated in the confocal reflection mode. Figure 1a shows an overlay image from a "100 z-sectioning series", meaning that the image has been electronically constructed from 100 individual confocal images. The total image depth is 1200 µm and the "thickness" of each section in the image stack is 12 µm, that is, as the images were collected by the CLSM computer, the focal plane was shifted up by 12 µm

after each image was collected. Specimen HA-70-AS-1 includes macropores with diameters of roughly 150 to 300 μm (Figure 1a), which is within the size range of micropores that is typical of bone scaffold materials. In addition, Figure 1a shows a portion of a micropore about 60 μm in diameter. (As discussed in Section 2.1, the bone tissue engineering community uses the term "micropore" to describe pores with diameters of about 60 to 70 μm that serve as connecting pathways for nutrient flow and bone ingrowth).The details of the topography of an overlay image (Figure 1a) can be analyzed via a "phi-Z' scan (Figure 1b), a topographical map (Figure 1c) and a contour map (Figure 1d). A phi-Z scan (Figure 1b) represents a top surface profile along an operator-selected line within the field of view of the CLSM image. For example, the lower half of the image in Figure 1b shows Line A-B placed across a portion of the image shown in Figure 1a. The upper half of Figure 1b presents the geometric profile of the specimen along the "cutting" line A-B. Once the profile has been obtained, the CLSM software allows one to measure vertical heights between any two points along the specimen profile. For the pore shown in the phi-Z profile (Figure 1b), the horizontal distance between points P1 and P2 is 104 μm and the vertical distance between points P1 and P3 is 148 μm. Thus, the phi-Z scan allows one to select particular features of interest and then to determine their dimensions.

Figure 1c gives a three-dimensional topographic profile for specimen HA-70-AS-1 that corresponds to the overlay image presented in Figure 1a. After an overlay image has been collected, a topographic profile image as well as

contour images (Figure 1d) and an arbitrary number of phi-Z scans (such as Figure 1b) can be constructed electronically from the overlay image. Phi-Z, contour and topographical images also can be constructed from overlay images and can be collected independently.

The topographic image has two advantages over the overlay images. First, the topographic map's "wire mesh image" shows clearly the overall surface profile of a specimen by suppressing the information on the specimen's fine surface features. A second advantage of the topographic map is that one can choose to collect the topographical map separate from an overlay image, since the topographical map itself takes far less time to accumulate than a complete overlay image. For example, whereas for an overlay image that takes 10 minutes to accumulate, a comparable topographical image can be obtained in perhaps five minutes or less. Thus, one can more quickly and efficiently "survey" the topographical features using a series of topographical maps as opposed to a comparable series of overlay images. This implies that the CLSM could efficiently gather topographical information from specimens of realistic dimensions for medical practice, where ceramic bone scaffold dimensions can range from roughly a few millimeters to several centimeters depending on the relative size of the bone in which the defect occurs. Of course, the overlay image (such as Figure 1a) has the advantage of displaying far greater detail in the image than does the topographical profile.

A contour map for specimen HA-70-AS-1 (corresponding to the overlay image in Figure 1a) uses a gray scale to indicate depth and contour lines to indicate "levels" of constant depth. (Although it is shown as a gray scale here, the contour maps prepared by the CLSM's computer are rendered in color.) In Figure 1d, there is a height difference of 200 μm between adjacent contour lines. The labels "A", "B" and "C" in Figure 1d denote depths of 1000 μm, 600 μm, and 200 μm, respectively above the lowest point in the image (designated as a height of zero). The contour map's information thus complements that given by the overlay, phi-z and topographical images.

Figure 2, which was obtained using the Zeiss 210 CLSM in the confocal reflection mode, shows specimen HA-70-AS-2 (as-sectioned specimen with a 70 volume percent porosity). Figure 2 is an overlay image consisting of a 100-z section series with total depth of 2 mm and a thickness of 2.0 μm for each section. While the overlay image (Figure 2a) depicts the details of the specimen surface, the phi-Z scan (Figure 2b) again helps us to understand the three-dimensional nature of the surface. Figure 2b shows (for the cut A-B across the overlay image), a steep-sided ridge 1325 μm tall (Point P1 to P2 in Figure 2b) and 363 μm wide (point P2 to P3 in Figure 2b) that separates two pore regions with relatively flat or gently sloping bottoms.

Specimen HA-70-ES-1, an epoxy impregnated, Rhodamine B stained hydroxyapatite specimen with approximately 70 volume percent porosity was imaged using the Zeiss Pascal 510 CLSM in the confocal fluorescence mode (Figure 3). Figure 3a is a 100-section overlay image with a thickness of 1.0

μm for each section and total image depth of 100 μm. In Figure 3a, the two lines that intersect at right angles (labeled at "1" and "2") mark the position of two phi-z cuts on the image, the projections of which are shown in Figure 3b. The two profiles depict the thickness and shape of a thin bridge of epoxy, where the profile along cut 1 shows an arching section of epoxy that varies from about 90 μm down to about 15 μm in the vertical direction (Figure 3b). In contrast, the bridging section along cut 2 is only about 80 μm long with a maximum thickness of about 20μm.

Figure 3c is an image in the fluorescence mode taken at a depth about 40 μm below the specimen surface. Figure 3c depicts a "pore throat", an opening between two pores, which is about 30 μm across at its narrowest point. The use of the CLSM fluorescence mode to image subsurface features will likely prove to be extremely important to the development of a process to characterize the three-dimensional nature of bone scaffolds, in a manner analogous to the analysis done for the interconnected porosity in geological materials [8, 48, 49].

The pair of images given in Figures 4a and 4b provides a direct comparison between a CLSM overlay image (Figure 4a) and a conventional SEM (Figure 4b) micrograph of a sintered 70 volume percent HA specimen (HA-70-AS-3). In order to facilitate comparison, the two micrographs (Figures 4a and 4b) depict the same location on the specimen surface and were taken at the same magnification. While the SEM micrograph portrays well the details of the uppermost portion of the specimen surface of the specimen,

there is no information from within the pores due to the limited depth of field of the SEM. In contrast, the upper surface as well as the bottoms and side walls of the pores are in focus in the CLSM overlay image. To further determine the details of the surface topology, one could use the phi-Z scans, topographical maps or contour maps, as discussed for Figure 1.

Figure 5a and 5b demonstrate the use of the CLSM reflection mode to examine micron-scale features on the bone scaffold surfaces. The phi-Z scan (top section of Figure 5a) corresponding to surface shown (bottom section of Figure 5a) shows surface roughness on the scale of several microns. For example, the larger surface features in Figure 5a are on the scale of tens of microns, where the horizontal distance from P1 to P2 is 27.6 μm and the vertical distance from point P1 to P2 is 31.8 μm.

SUMMARY AND CONCLUSIONS

The development of ceramic bone scaffold materials depends on developing methods to characterize the microstructure of the ceramic scaffolds. These ceramic materials represent a cost of approximately $2.5 billion annually in the United States alone [7]. When combined with the market in craniofacial and other orthopaedic applications such as the total hip replacement, bioceramics represent an increasingly popular choice for biomedical applications. Confocal Laser Scanning Microscopy is a tool that is well suited to characterizing important macro- and micro- scale features in bone scaffolds and has the potential to receive wide spread use

characterizing other bioceramic materials such as alumina, zirconia and Bioglass™.

While the CLSM reflection mode is well suited to characterize the 200 to 1000 μm diameter surface-breaking pores in HA bone scaffolds, the fluorescence mode is very powerful since it can image subsurface features. This study has begun the process of adjusting the CLSM procedures developed by geologists [8, 48, 49] for materials with a smaller average pore size (about 25 to 40 μm on average). As work on these procedures progress, the observation technique for subsurface features will be further refined, and then complex statistical analysis can be applied to the CLSM images to fully characterize the three-dimensional pore architecture of bone scaffolds.

ACKNOWLEDGEMENTS

The authors acknowledge the use of the Confocal Laser Scanning Microscope and SEM facilities at the Advanced Microscopy Center, Michigan State University along with the assistance of Dr. Shirley Owens and Dr. Joanne Whallon.

REFERENCES

1. H. Feng, Y. Zeng, M. Graner, and E. Katsanis, "Stressed apoptotic tumor cells stimulate dendritic cells and induce specific cytotoxic T cells," Blood **100**(2), 4108-4115 (2002).

2. P. Kolenbrander, R. Andersen, D. Blehert, P. Egland, J. Foster, and R. Palmer, "Communication among oral bacteria," Microbiol Mol Biol Rev **66**(3), 486-505 (2002).

3. P. Day, R. Roden, D. Lowy, and J. Schiller, "The papillomavirus minor capsid protein, L2, induces localization of the major capsid protein, L1, and the viral transcription/replication protein, E2, to PML oncogenic domains," J Virol **72**(1), 142-150 (1998).

4. B. Trapp, J. Peterson, R. Ransohoff, R. Rudick, S. Mork, and L. B. L, "Axonal transection in the lesions of multiple sclerosis," N Engl J Med **338**(5), 278-285 (1998).

5. L. Li, P. Lorenzo, K. Bogi, P. Blumberg, and S. Yuspa, "Protein kinase C delta targets mitochondria, alters mitochondrial membrane potential, and induces apoptosis in normal and neoplastic keratinocytes when overexpressed by an adenoviral vector," Mol Cell Biol **19**(12), 8547-8558 (1999).

6. J. Jester, P. Barry, G. Lind, W. Petroll, R. Garana, and H. Cavanagh, "Corneal keratocytes - in situ and in-vitro organization of cytoskeletal contractile proteins," Invest Ophthalmol Vis Sci **35**(2), 730-743 (1994).

7. C. T. Laurencin and Y. Khan, "Bone graft substitute materials" (eMedicine.com, Inc., 2004), retrieved 2004, http://www.emedicine.com/orthoped/topic611.htm.

8. J. Fredrich, "3D imaging of porous media using laser scanning confocal microscopy with application to microscale transport processes," Phys. Chem. Earth Pt. A-Solid Earth Geod. **24**, 551-561 (1999).

9. W. Lu, F. Zhao, K. Luk, Y. Yin, K. Cheung, G. Cheng, K. Yao, and J. JCY Leong, "Controllable porosity hydroxyapatite ceramics as spine cage: fabrication and properties evaluation," J Mater Sci: Mater in Med **14**(12), 1039 - 1046 (2003).

10. A. Queiroz, S. Teixeira, J. Santos, and F. Monteiro, "Production of porus hydroxyapatite with potential for controlled drug delivery," Mater Sci Forum **455-456**, 358 - 360 (2004).

11. K. Hing, S. Saeed, B. Annaz, T. Buckland, and P. Revell, "Microporosity affects bioactivity of macroporous hydroxyapatite bone graft substitutes," Key Eng Mat **254**(2), 273 - 276 (2004).

12. K. Hing, S. Best, K. Tanner, W. Bonfield, and P. Revell, "Mediation of bone ingrowth in porous hydroxyapatite bone graft substitutes," J Biomed Mater Res **68**(1), 187-200 (2004).

13. G. Babini and A. Tampieri, "Towards biologically inspired materials," Brit Ceram Trans **103**(3), 101-109 (2004).

14. M. Hasegawa, A. Sudo, V. Komlev, S. Barinov, and A. Uchida, "High release of antibiotic from a novel hydroxyapatite with bimodal pore size distribution," J Biomed Mater Res **70**(2), 332-339 (2004).

15. L. Nielsen, "Elasticity and damping of porous materials and impregnated materials," J Am Ceram Soc **67**, 93-98 (1983).

16. L. Nielsen, "Strength and stiffness of porous materials," J Am Ceram Soc **73**, 2684-2689 (1990).

17. S. Nanjangud, R. Brezny, and D. J. Green, "Strength and young's modulus behavior of a partially sintered porous alumina," J Am Ceram Soc **78**, 266-268 (1995).

18. A. Ravaglioli and A. Krajewski, *Bioceramics. materials, properties, applications* (Chapman and Hall, London, 1992).

19. D. Lam, F. Lange, and A. Evans, "Mechanical properties of partially dense alumina produced from powder compacts," J Am Ceram Soc **77**, 2113-2117 (1994).

20. T. P. Hoepfner and E. D. Case, "The influence of the microstructure on the hardness of sintered hydroxyapatite," Ceram Intl **29**(6), 699-706 (2003).

21. E. Ryshkewitch, "Compression strength of porous sintered alumina and zirconia," J Am Ceram Soc **36**, 65-68 (1953).

22. D. Hardy and D. J. Green, "Mechanical properties of a partially sintered alumina," J Eur Ceram Soc **15**, 769-775 (1995).

23. D. J. Green and D. Hardy, "Fracture toughness of partially-sintered brittle materials," Mat Sci Lett **15**(13), 1167-1168 (1996).

24. K. deGroot, "Effect of porosity and physicochemical properties on the stability, resorption and strength of calcium phosphate ceramics," in *Bioceramics: Material characteristic versus in vivo behavior*, J. E. Lemons, ed. (New York, 1988), pp. 227-234.

25. K. Hing, S. Best, K. Tanner, W. Bonfield, and P. Revell, "Quantification of bone ingrowth within bone-derived porous hydroxyapatite implants of varying density," J Mater Sci: Mater Med **10**, 663-670 (1999).

26. F. Bodic, Y. Amouriq, O. Gauthier, M. Gayet-Delacroix, J. M. Bouler, G. Daclusi, and L. Hamel, "Computed tomography assessment of alveolar filling with an injectable bone substitute," J Mater Sci: Mater Med **13**, 953-958 (2002).

27. S. Nagaraja, T. L. Couse, and R. E. Guldberg, "Trabecular bone microdamage and microstructural stresses under uniaxial compression," J Biomech **38**, 707-716 (2005).

28. S. Ikeda, Y. Morishita, H. Tsutsumi, M. Ito, A. Shiraishi, S. Arita, S. Akahoshi, K. Narusawa, and T. Nakamura, "Reductions in bone turnover, mineral, and structure associated with mechanical properties of lumbar vertebra and femur in glucocorticoid-treated growing minipigs," Bone **33**, 779-787 (2003).

29. P. Weiss, L. Obadia, D. Magne, X. Bourges, C. Rau, T. Weitkamp, I. Khairoun, J. M. Bouler, D. Chappard, O. Gauthier, and G. Daclusi, "Synchrotron X-ray microtomography (on a micron scale) provides three-dimensional imaging representation of bone ingrowth in calcium phosphate biomaterials," Biomaterials **24**, 4591-4601 (2003).

30. Z. Liu, "Confocal laser scanning microscopy - an attractive tool for studying the uptake of xenobiotics into plant foliage," J Microscopy - Oxford **213**(Part 2), 87-93 (2004).

31. K. Sauermann, T. Gambichler, M. Wilmert, S. Rotterdam, M. Stucker, P. Altmeyer, and K. Hoffmann, "Investigation of basal cell carcionoma by confocal laser scanning in vivo," Skin Research and Technology **8**(3), 141-147 (2002).

32. M. Hudelmaier, A. Kollstedt, E. M. Lochmuller, V. Kuhn, F. Eckstein, and T. M. Link, "Gender differences in trabecular bone architecture of the distal radius assessed with magnetic resonance imaging and implications for mechanical competence," Osteoporosis Int **16**(9), 1124-1133 (2005).

33. R. A. McMullen, "An in vitro investigation of MC3T3-E1 osteoblast proliferation and differentiation on hydroxyapatite based tissue engineered scaffolds," M.S. (Michigan State University, East Lansing, 2004).

34. C. Barrias, C. Ribeiro, and M. Barbosa, "Adhesion and proliferation of human osteoblastic cells seeded on injectable hydroxyapatite microspheres," Key Eng Mat **254-256**, 877-880 (2004).

35. P. Ramires, A. Giuffrida, and E. Milella, "Three-dimensional reconstruction of confocal laser microscopy images to study the behaviour of osteoblastic cells grown on biomaterials," Biomaterials **23**, 397-406 (2002).

36. M. Dalby, L. DiSilvio, E. Harper, and W. Bonfield, "Increasing hydroxyapatite incorporation into poly(methylmethacrylate) cement increases osteoblast adhesion and response," Biomaterials **23**, 569-576 (2002).

37. M. Dalby, M. Kayser, W. Bonfield, and L. DiSilvio, "Initial attachment of osteoblasts to an optimized HAPEX topography," Biomaterials **23**, 681-690 (2002).

38. S. Rhea, R. Brooks, A. Schneider, S. Best, and W. Bonfield, "Osteoblast-like cell response to bioactive composites - surface-topography and composition effects," J. Biomed Mater Res: Appl Biomater **70B**, 250-261 (2004).

39. F. Takeshita, S. Iyama, Y. Ayukawa, H. Akedo, and T. Suetsugu, "Study of bone formation around dense hydroxyapatite implants using light microscopy, image processing and confocal laser scanning microscopy," Biomaterials **18**, 317-322 (1997).

40. K. Khor, M. E. Pons, G. Bertran, N. Llorca, M. Jeandin, and V. Guipont, "Confocal microscopy characterization of in vitro tests of controlled atmosphere plasma spraying hydroxyapatite (CAPS-HA) coatings," Key Eng Mat **254-256**, 319-322 (2004).

41. D. J. Draeger and E. D. Case, "The characterization of channels in zirconia ceramics using Laser Scanning Confocal Microscopy," J Mater Sci Lett **21**, 787-791 (2002).

42. D. J. Draeger and E. D. Case, "The modification of the surface topology of channels in fully stabilized zirconia, as observed using Laser Scanning Confocal Microscopy," Materials Letters **55**(1-2), 88-92 (2002).

43. D. J. Draeger and E. D. Case, "Engineering the surface texture and shape of channels in ceramic substrates," Mater Sci and Eng B **97**(1), 94-105 (2003).

44. H. Shin, E. Case, and P. Kwon, "Fabrication of internal channels in ceramics and ceramic composites," J Adv Mater **35**(2), 28-35 (2003).

45. E. D. Case, "Selection and function of interlayer materials in ceramic/ceramic joining," in *Ceramic Transactions*, R. Loehman, ed. (American Ceramic Society, Westerville OH, 2003), pp. 3-28.

46. L. Zeng, E. D. Case, and M. A. Crimp, "Effects of a silica spin-on interalyer and heating mode on the joining of zirconia and MaCor," Mat Sci and Eng **357**(1-2), 67–74 (2003).

47. E. D. Case, F. Ren, P. Kwon, C. K. Kok, R. Rachedi, and B. Klenow, "Machining and ceramic/ceramic joining to form internal meso-scale channels," Intl J Appl Ceram Tech **1**(1), 95-103 (2004).

48. J. Fredrich, K. Greaves, and J. Martin, "Pore geometry and transport properties of Fontainebleau sandstone," Int J Rock Mech Min Sci and Geomech Abstr **30**(7), 691-697 (1993).

49. N. Petford, G. Davidson, and J. Miller, "Investigation of the petrophysical properties of a porous sandstone sample using confocal scanning laser microscopy," Petrol Geosci **7**, 99-105 (2001).

50. M. Montoto, A. Martinez-Nistal, A. Rodriguez-Rey, N. Fernandez-Merayo, and P. Soriano, "Microfractography of granitic-rocks under confocal scanning laser microscopy," J Microscopy **177**, 138-149 (1995).

51. J. Pironon, M. Canals, J. Dubessy, F. Walgenwitz, and C. Laplace-Builhe, "Volumetric reconstruction of individual oil inclusions by confocal scanning laser micrscopy," Eur J Miner **10**(6), 1143-1150 (1998).

52. R. M. German, *Sintering theory and practice* (John Wiley and Sons, New York, 1996), pp. 99-101.

APPENDIX B

CONFOCAL LASER SCANNING MICROSCOPY (CLSM) AS A TOOL FOR IMAGING CANCELLOUS BONE

I.O. SMITH, F. REN, M.J. BAUMANN AND E.D. CASE
Department of Chemical Engineering and Materials Science, Michigan State University, East Lansing, MI, USA 48824

PUBLISHED IN: Journal of Biomedical Materials Research Part B. 2006;79:185-192.

ABSTRACT

Understanding the bimodal structure of cancellous bone is important for tissue engineering in order to more accurately fabricate scaffolds to promote bone ingrowth and vascularization in newly forming bone. In this study, confocal laser scanning microscopy (CLSM) was used to create detailed images of the bimodally porous intertrabecular space of defatted and deproteinized cancellous canine bone taken from the epiphysis of the humerus. The bimodal pore structure was imaged using both reflective and fluorescent modes in CLSM, resulting in four different, but complementary image types: 1) a Z-stack overlay, 2) a phi-Z scan, 3) a topographical map and 4) a contour map. Submerging the bone in Rhodamine B dye prior to fluorescent imaging enhanced the pore surface details giving a more accurate pore size measurement. The average macropore diameter was found to be 260 μm ± 97 μm while the average micropore diameter was 13 μm ± 10 μm. When compared to common techniques for imaging cancellous bone, including micro computed tomography (μCT), magnetic resonance imaging

(MRI), scanning electron microscopy (SEM) and environmental scanning electron microscopy (ESEM), CLSM was found to be an effective tool, given its ability to non-destructively image the surface and near-surface pore structure.

INTRODUCTION

This study is an extension of a series by the authors on bone and engineered bone tissue materials, including the role of hydroxyapatite (HA) surfaces in the regulation of osteoblast (OB) gene expression and phenotype,[1] electrostatic interactions of biomaterials with OBs and whole bone,[2] the electrostatic attraction between OBs and calcium deficient apatites and OBs and biphasic calcium phosphate[3] and the effect of HA on differentiation and growth of MC3T3-E1 OBs[4]. Additionally, the authors' recent work includes studies of the dependence of the hardness[5] and dielectric constant[6] on volume fraction porosity of HA, as well as studies of microcracking,[7,8] biaxial flexure strength[9] and ceramic/ceramic joining by both microwave and conventional sintering.[10-14] Recently, the authors were among the first to apply Confocal Laser Scanning Microscopy (CLSM) to the study of porosity in HA specimens,[15] based in part on studies on the morphology of surface channels in zirconia ceramics.[16-18]

The hypothesis of this study is that CLSM may be used to image surface and near-surface features in cancellous bone, including macro- and micropores. Three-dimensional representative images of cancellous canine bone were created using stacks of individual confocal images (Z-stacks) and

both reflective and fluorescent modes in CLSM. These methods created detailed images of the surface and near-surface structure of the macro- and micropores, using a combination of Z-stack overlays, phi-Z scans, as well as topographical and contour mapping. CLSM's high resolution (2 μm) and high depth of field (~2 mm) makes it suitable to image both the large scale macropores and the finer interconnective micropores of cancellous bone. Imaging is enhanced by fluorescent CLSM Z-stack overlay which also increased the accuracy of pore size measurements, showing macropores having an average diameter of 260 μm ± 97 μm and micropores having an average diameter of 13 μm ± 10 μm. Three-dimensional images obtained in this study give a better understanding of the bimodal pore structure of cancellous bone, which is an essential part of more effectively designing bone tissue engineering scaffolds.

BACKGROUND

Bone Structure

The structural elements of bone are divided into two types: cortical and cancellous tissue.[19] Cortical (compact) bone has a higher compressive strength (69-110MPa)[20] than cancellous (spongy) bone and is more abundant in load-bearing bones, such as the femur.[21]

Cortical bone consists of nanocrystals of apatite, which has a composition similar to HA,[22,23] and collagen fibrils arranged in thin, concentrically layered lamellar sheets. These are grouped around central

Haversian canals, which provide a pathway for blood vessels and nerve fibers.[19,21] Each grouping is referred to as an osteon or Haversian system.[21] Within individual lamellae are interconnected spaces called lacunae, which contain osteocytes that traverse each Haversian system, supplying nutrients to the entire structure.[19,21]

Cancellous (spongy) bone has a greater volume fraction porosity than cortical bone[19] with an open microstructure of trabeculae intermingled with bone marrow.[21] These trabeculae consist of lamellae, but do not form osteons. Rather, nutrients are exchanged with the surrounding bone marrow via lacunae contained within the trabecular lamellae.[21] In long bones, cancellous tissue is found primarily in the epiphysis and along the outer surface of the medullary cavity.[21]

The bimodal porosity of cancellous bone tissue is an important factor in its effective vascularization and for bone ingrowth. Microporosity is essential during the initial stages of osseointegration, with increased microporosity causing increased bone ingrowth.[24]

Imaging porous structures using CLSM

Geologists use CLSM to image subsurface pore structures in rock where it is difficult to image such features without physically removing a surface layer, thereby damaging the specimen. These subsurface details are crucial, for example in water or oil flow in porous rock. CLSM has successfully characterized the subsurface pore size, shape and interconnectivity,[25-28] as

well as microcracking,[29] in a wide range of geological materials by impregnating porous specimens with a low viscosity epoxy containing a fluorescent stain.[26,27]

Visualizing the detailed shape of pores, including subsurface pore structures, is also important when designing bone tissue engineered scaffolds. Non-destructive sectioning of a solid specimen followed by reconstruction of a detailed three-dimensional image of the pore structure is beneficial in understanding and in turn mimicking the three-dimensional nature of bone.

Recently, a modified version of the technique described above by Fredrich et al.[26] and Petford et al.[27] has been used to image porous HA scaffolds having a pore geometry similar to that of cancellous bone.[15] While this technique provided some detailed structural images, it must be further refined before it can be used to effectively assess the complete subsurface pore structure. Ren et al. were more successful in imaging the scaffold structure by using the reflective mode of CLSM to image surface and near-surface pores.[15] The larger-scale bimodal pore structure of cancellous bone is similar to the pore structure of the HA scaffolds viewed by Ren et al., therefore similar CLSM techniques could be used.

Electron microscopy for imaging bone

Transmission electron microscopy (TEM) is commonly used to image the micron and submicron features of bone, including cell structure,

organelles, extracellular matrix and submicron structural elements,[21,30] as well as the bone-implant interface, studying the remodeling process between HA and adjacent bone.[31-34] While TEM gives microstructural detail on the order of a micron or smaller, it is not an effective tool to image the larger scale pore structure in bone. Scanning electron microscopy (SEM) and CLSM are better suited for imaging surface and subsurface pore structures because of their lower magnification and greater depth of field.

Bone structures imaged using SEM include cancellous bone in human proximal femora,[35] cancellous bone in the human lumber spine,[36] the fracture surface of bovine subchondral bone[37] and rat vertebrae.[38] While the SEM gives submicron resolution (3-6 nm best case), it is limited by its depth of field (<<1 μm at high magnification) along with its inability to image subsurface features.[39]

MATERIALS AND METHODS

Sample preparation

A canine humerus, obtained from an animal sacrificed for reasons unrelated to the current study, was stored at -20°C for approximately two weeks prior to removal of muscle and skin tissue. Exposed bone was refrozen and sectioned transversely across the epiphysis using a low speed diamond-wafering blade at 200 rpm, revealing the trabeculae within the bone. A second cut was then made, parallel to the first, leaving a slice of bone approximately 10-mm thick. The rough sectioning used to obtain these

specimens did not adversely damage the specimen pore structure, as the saw kerf is negligible when compared to the specimen size. Using a scalpel, the periosteum and loose marrow were then carefully removed and the slice sectioned into 8 to 10, 10-mm wide pieces, each including regions of cortical and cancellous bone. Each piece was then defatted and deproteinized following a procedure devised by Johnson et al.[40] Dry samples of defatted and deproteinized bone were stored in a petri dish until CLSM imaging.

Two specimens were reserved for fluorescent staining. One specimen was globally stained by immersion in Rhodamine B solution for 12 hours. The staining of a second specimen was localized by injection with Rhodamine B at three pore openings along its surface, where only a small amount of dye (10 μl) was used to avoid spreading beyond the single pore.

CLSM Imaging

Two CLSM units were used in this study. One was better suited for topographical studies in the reflection mode and the second better suited for fluorescent mode. The CLSM unit used in reflection mode* used an Ar 488 nm laser for maximum resolution. An optical filter was not utilized; instead computer program filters (low pass filter and median pass filter) reduced the noise to signal ratio.

* Zeiss 210 CLSM (Carl-Zeiss Inc. Jena, Germany)

The CLSM unit used in fluorescent mode** was operated using a 488 nm Ar laser. Images were taken with a long pass filter (LP560) and a line average of 4 to reduce noise. In both cases, 1 to 2-mm thick sections of bone were optically sectioned into 50 or 100 slices (with thickness of ~10 μm) using CLSM.

SEM Imaging

Images of the bone from SEM were used for comparison purposes. Specimens were mounted onto aluminum stubs, gold-coated (21 nm thick) using a sputter coater and imaged at an accelerating voltage of 5 keV. SEM image was also compared to CLSM image by measuring pore size using phase-contrast imaging software.***

RESULTS

Reflection Mode

Reflective CLSM images of the defatted and deproteinized bone surface show near-surface features (Fig. 1), including both macro- and micropores. Images collected include Z-stack overlay (Fig. 1a), a single phi-Z scan across the specimen surface (Fig. 1b), a topographical map comprised of several phi-Z scans (Fig. 1c) and a contour map of the same surface, showing a maximum depth of ~1.2 mm (Fig. 1d).

** Zeiss LSM 5 Pascal CLSM (Carl-Zeiss Inc. Jena, Germany)
*** AnalySIS v.3.2 (Soft Imaging System GmbH, Lakewood, CO)

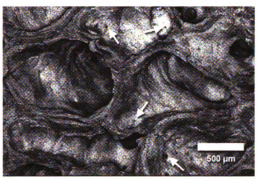

Figure 1a

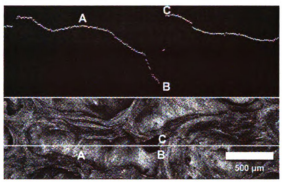

Figure 1b

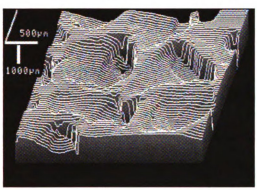

Figure 1c

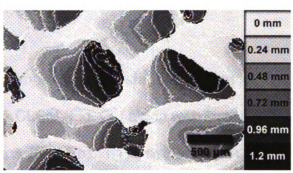

Figure 1d

Figure 1: Four images taken at a single location on cancellous bone specimen, including (Fig. 1a) a Z-stack overlay image showing macropores and interconnecting micropores (indicated with arrows), (Fig. 1b) a Phi-Z scan cross-sectional cut taken along the line shown, with A-B-C shown in the upper portion indicating the features of a pore (A-B-C on the lower portion), and C-B equal to 1.2 mm, (Fig. 1c) topographical map consisting of a wire mesh of consecutive Phi-Z cuts and (Fig. 1d) a contour map showing pore morphology and depth.

The topographical map and the contour map are different than, but complimentary to the Z-stack overlay image (Fig. 1). Contour mapping provides a reference for the shape, local curvature and depth of each macropore present. Topographical mapping builds three-dimensional images of surface features, giving the viewer a visual representation of the information contained in the contour map. When the topographical map and contour map are viewed together with the Z-stack overlay image, this combination is an intuitively useful representation of the specimen surface.

The surface area shown has several distinct macropores where each macropore has micropores along its walls, indicated with arrows (Fig. 1a). In Fig. 1b, the cross section of a macropore is indicated by A-B-C. The top-down view is shown in the lower half of the figure and the side view in the upper half. On the side view, the distance A-C is equal to 700 μm and the distance C-B is equal to 1.2 mm.

Topographical Fluorescence

One locally stained macropore, impregnated with Rhodamine B dye solution was imaged using fluorescent CLSM (Fig. 2a) along with finer details, including micropores, along its surface (Fig. 2b). This method was used to image only the pores impregnated with dye. Other non-impregnated pores could not be fluoresced.

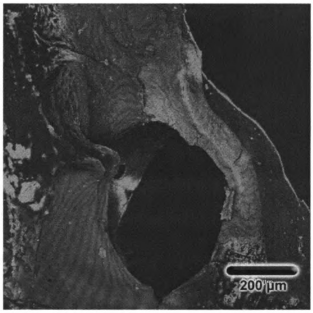

Figure 2a

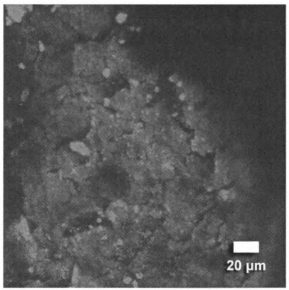

Figure 2b

Figure 2: Local staining of cancellous bone imaging (a) the interior of a single macro- and (b) micropores along the surface of a macropore.

A globally stained bone specimen was also imaged with fluorescent CLSM, revealing the bimodal pore structure (Fig. 3a). Further images (figures 3b and 3c) collected using this method were used to measure the average size of the macropores (260 μm ± 97 μm) and the micropores (13 μm ± 10 μm). The globally stained specimen was more effectively imaged in comparison to the locally stained specimen because the dye made it possible to image any region of the structure. This increased available field of view meant that the size of the pores could be more accurately measured.

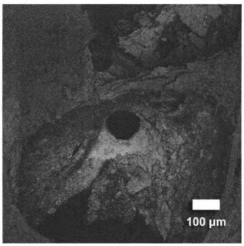

Figure 3a

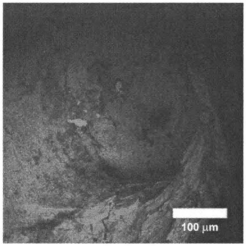

Figure 3b

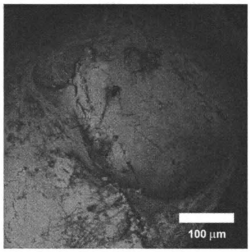

Figure 3c

Figure 3: CLSM reflectance images showing a single micropore on the surface of a macropore for globally stained cancellous bone. Figures 3b and 3c were used in measuring pore size.

SEM Comparison

The surface of defatted and deproteinized bone was imaged using both reflective CLSM (Fig. 4a) and SEM (Fig. 4b). Analysis of the SEM image yielded an average macropore size of 534.9 µm ± 265.9 µm and micropore size of 137.7 µm ± 50 µm. Analysis of the CLSM image yielded an average

macropore size of 506.0 μm ± 252.4 μm and micropore size of 106.6 μm ± 47.7 μm. Differences between reported values are possibly a result of the inability of SEM to image deep into the pores. The arrow shown on Figure 4a indicates a deep pore not clearly visible in Figure 4b. Actual location of these deep features can be ascertained using phi-Z scanning, topographical mapping and contour mapping (Figure 1b-1d).

Values reported in both cases are near those reported by deGroot (~200-400 μm and micropores <60 μm).[41] Compared to these established ranges, apparent differences in this case are likely a result of the inability of both techniques to effectively image smaller micropores, because of the relatively low magnification used.

While the SEM image effectively shows micron-scale details of the specimen surface, the sub-surface pore structure is not visible. The CLSM image (Fig. 4a) shows the pore interconnections while the corresponding SEM image (Fig. 4b) does not. Further, the pore depth cannot be assessed from SEM images. CLSM on the other hand, shows details from the surface to greater depths by combining individual CLSM image slices into Z-stacks greater than 1 mm in thickness.

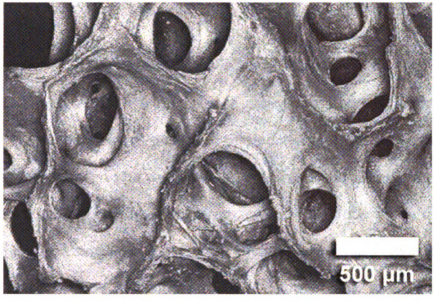

Figure 4a

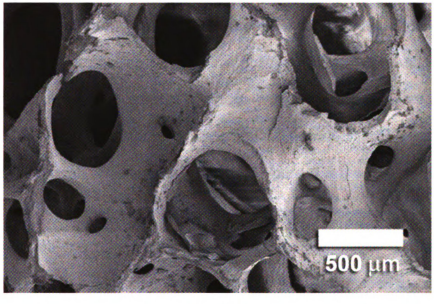

Figure 4b

Figure 4: A comparison between (a) CLSM image and (b) SEM image of the same section of defatted and deproteinized cancellous bone. Fig. 4a was taken using reflective CLSM, showing greater detail of pore depth, while Fig. 4b highlights the limitations of SEM imaging because of lower depth of field.

DISCUSSION

Reflective CLSM techniques similar to those used by Ren et al.[15] successfully imaged surface features of cancellous bone. Surface images produced by stacking optical slices into three-dimensional Z-stacks have both a sufficient resolution and a depth of field that is sufficient to show details of the bone's bimodal porosity, including macro- and micropores. In particular, topographical and contour mapping (Fig. 1c and Fig. 1d) aid in visualization of the specimen surface including details of pore shape, size, depth and curvature of pore walls. Fluorescent CLSM of rhodamine dye impregnated bone further improved the quality of Z-stack overlay images of the near-surface bone structure. The improved contrast between fluorescing bone mineral and non-fluorescing empty pore space enhanced the image quality thus more accurate measurement of macro- and micropore size was possible.

CLSM images taken from globally stained bone are more versatile than locally stained bone. The images shown in Figure 2 are two of three locally stained pores on the specimen surface. When selecting a pore for imaging, these three are the only choices, ruling out the remainder of the surface pores. This makes it difficult to observe a true representation of the specimen surface, as each pore is unique. In contrast, globally stained specimens provide a larger number of pores for imaging. The images shown in Figure 3 are a sampling of dozens of surface-breaking pores on the specimen. This wider variety of available pores allows the viewer to see a better representation of the specimen surface. In essence, local staining requires

the viewer to choose pores of interest before observing them, while global staining allows the viewer to observe the entire surface when looking for regions of interest.

Common bone imaging techniques include micro computed tomography (μCT), magnetic resonance imaging (MRI) and SEM. μCT gives a three-dimensional image of porous structures with resolutions up to 5 μm using benchtop units[42-44] and approaching 1 μm using synchrotron radiation sources.[45] However, high-flux synchrotron radiation damages living tissue. Also, synchrotron sources are rare and beam time is not easily obtainable. CLSM on the other hand images specimens of living tissue, and has a resolution of ~2 μm.[15]

MRI resolves and images the larger features of cancellous bone (~100-200 μm), but is unsuitable for smaller features such as micropores (<60 μm).[46] Furthermore, current MRI techniques do not include the compositing of two-dimensional images into three dimensions and MRI units are a far more expensive option, with unit costs over $1 million, compared to ~$200,000 for a CLSM unit.

While SEM imaged the surface features of bone, those images did not include detailed features at depths possible with CLSM. Also, SEM does not image qualities of the pore structure, on the order of those shown by contour mapping (Fig. 1d). The lack of these abilities prevent accurate pore depth measurement in bone using SEM. Additionally, SEM specimens used in this

study were free of water, because of the high vacuum required. This requirement rules out imaging whole bone tissue or bone cells in future studies.[39] The additional requirement that surfaces of SEM specimens also be conductive requires that ceramic-containing materials be imaged using a low potential or by adding a conductive coating, further limiting the use of living tissue.[39] Environmental scanning electron microscopy (ESEM) images water-containing specimens, but still requires a partial vacuum of 1 – 3 kPa.[39] Both SEM and ESEM vacuum chambers also constrain the specimen size (<100 mm in most cases), while CLSM uses an open stage, which accommodates specimens up to 20-30 mm thick and >100 mm in length and width.[15]

CLSM is a high-resolution imaging tool, imaging details as small as 2 μm with high depth of field capability, and is capable of creating three-dimensional images of known dimensions. In this study, CLSM imaging resulted in detailed images of both macro- and micropores comprising the bimodally porous intertrabecular space of cancellous bone. In the design of bone replacement scaffolds, mimicking the bimodal pore structure promotes bone ingrowth and proper vascularization in newly forming bone. Imaging pore structures via CLSM and using the resulting Z-stack overlays, topographical maps and contour maps, which are a source of valuable structural data, helps the viewer to better understand this structure. Although we have successfully imaged pore structures in HA[15] and in cancellous bone (this study) via CLSM, we have not yet imaged the pore structure of cortical

bone using CLSM. However, the ordered structure of cortical bone is comparatively well understood.[19,21]

CONCLUSION

CLSM has a lower lateral resolution than SEM and a lateral resolution comparable to μCT. However, the lateral resolution of CLSM is sufficient for detailed imaging of both macro- and micropores in cancellous bone. Fluorescent CLSM further improves contrast of these images, increasing the accuracy of pore size measurement. Additionally, CLSM does not require special specimen preparation or conditions damaging to living specimens for operation, which makes it possible to image living cells and tissue, a prospect for future studies.

The authors acknowledge the invaluable assistance and resources provided by the Center for Advanced Microscopy at Michigan State University, especially that of Dr. Shirley Owens and Professor Emeritus Joanne Whallon. Additionally, the authors thank Stuart Kaltz, an undergraduate student, for his assistance in preparing the bone specimens.

REFERENCES

1. Xie J, Baumann MJ, McCabe LR. Osteoblasts respond to hydroxyapatite surfaces with immediate changes in gene expression. J Biomed Mater Res 2004;71A:108-117.

2. Smith IO, Baumann MJ, McCabe LR. Electrostatic interactions as a predictor for osteoblast attachment to biomaterials. J Biomed Mater Res 2004;70A:436-441.

3. Smith IO, Baumann MJ, Obadia L, Bouler JM. Surface potential and osteoblast attraction to calcium phosphate compounds is affected by selected alkaline hydrolysis processing. J Mater Sci: Mater Med 2004;15:841-846.

4. Shu R, McMullen R, Baumann MJ, McCabe LR. Hydroxyapatite accelerates differentiation and suppresses growth of MC3T3-E1 osteoblasts. J Biomed Mater Res 2003;67A:1196-1204.

5. Hoepfner TP, Case ED. The influence of the microstructure on the hardness of sintered hydroxyapatite. Ceram Int 2003;29:699-706.

6. Hoepfner TP, Case ED. The porosity dependence of the dielectric constant for sintered hydroxyapatite. J Biomed Mater Res 2002;60:643-650.

7. Case ED, Smith IO, Baumann MJ. Microcracking and porosity in calcium phosphates and the implications for bone tissue engineering. Mat Sci and Eng A 2005;390:246-254.

8. Hoepfner TP, Case ED. An estimate of the critical grain size for microcracks induced hydroxyapatite by thermal expansion anisotropy. Mater Lett 2004;58:489-492.

9. Meganck JA, Baumann MJ, Case ED, McCabe LR, Allar JN. Biaxial flexure testing of calcium phosphate bioceramics for use in tissue engineering. J Biomed Mater Res 2005;72A:115-126.

10. Case ED. in *Joining 2002: On Joining Ceramics, Glass and Metal, Deutsche Kermaische Gesellschaft, e.V.* 9-16 (Am Grott 7, Cologne, Germany, 2002).

11. Case ED, Crimp MA. Joining of ceramic materials using spin on interlayers. Adv Eng Mater 2001;3:395-399.

12. Case ED, Ren F, Kwon P, Kok C-K, Rachedi R, Klenow B. Machining and ceramic/ceramic joining to form internal meso-scale channels. Int J Appl Ceram Tech 2004;1:95-103.

13. Shin HW, Case ED, Kwon P. Fabrication of internal channels in ceramics and ceramic composites. J Adv Mater 2003;35:28-35.

14. Singh D, Gutiérrez-Mora F, de la Cinta Lorenzo-Martin M, Routbort JL, Case ED. Plastic deformation of hydroxyapatites and its application to joining. Int J Appl Ceram Tech 2005;2:247-266.

15. Ren F, Smith IO, Case ED, Baumann MJ. Three-dimensional microstructural characterization of porous hydroxyapatite using confocal laser scanning microscopy (CLSM). Int J Appl Ceram Tech 2005; 2:200 - 211.

16. Draeger DJ, Case ED. The characterization of channels in zirconia ceramics using laser scanning confocal microscopy. J Mater Sci Lett 2002;21:787-791.

17. Draeger DJ, Case ED. The modification of the surface topology of channels in fully stabilized zirconia, as observed using laser scanning confocal microscopy. Mater Lett 2002;55:88-92.

18. Draeger DJ, Case ED. Engineering the surface texture and shape of channels in ceramic substrates. Mater Sci Eng 2003;B97:94-105.

19. Bryan GJ. Skeletal Anatomy. New York: Churchill Livingstone; 1996. 249 p.

20. LeGeros RZ. Properties of osteoconductive biomaterials: Calcium phosphates. Clin Orthop 2002;395:81-98.

21. Young B, Heath JW. Wheater's Functional Histology. Edinburgh: Churchill Livingstone; 2000. 413 p.

22. Ruys AJ, Wei M, Sorrell CC, Dickson MR, Brandwood A, Milthorpe BK. Sintering effects on the strength of hydroxyapatite. Biomaterials 1995;16:409-415.

23. Royer A, Viguie JC, Heughbaert M, Heughbaert JC. Stoichiometry of hydroxyapatite: Influence on flexural strength. J Mater Sci: Mater Med 1993;4:76-82.

24. Hing K, Saeed S, Annaz B, Buckland T, Revell P. Microporosity affects bioactivity of macroporous hydroxyapatite bone graft substitutes. Key Eng Mat 2004;254:273-276.

25. Fredrich JT, Greaves KH, Martin JW. Pore geometry and transport properties of Fontainebleau sandstone. Int J Rock Mech Min 1993;30:691-697.

26. Fredrich JT. 3D imaging of porous media using laser scanning confocal microscopy with application to microscale transport processes. Phys Chem Earth Pt A 1999;24:551-561.

27. Petford N, Davidson G, Miller JA. Investigation of the petrophysical properties if a porous sandstone sample using confocal scanning laser microscopy. Petrol Geosci 2001;7:99-105.

28. Pironon J, Canals M, Dubessy J, Walgenwitz F, Laplace-Builhe C. Volumetric reconstruction of individual oil inclusions by confocal scanning laser microscopy. Eur J Mineral 1998;10:1143-1150.

29. Montoto M, Martinez-Nistal A, Rodriguez-Rey A, Fernandez-Merayo N, Soriano P. Microfractography of granitic-rocks under confocal scanning laser microscopy. J Microscopy 1995;177:138-149.

30. Rosen VB, Hobbs LW, Spector M. The ultrastructure of anorganic bovine bone and selected synthetic hydroxyapatites used as bone graft substitute materials. Biomaterials 2002;23:921-928.

31. Fujita R, Yokoyama A, Nodasaka Y, Kohgo T, Kawasaki T. Ultrastructure of ceramic-bone interface using hydroxyapatite and beta-tricalcium phosphate ceramics and replacement mechanism of beta-tricalcium phosphate in bone. Tissue Cell 2003;35:427-440.

32. Kim H-M, Himeno T, Kokubo T, Nakamura T. Process and kinetics of bonelike apatite formation on sintered hydroxyapatite in a simulated body fluid. Biomaterials 2005;26:4366-4373.

33. Porter AE, Patel N, Skepper JN, Best SM, Bonfield W. Effect of sintered silicate-substituted hydroxyapatite on remodeling processes at the bone-implant interface. Biomaterials 2004;25:3303-3314.

34. Zhong JP, Greenspan DC, Feng JW. A microstructural examination of apatite induced by Bioglass *in vitro*. J Mater Sci: Mater Med 2002;13:321-326.

35. Gentzsch C, Delling G, Kaiser E. Microstructural classification of resorption lacunae and perforations in human proximal femora. Calcif Tissue Int 2003;72:698-709.

36. Kneissel M, Roschger P, Steiner W, Schamall D, Kalchhauser G, Boyde A, Teschler-Nicola M. Cancellous bone structure in the growing and aging lumbar spine in a historic Nubian population. Calcified Tissue Int 1997;61:95-100.

37. Braidotti P, Bemporad E, D'Alessio T, Sciuto SA, Stagni L. Tensile experiments and SEM fractography on bovine subchondral bone. J Biomech 2000;33:1153-1157.

38. Koivukangas A, Tuukkanen J, Lehenkari P, Peura R, Hannuniemi R, Kippo K, Jamsa T, Jalovaara P. Microstructural properties of bone in rat vertebra after long-term clodronate treatment. J Bone Miner Metab 2002;20:223-227.

39. Flegler SL, Heckman JW, Klomparens KL. Scanning and transmission electron microscopy. New York: Oxford University Press; 1993. 225 p.

40. Johnson GS, Mucalo MR, Lorier MA. The processing and characterization of animal-derived bone to yield materials with biomedical applications Part 1: Modifiable porous implants from bovine condyle cancellous bone and characterization of bone materials as a function of processing. J Mater Sci: Mater Med 2000;11:427-441.

41. deGroot K. Effect of porosity and physicochemical properties on the stability, resorption, and strength of calcium phosphate ceramics. Ann N Y Acad Sci 1988;523:227-233.

42. Bodic F, Amouriq Y, Gauthier O, Gayet-Delacroix M, Bouler JM, Daclusi G, Hamel L. Computed tomography assessment of alveolar filling with an injectable bone substitute. J Mater Sci: Mater Med 2002;13:953-958.

43. Nagaraja S, Couse TL, Guldberg RE. Trabecular bone microdamage and microstructural stresses under uniaxial compression. J Biomech 2005;38:707-716.

44. Ikeda S, Morishita Y, Tsutsumi H, Ito M, Shiraishi A, Arita S, Akahoshi S, Narusawa K, Nakamura T. Reductions in bone turnover, mineral, and structure associated with mechanical properties of lumbar vertebra and femur in glucocorticoid-treated growing minipigs. Bone 2003;33:779-787.

45. Weiss P, Obadia L, Magne D, Bourges X, Rau C, Weitkamp T, Khairoun I, Bouler JM, Chappard D, Gauthier O, Daclusi G. Synchrotron X-ray microtomography (on a micron scale) provides three-dimensional imaging representation of bone ingrowth in calcium phosphate biomaterials. Biomaterials 2003;24:4591-4601.

46. Hudelmaier M, Kollstedt A, Lochmuller EM, Kuhn V, Eckstein F, Link TM. Gender differences in trabecular bone architecture of the distal radius assessed with magnetic resonance imaging and implications for mechanical competence. Osteoporosis Int 2005;16:1124-1133.

APPENDIX C

SAMPLE CALCULATION FOR PERCENT OF OSTEOBLASTS ATTACHED TO DENSE HYDROXYAPATITE SPECIMEN (CONTROL VS. MICROCRACKED, 4 HR ATTACHMENT).

MC3T3-E1 osteoblasts (OBs) were counted in 10 select fields of view, as described in Chapter 2. These counts were then used to calculate the number of cells attached on each specimen. A Microsoft Excel spreadsheet was used to determine mean attachment values and standard deviation for the control and microcracked groups.

Table 1: Cell counts taken from 10 fields of view per specimen (9 control specimens, 9 microcracked specimens).

	1	2	3	4	5	6	7	8	9	10	Mean	Per cm^2	Per sample	% of attached
C1	9	2	6	0	3	0	4	10	8	9	5.1	2454.80	10162.87	21.61
C2	2	1	4	1	18	2	5	3	3	6	4.5	2166.00	8967.24	19.07
C3	6	2	5	1	3	9	0	1	6	1	3.4	1636.53	6775.25	14.41
C4	11	0	1	11	0	2	0	1	3	1	3	1444.00	5978.16	12.71
C5	1	3	2	0	4	3	5	0	2	1	2.1	1010.80	4184.71	8.90
C6	8	19	0	2	1	2	5	2	3	1	4.3	2069.73	8568.70	18.22
C7	16	3	3	4	18	2	2	2	0	1	5.1	2454.80	10162.87	21.61
C8	1	7	13	3	2	0	1	23	0	21	7.1	3417.47	14148.31	30.08
C9	5	1	12	1	7	1	2	2	5	2	3.8	1829.07	7572.34	16.10
M1	1	5	2	8	2	4	13	3	6	1	4.5	2166.00	8967.24	19.07
M2	1	11	12	4	7	3	10	13	2	1	6.4	3080.53	12753.41	27.12
M3	9	8	5	7	7	6	1	1	2	1	4.7	2262.27	9365.78	19.91
M4	3	21	7	4	26	5	5	5	9	13	9.8	4717.07	19528.65	41.52
M5	3	4	8	12	4	4	7	11	1	2	5.6	2695.47	11159.23	23.73
M6	6	13	14	9	5	5	5	9	8	9	8.3	3995.07	16539.57	35.17
M7	9	25	13	1	3	4	5	4	4	1	6.9	3321.20	13749.77	29.23
M8	13	4	2	4	3	4	20	3	14	2	6.9	3321.20	13749.77	29.23
M9	4	17	6	17	1	8	5	4	3	21	8.6	4139.47	17137.39	36.44

Table 2: Average percent attached osteoblasts for both the control and microcracked group.

Mean	Per cm^2	Per sample	% of attached				
5.1	2454.80	10162.87	21.61				
4.5	2166.00	8967.24	19.07				
3.4	1636.53	6775.25	14.41				
3	1444.00	5978.16	12.71				
2.1	1010.80	4184.71	8.90				
4.3	2069.73	8568.70	18.22				
5.1	2454.80	10162.87	21.61		Raw Count	Per cm^2	% attached
7.1	3417.47	14148.31	30.08	MEAN	4.27	2053.69	18.08
3.8	1829.07	7572.34	16.10	STDEV	1.45	696.27	6.13
4.5	2166.00	8967.24	19.07				
6.4	3080.53	12753.41	27.12				
4.7	2262.27	9365.78	19.91				
9.8	4717.07	19528.65	41.52				
5.6	2695.47	11159.23	23.73				
8.3	3995.07	16539.57	35.17				
6.9	3321.20	13749.77	29.23		Raw Count	Per cm^2	% attached
6.9	3321.20	13749.77	29.23	MEAN	6.86	3299.81	29.05
8.6	4139.47	17137.39	36.44	STDEV	1.80	864.09	7.61

To determine statistical significance in the difference between these mean attachment values, we performed an unpaired Students t-test, taking n < 0.05 to indicate statistical significance. The results of this test are shown below. Group A is the control group and Group B is the microcracked group.

Student's t-Test: Results

The results of an unpaired t-test performed at 22:40 on 27-JAN-2007

t= -3.37
sdev= 1.63
degrees of freedom = 16 The probability of this result, assuming the null hypothesis, is **0.0039**

Group A: Number of items = 9
2.10 3.00 3.40 3.80 4.30 4.50 5.10 5.10 7.10

Mean = 4.27
95% confidence interval for Mean: 3.115 thru 5.419
Standard Deviation = 1.45
Hi = 7.10 Low = 2.10
Median = 4.30
Average Absolute Deviation from Median = 1.06

Group B: Number of items = 9
4.50 4.70 5.60 6.40 6.90 6.90 8.30 8.60 9.80

Mean = 6.86
95% confidence interval for Mean: 5.704 thru 8.008

Standard Deviation = 1.80
Hi = 9.80 Low = 4.50
Median = 6.90
Average Absolute Deviation from Median = 1.38

APPENDIX D

X-RAY DIFFRACTION OF DENSE HYDROXYAPATITE USED IN THIS STUDY

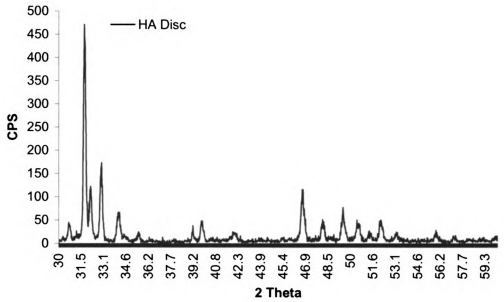

Figure 1: X-ray diffraction data of dense sintered hydroxyapatite (Taihei Chemical).

APPENDIX E

ELECTROSTATIC INTERACTIONS AS A PREDICTOR FOR OSTEOBLAST ATTACHMENT TO BIOMATERIALS

I.O. SMITH*, M.J. BAUMANN*, L.R. MCCABE‡

*Department of Chemical Engineering and Materials Science, ‡Department of Physiology, Michigan State University, East Lansing, MI 48824-1226

PUBLISHED IN: J Biomed Mater Res 2004;70A:436-441.

SYNOPSIS

The present study utilizes zeta (ζ) potential analysis as an indicator of bonding of osteoblasts (OBs) and whole bone to various biomaterials. Common metal alloys (316L stainless steel, CoCrMo and Ti6Al4V) and bioceramics (HA and β-TCP) used in orthopaedic applications were suspended in particulate form in physiologic saline (PS), both as-received and supplemented with bovine serum albumin (BSA). Metal alloys were also treated with NaOH washing to study the effect of such a surface treatment on the ζ-potential. The NaOH wash was found to increase the ζ-potential for CoCrMo and Ti6Al4V and a decrease in the magnitude of the ζ-potential for 316L stainless steel. When the metal alloy powders were suspended in BSA-supplemented PS, the ζ-potential as a function of pH increased, thereby

increasing the electronegativity gap and increasing the propensity for bonding between each of the metal alloys and bone. This increase is likely due to matrix proteins in the BSA, which adsorb onto the metal alloy surfaces, promoting bone growth. With the addition of BSA to each bioceramic system, a uniform decrease in ζ-potential was observed. However, the electronegativity gap remains large in each case, maintaining the anticipation of bonding. ζ-potential analysis is an effective predictor of biomaterial attraction to osteoblasts and bone, providing a useful in vitro method for predicting such interactions.

INTRODUCTION

The biocompatibility of biomaterials in contact with bone has been widely examined.[1] Such materials, including metals and ceramics, have a wide array of uses in orthopedic implants. However, the exact mechanisms of the implant-bone bond are not clearly understood. While surface properties, such as roughness and porosity, and chemical treatments, such as NaOH washes affect the extent of the implant to bone attachment, a comprehensive explanation for the nature of this bond is currently lacking. Biocompatible alloys such as CoCrMo, 316L stainless steel and Ti6Al4V have been commonly used in the fabrication of orthopedic implants. Calcium phosphate ceramic materials, such as hydroxyapatite (HA) and tricalcium phosphate (TCP), have been a focus in the development of surface reactive bone scaffolds and implant coatings. These bioceramics have been shown to form

an interfacial bond with bone in previous studies and it is therefore reasonable to assume they will show a propensity for bonding with osteoblast (OB) cells, which are the dominant cell type in normal physiologic bone growth.[2] Based on these findings, it is also logical by extension, to hypothesize that these ceramics will show a propensity for bonding to whole bone.

Several studies have linked the ζ-potential of bone to the piezoelectric effect.[3] Oppermann et al. examined the stability of the interactions between bone and various compositions of Bioglass© and hydroxyapatite (HA) using ζ-potential data as a function of pH.[4] Their results showed that highly stable interactions were indicative of successful *in vivo* bonding between optimum Bioglass© compositions to bone and between HA and bone. An effective method to quantitatively examine bone-implant bonding is to measure the mobility of colloidal particles in a suspension, using ultrasonic attenuation spectroscopy (UAS), from which the surface, or zeta (ζ) potential is calculated. This study will employ ζ-potential analysis using UAS, as a function of physiologically relevant pH, to predict bone-implant interactions in a variety of bioceramic and biocompatible metal powder materials. The metal powders also were washed with NaOH in order to measure any change in the implant to bone surface potentials and relate this to noted improvements in *in vivo* bone to implant bonding.[5] This approach was verified for the case of OB-HA interactions by examining *in vitro* OB cell growth and proliferation as a function of time on HA discs.

MATERIALS AND METHODS

Suspension Preparation

Metals: Three metal powders, representative of metals used in total knee and total hip prostheses were examined (316L SS (Ametek, Eighty Four, PA), 750F CoCrMo and Ti6Al4V (Powder Alloy Corp., Cincinnati, OH)). To normalize particle size in these powders, each was ball milled dry for 14 days at <2°C with Al_2O_3 grinding media prior to analysis, leaving particle sizes of 10 μm, 30 μm and 80 μm, respectively. To simulate *in vivo* exposure to proteins upon implantation and ionic activity, the ball-milled powders were next suspended at 1 volume % in physiologic saline (PS) at 0.154M NaCl with 1% (by volume) bovine serum albumin. Samples of each metal powder were then washed in 0.1M NaOH by suspending each powder and stirring for 15 minutes, then allowing particles to settle for 1.5 hours before removing liquid and allowing powder to dry under mild heat. Excess NaOH solution was decanted and the powders air-dried, before subsequent resuspension in PS for UAS measurement under a N_2 blanket. In this study, the O'Brien model, which takes into effect double-layer distortion, was used to calculate the ζ-potential from the UAS mobility data which was measured using the AcoustoSizer II ESA apparatus (Colloidal Dynamics, Warwick, RI).[6,7] Amplitudes were measured across a range of frequencies, yielding an attenuation spectrum. For each set of ζ-potential data, 30 measurements of particle size were taken and the Gaussian average of these utilized in ζ-potential calculation at each pH value. To eliminate adsorption of ions from

the atmosphere, all ζ-potential measurements for each of the materials and cells examined in this study were carried out under a N_2 blanket.

Bone: Bone stock was taken from the proximal femur of a deer harvested within 4 hours of death and sectioned for immediate grinding. The soft tissue and periosteum were removed and the bone wet ground from the sub-periosteal surface to the mid-cortex, while submerged in PS, using a diamond conical grinding bit at 3,000 rpm, under moderate hand pressure. The resulting bone particle suspension was then subjected to immediate ζ-potential measurement. For each material, the mobility was measured and the resulting ζ-potential calculated and plotted as a function of pH. The range of pH was controlled, under constant stirring, with automated titration using a complementary acid (1M HCl) and base (1M NaOH).

Osteoblasts: MC3T3-E1 mouse osteoblast cells were cultured in α minimum essential medium (α-MEM, Invitrogen Corp., Carlsbad, CA) supplemented with 10% fetal bovine serum (FBS, Atlanta Biologicals, Norcross, GA) at 37°C in a humid atmosphere containing 5% CO_2 and 95% air. The media was aspirated off and the cells washed once with 1X phosphate buffered saline. Cells were then trypsinized and subsequently pelleted by centrifuge at 10,000 rpm for 10 min. The resulting OB pellets were resuspended by aspiration in PS in 50 ml tubes. PS was prepared at three different pH levels (7.3, 7.4, 7.5) by titrating with complementary acid and base (1M HCl and 1M NaOH). The resulting suspensions were then transferred to 60 ml syringes and finally, injected in turn into the UAS cell chamber where instantaneous mobility

measurements were taken and ζ-potential values calculated and recorded as a function of pH. This technique is known as static ζ-potential measurement (as the suspension does not constantly flow through the chamber) and was chosen because of the small volume of OB suspension available for measurement.

Bioceramics: Three calcium phosphate ceramic powders, typical of those used in bone tissue engineering scaffolds were examined, unsintered HA (Berkeley Advanced Biomaterials Inc., San Leandro, CA), sintered HA and sintered β-TCP (HiMed, Old Bethpage, NY) having particle sizes of 0.85 μm, 0.95 μm and 1.15 μm, respectively. HiMed HA powder was sieved by the manufacturer using a proprietary process to achieve a narrower particle size distribution. These powders were suspended in PS and subjected to ζ-potential measurement with the AcoustoSizer II under a N_2 blanket. For each material, the ζ-potential was collected and plotted as a function of physiologically relevant pH. The pH range was controlled with automated titration with complementary acid (1M HCl) and base (1M NaOH) under constant stirring. For comparison, HA suspensions were also prepared in PS with 1% (by volume) bovine serum albumin.

RESULTS

Metal Alloys

The ζ-potentials as a function of pH for the as-received metal alloy powders are shown in Figure 1. Across three separate data sets, ζ-potential date was found to be very nearly identical for each metal. For 316L SS, the ζ-potential ranges from –1.4 at pH 6.3 to –3.2 mV at pH 7.5, while for CoCrMo and Ti6Al4V, the ζ-potential ranges from –1.3 at pH 6.3 to –1.7 mV at pH 7.8 and from –2.8 mV at pH 6.5 to –3.1 mV at pH 7.8, respectively. In each case, the metal powders possess ζ-potentials that are significantly more positive with respect to the bone which has a ζ-potential of –75 mV through the entire pH range examined and is shown in Figure 2. Kowalchuk et al., using bone particles having a diameter of >5 μm, reported ζ-potential values from 0 to -15 mV, while the bone particles used in this study have a diameter of 1μm and a ζ-potential of –75 mV across comparable pH ranges.[8] Because the magnitude of the ζ-potential is indirectly proportional to the diameter of the particulate material, the ζ-potential values obtained in this study are therefore consistent with this earlier report,[9-13] as a five-fold increase in particle size decreases the surface area of the powder by a factor of approximately five while holding volume constant. With NaOH washing, the ζ-potentials as a function of pH for each metal powder remain negative over the pH range and are shown in Figure 3 where the ζ-potential for 316L SS shifts to more negative values from –6.0 mV to –10.2 mV, more positive values for CoCrMo

from –0.4 mV to –1.0 mV and for Ti6Al4V shifting to more negative values of an approximately constant –2.5 mV.

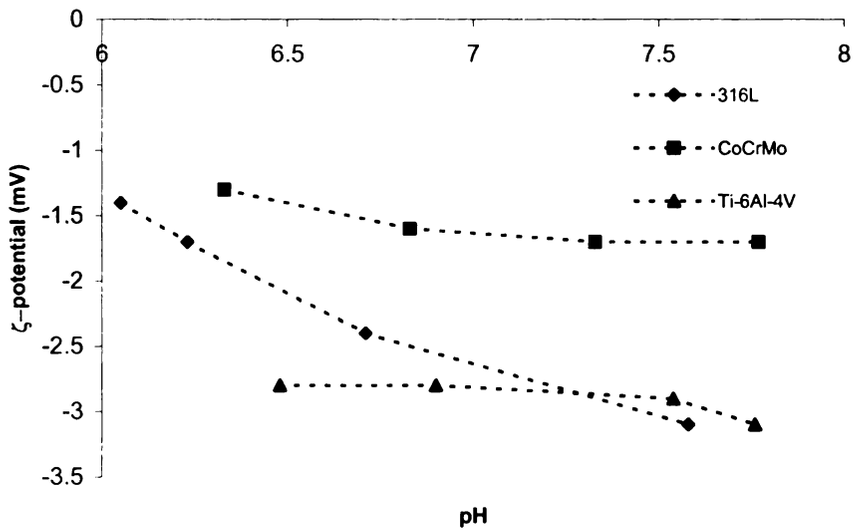

Figure 1: ζ-potential as a function of pH for as-received 316L, CoCrMo and Ti6Al4V vs. whole bone suspended at 1% in PS.

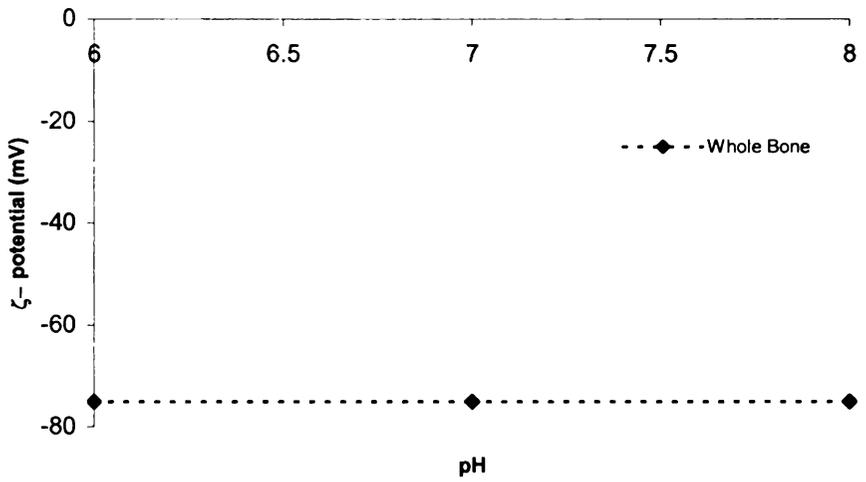

Figure 2: ζ-potential as a function of pH for ground whole deer bone suspended at 1% in PS.

The ζ-potentials as a function of pH in BSA for both the as-received and the NaOH metals are shown in Figures 4 and 5, respectively. For the as-received metals in BSA, over the indicated pH, the ζ-potential of 316L SS ranges from –2.5 to –4.8 mV, for CoCrMo from 3.7 to 2.5 mV and for Ti-6AL-4V from –1.5 to –1.7 mV. When comparing to the as-received metal alloy powders not suspended in BSA, the metal alloy powders dispersed in BSA all exhibited positive shifts in the ζ-potential. Dispersing the NaOH washed metal alloy powders in BSA over the same pH range gave positive shifts in the ζ-potentials for 316L SS from –2.2 mV to –3.6 mV, for CoCrMo from –0.3 to –1.0 mV and for Ti6Al4V a relatively constant –1.3 mV. Again, in all cases, the ζ-potential values of the metal alloy powders dispersed in BSA are significantly more positive than those of bone at a ζ-potential of –75 mV.

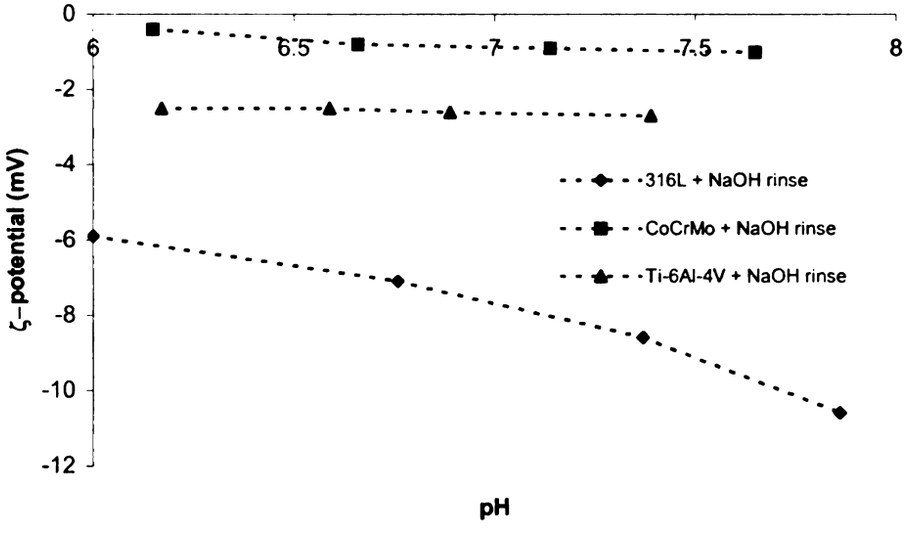

Figure 3: ζ-potential as a function of pH for NaOH-washed 316L, CoCrMo and Ti6Al4V vs. whole bone suspended at 1% in PS.

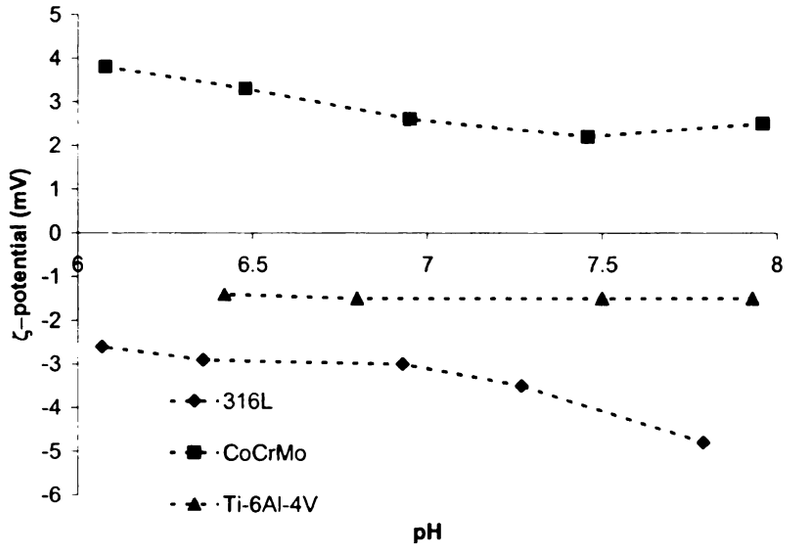

Figure 4: ζ-potential as a function of pH for as-received 316L, CoCrMo, Ti6Al4V and whole bone suspended at 1% in PS with 1% (by volume) bovine serum albumin.

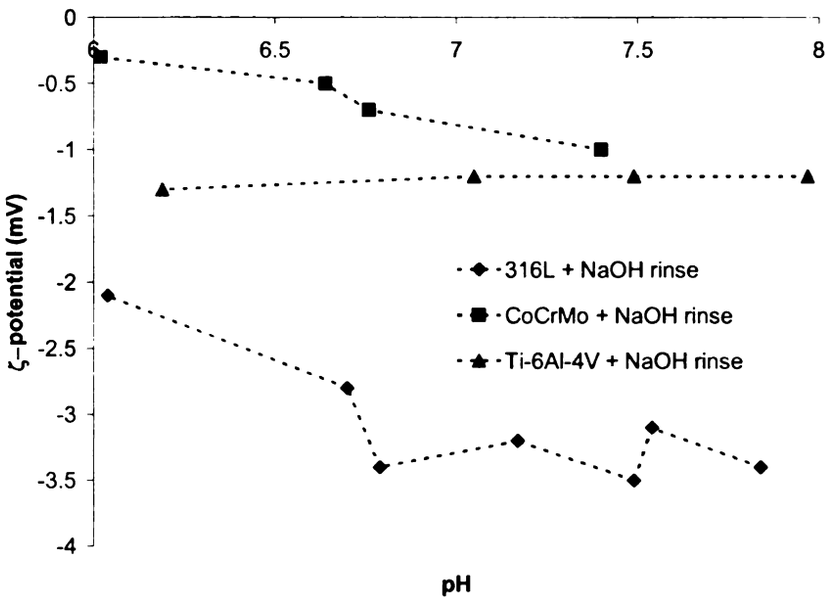

Figure 5: ζ-potential as a function of pH for NaOH-washed 316L, CoCrMo, Ti6Al4V and whole bone suspended at 1% in PS with 1% (by volume) bovine serum albumin.

Bioceramics

For OBs, whole bone, HA and β-TCP in suspension without BSA, the ζ-potential as a function of pH is shown in Figure 6. The ζ-potential of the

sintered HA ranges from 4.1 mV at pH 7 to 4.2 mV at pH 7.8. Unsintered HA has a ζ-potential from 17.1 mV at pH 6.7 to 14.5 mV at pH 7.7 and β-TCP has a relatively constant ζ-potential from 2.5 mV at pH 6.6 to 2.1 mV at pH 8.1. With BSA additions, shown in Figure 7, the ζ-potential of sintered HA shows little change from the ζ-potential values of the suspension without BSA, having a ζ-potential from 3.8 mV at pH 6.1 to 3.5 mV at pH 7.6. The unsintered HA has a ζ-potential ranging from 11.8 mV at pH 6 to 10.4 mV at pH 7.7 while the β-TCP has ζ-potentials ranging from 1.1 mV at pH 6.1 to –0.5 mV at pH 8. From pH 7.3 to 7.5, OBs had negative ζ-potentials of –29.4 mV to –52.4 mV.

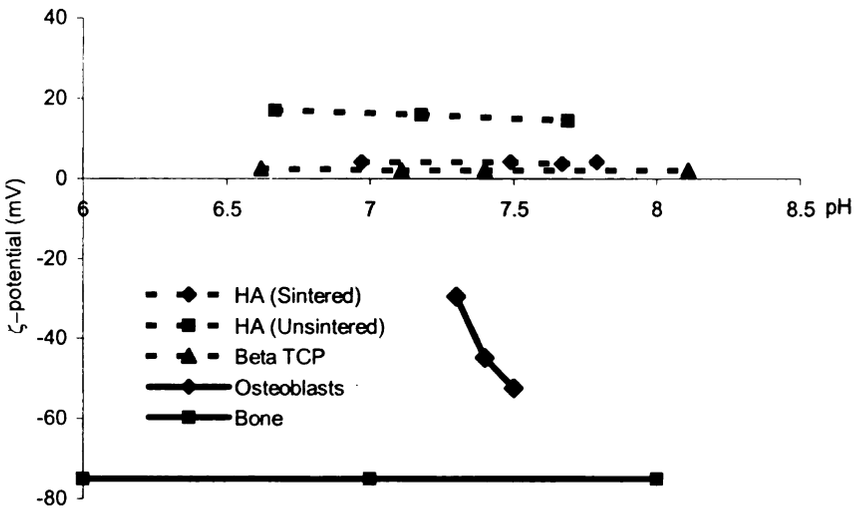

Figure 6: ζ-potential as a function of pH for HA (sintered), HA (unsintered), ζ-TCP, osteoblasts and whole bone suspended at 1% in PS.

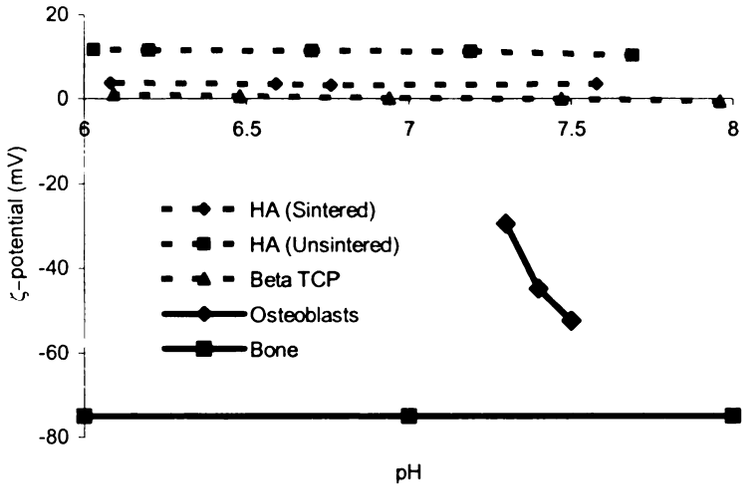

Figure 7: ζ-potential as a function of pH for HA (sintered), HA (unsintered) and β-TCP in 1% (by volume) bovine serum albumin in comparison to osteoblasts and whole bone suspended at 1% in PS.

DISCUSSION

Metal Alloys

Each of the metal alloy powders, over the given pH range, has an average ζ-potential value near zero, where NaOH treatment caused an increase in the ζ-potential for CoCrMo and Ti6Al4V and a decrease in the magnitude of the ζ-potential for 316L stainless steel. While it is widely held that none of these common orthopaedic materials exhibits direct bonding to bone, NaOH treatment has been shown to increase apatite layer formation *in vitro* on the surface of Ti alloys.[14,15] Here, Ti forms an alkali titanate hydrogel layer to which bone is observed to directly bond, both *in vitro* and *in vivo*.[14] While the zero point of charge for Ti occurs at pH 6.2, over the physiologic pH ranges used in the current study (pH 6-8), it is therefore expected that the Ti6Al4V

would be negatively charged as shown in Figure 1.[16] With exposure to NaOH, Kim et al. postulate that the titanium oxide on the Ti6Al4V surface is partially dissolved by the OH^- ions, to form $HTiO_3^-$ at the same time as the underlying base Ti metal is hydrating to form $Ti(OH)_3^+$.[14] Therefore, with NaOH treatment, there is an increase in the number of positive ions formed on the Ti6Al4V surface that corresponds to the noted increase in ζ-potential found in this study and shown in Figure 3. In the case of 316L, it is possible that the steel's self-healing oxidation layer may not remain impermeable to continued dissolution in an OH^- -containing environment. This may contribute to the larger variation in ζ-potential values experienced by the 316L SS in comparison to either the CoCr or the Ti6Al4V powders.[17] Significant electronegativity differences |~75mV| between whole bone and each of the metal alloy powder materials were observed. This large gap in electronegativity suggests a propensity for electrostatic bonding between each metal alloy and whole bone.

BSA was added to each colloidal system in order to create an *in vitro* environment that more closely matches *in vivo* conditions. Our results demonstrate that BSA increases the electronegativity gap, and therefore attraction, between each of the metal alloys and bone. In addition, BSA contains extracellular matrix proteins, such as fibronectin, that adsorb onto metal surfaces, thereby providing sites for integrin mediated osteoblast attachment. Specific integrin and extracellular matrix combinations can

influence osteoblast adhesion and contribute to surface attraction and subsequent promotion of bone growth.

Bioceramics

Unsintered HA exhibits uniformly greater ζ-potential values in comparison to sintered HA, ~17 mV as compared to ~4 mV, over the given pH range. While x-ray diffraction results (not shown here) for both the sintered and unsintered HA powders demonstrate that the only phase present is pure hydroxyapatite, the Ca/P ratio determined by energy dispersive spectroscopy are similar but not identical (2.30±0.2 for unsintered HA and 1.67±0.08 for sintered HA). Therefore, differences in powder processing have led to changes in the Ca/P ratio, which have altered the surface chemistry, leading to differences in the surface or ζ-potential. The differences in the ζ-potential in turn necessitate changes in the experimental protocol if these powders are processed in an aqueous slurry. For example, the higher magnitude of the ζ-potential in the unsintered HA makes it is easier to disperse and form a uniform slurry. A uniform slurry is necessary to form a uniform green body, and hence a uniform scaffold.[18] Unsintered HA also has a greater electronegativity difference with respect to both osteoblast and whole bone in comparison to sintered HA and β-TCP. Therefore, unsintered HA would be expected to show a greater propensity for bonding with both osteoblasts and whole bone. However, as an unsintered powder must still be sintered to form a scaffold, it is worthwhile to note that significant electronegativity differences are still present for both sintered HA and β-TCP. Another factor that accounts for the

differences in ζ-potential between these bioceramics are the differences in particle size. Because the magnitude of the ζ-potential is indirectly proportional to the diameter of the particulate material, the differences in ζ-potential can also be partially attributed to the fact that unsintered HA has a mean particle size that is less than that of sintered HA, 0.85 μm versus 0.95 μm, respectively. The low ζ-potential values for the β-TCP ($Ca_3(PO_4)_2$) may be understood by noting the lack of hydroxyl groups, which are charge determining ions on HA ($Ca_{10}(PO_4)_6(OH)_2$).

Contrary to the metals examined in this study, BSA additions to the bioceramic suspensions acted to uniformly lower the ζ-potential measurements for each material. However, the electronegativity difference between each of these bioceramics with respect to either osteoblasts or whole bone, is still on the order of 80 mV, meaning that attraction and bonding between these materials and bone is still anticipated. These findings reinforce the argument that calcium phosphate ceramics are suitable for bone scaffold applications, both for osteoblast seeding as well as attachment to existing bone. Future studies will probe the experimental link between surface potential and OB attachment and mineralization.

ACKNOWLEDGEMENTS

Funding for this study was granted by the National Science Foundation (DMR0074439) and the MSU Foundation. Assistance in osteoblast cell

culture was kindly provided by M. Hossain and R. McMullen and for x-ray diffraction measurements to M. Soto.

REFERENCES

1. Park JB, Lakes RS. Biomaterials: An Introduction. 2nd ed. Plenum Press, NY 1992

2. Vander, Sherman, Luciano. Human Physiology: The Mechanisms of Body Function. 8th ed. McGraw Hill, NY 2001

3. Fukada E, Yasuda I, On the piezoelectric effect of bone. J. Phys. Soc., 12: 1158-1162, (1957).

4. Oppermann DA, Crimp MJ, Bement DM, *In vitro* stability predictions for the bone/bioglass and bone/HA interactions, J. Biomed. Mater. Res., 42:412-416 (1998)

5. Gross K. Fluor-hydroxyapatite solid solutions as alternative bioceramics. Proceedings from International Society of Ceramics in Medicine, Bioceramics-14 , B6 (2001)

6. O'Brien RW. Electro-acoustic effects in a dilute suspension of spherical particles. J. Fluid Mech., 190, 71-86 (1986)

7. O'Brien RW. The Electro-acoustic equation for a colloidal suspension. J. Fluid Mech., 212, 81-93 (1990)

8. Kowalchuk RM, Pollack SR, Corcoran TA. Zeta potential of bone from particle electrophoresis: Solution composition and kinetic effects. J. Biomed. Mater. Res., 29, 47-57 (1995)

9. Lange FF. Powder processing science and technology for increased reliability. J. Am. Ceram. Soc., 72, 3-15 (1989)

10. Velamekanni BV, Lange FF. Effect of interparticle potentials and sedimentation on particle packing density of bimodal particle distributions during pressure filtration. J. Am. Ceram. Soc. 74, 166-172 (1991)

11. Chang JC, Velamekanni BV, Lange FF, Pearson DS, Centrifugal Consolidation of Al_2O_3 and Al_2O_3/ZrO_2 Composite Slurries vs. Interparticle Potentials: Particle Packing and Mass Segregation. J. Am. Ceram. Soc., 74, 2201-2204 (1991)

12. Crimp MJ, Oppermann DA. Green Density Variations in Relation to Colloidal Packing in SiC/Si_3N_4 Composites. Proc. Am. Ceram. Soc.: Science, Technology and Applications of Colloidal Suspensions, 91-101 (1995)

13. Crimp MJ. A Novel Approach to Intermetallic Matrix Composite (IMC) Processing. J. Mater. Sci. Eng., A192/193, 633-639 (1995)

14. Kim H-M, Miyaji F, Kokubo T, Nakamura T. Preparation of bioactive Ti and its alloys via simple chemical surface treatment. J. Biomed. Mater. Res., 32, 409-417 (1996)

15. Wang CX, Wang M. Electrochemical impedance study of the nucleation and growth of apatite on titanium pretreated with NaOH solution. Society for Biomaterials 27th Annual Meeting, 101 (2001)

16. Boehm HP. Acidic and basic properties of hydroxylated metal oxide surfaces. Disc. Farad. Soc., 52, 264-275 (1971)

17. Smith, WF. Principles of Materials Science and Engineering. McGraw-Hill, NY 1986

18. Sacks MD. Rheological science in ceramic processing. Science of Ceramic Chemical Processing, Ed. L.L. Hench and D.R. Ulrich, J. Wiley & Sons, 522-538 (1986)

APPENDIX F

SURFACE POTENTIAL AND OSTEOBLAST ATTRACTION TO CALCIUM PHOSPHATE COMPOUNDS IS AFFECTED BY SELECTED ALKALINE HYDROLYSIS PROCESSING

I.O. SMITH*, M.J. BAUMANN*, L. OBADIA‡, J-M BOULER‡,
*Department of Chemical Engineering and Materials Science, Michigan State University, East Lansing, MI 48824-1226, USA, ‡INSERM EM99-03, Faculté de Chirurgie Dentaire, BP 84215, 44042 Nantes, France

PUBLISHED IN: J Mater Sci:Mater Med 2004;15:841-846.

ABSTRACT

This study examines the link(s) between the suspension behavior of calcium deficient apatites (CDAs) and biphasic calcium phosphate (BCP), as measured by the ζ-potential, with respect to both whole bone and osteoblasts. CDA is fabricated by hydrolyzing an acidic CaP such as dicalcium diphosphate dihydrate (DCPD; $CaHPO_4$, $2H_2O$) and has a structure and composition close to bone apatite. Sintering CDA results in the formation of BCP ceramics consisting of mixtures of HA and β-TCP, with the HA/β-TCP weight ratio proportional to the Ca/P ratio of CDA. The choice of the base for the DCPD hydrolysis allows various ionic partial substitution of the formed CDA. Na for Ca partial substitution is of interest because of the resulting improvement in mechanical properties of the resulting BCP ceramics and NH_4OH was used as a negative control. The ζ-potential was measured for these materials and the stability of the ceramic to bone interaction calculated. ζ-potential values decrease for CDA(NH_4OH) versus CDA(NaOH) and

increase for BCP(NH_4OH) versus BCP(NaOH). While results of these analyses indicate that NH_4OH and NaOH processed CDA and BCP will likely yield osteoblast attachment *in vivo*, differences in the ζ-potentials may explain varying degrees of cell attachment.

INTRODUCTION

The surface potential of orthopedic biomaterials in contact with bone has been the subject of recent interest, however, the exact mechanisms of the implant to bone bond are not clearly understood. [1-3] While surface functional groups such as carboxyl and hydroxyl ions determine the surface charge and hence the surface potential of many common ceramics, the degree to which such surface groups alter the resulting ceramic to osteoblast or bone attachment is less understood. [4-5] Bioceramics such as hydroxyapatite (HA; $Ca_{10}(PO_4)_6(OH)_2$) and beta-tricalcium phosphate (β-TCP; $Ca_3(PO4)_2$), have been a focus in the development of osteoconductive scaffolds for bone tissue engineering and improved orthopaedic implant coatings. [6-8] They respectively present hexagonal and rhombohedral crystal symmetries. [9]

The link between the surface potential, as assessed by the zeta (ζ) potential, of these bioceramics and their resulting attraction to both bone and osteoblasts, have been shown in previous studies. [1-3] The focus of this paper is the relationship between modifications in the processing method of calcium phosphate powders and their resulting ζ-potential, and hence

suitability for use as bone tissue engineering scaffolds. Several studies have linked the surface, or ζ-potential of bone to the piezoelectric effect. Oppermann et al. examined the stability of the interactions between bone and various compositions of Bioglass™ and hydroxyapatite (HA) using ζ-potential data as a function of pH. [2] Their results showed that unstable interactions were indicative of successful *in vivo* bonding between optimum Bioglass™ compositions and bone and between HA and bone. An effective method to quantitatively examine bone-implant bonding is to measure the mobility of colloidal particles in a suspension, using ultrasonic attenuation spectroscopy (UAS), from which the surface, or ζ-potential is calculated. This study will employ ζ-potential analysis using UAS, as a function of physiologically relevant pH, to predict bone-implant interactions in a variety of bioceramic powder materials that have been synthesized via two different processing methods.

One possible way of forming calcium deficient apatite (CDA) with both a structure and composition close to bone apatite is by hydrolyzing an acidic calcium phosphate phase such as dicalcium diphosphate dihydrate (DCPD; $CaHPO_4$, $2H_2O$). [10-11] Sintering CDA between 900°C and 1200°C results in the formation of biphasic calcium phosphate (BCP) ceramics consisting of mixtures of HA and β-TCP with the HA/β-TCP weight ratio proportional to the Ca/P ratio of CDA. [12] The choice of the base for the DCPD hydrolysis allows various ionic partial substitution of the formed CDA. Na for Ca partial substitution is of interest because of the resulting improvement in mechanical

properties of the final BCP ceramics. [13] Although biological fluids contain large quantities of ionic sodium, the biological role of ionic sodium within calcium phosphate (CaP) materials, with respect to cell adhesion and activity, remains unclear. In order to measure the influence of Na-substitution on the surface potentials of CaP materials, two kinds of chemical bases NH_4OH and NaOH were chosen, knowing that NH_4OH does not induce any particular ionic substitution.

The degree of ionic activity between bone and synthetic materials may be assessed through the ζ-potential as calculated from the acoustophoretic particle mobility. O'Brien and Oja have extensively described the electrokinetic phenomena of acoustophoresis. [14-16] The ζ-potential is calculated using the acoustophoretic mobility with a correction for the particle inertia $G(\alpha)^{-1}$, in an alternating field. This correction reduces the velocity amplitude of particle motion and was derived using the Helmholtz-Smoluchowski equation. [14-15]

$$\zeta = (\mu\eta / \varepsilon_o \varepsilon_r) G(\alpha)^{-1} \tag{1}$$

Where ε_o is the permitivity in a vacuum, ε_r is the relative permitivity, and $G(\alpha)^{-1}$ is given by:

$$G(\alpha)^{-1} = \left[1 - \frac{i\alpha(3 + 2\Delta\rho/\rho)}{9\{1 + (1-i)(\alpha/2)^{1/2}\}}\right] \tag{2}$$

To describe the effects of homo- and heterocoagulation and to generate a quantitative theory for the overall kinetic stability of a system of non-identical particles, Hogg et al. developed an expression for interparticle

stability (W_{ij}). This factor, termed the stability ratio is in effect, the ratio of particle collision to collisions that result in agglomeration. [19]

$$W_{ij} = \int_{a_i + a_j}^{\infty} \exp\left(\frac{V_T}{kT}\right) \frac{dr}{r^2} \qquad (3)$$

where the interparticle intercomponent stability (W_{ij}) varies exponentially with the total force, V_T, (attractive and repulsive) and inversely with the square of the particle separation distance, r, from a separation equal to the sum of the two particle radii, a_i and a_j to an infinite separation distance into the solution. The repulsive force, which acts as a barrier to coagulation is proportional to the surface charge of the particle. However, this surface charge is not readily measurable because of continuous ion activity at the particle/fluid interface. Therefore, the surface charge is estimated at the double layer by the ζ-potential, which in this study, is measured using ultrasonic attenuation spectroscopy (UAS) methods. Stable interactions, i.e. suspensions for which there is no flocculation exist at $W > 20$, while unstable interactions are predicted for systems where $W < 20$.

MATERIALS AND METHODS

Powder Processing Methods

Calcium-deficient apatite (CDA; $Ca_{10-x}(HPO_4)_x(PO_4)_{6-x}(OH)_{2-x}$) powders were obtained by hydrolysing two, 40g batches of dicalcium phosphate dihydrate (DCPD) powder (Merck, Darmstadt, Germany) in aqueous alkaline solutions (500ml with [NaOH] = 0.35 M and [NH_4OH] = 0.3M). These two chemical reactions were performed at 90°C under stable magnetic stirring for

4 hours. The CDA powders were washed with distilled water and dried (80°C, 12h). They were then calcinated at 1050 °C for 4 hours to obtain a biphasic calcium phosphate (BCP), a solid mixture of HA and β-TCP.

Powder Analysis

The purity of the starting and final materials was analyzed by assessing specific surface area (SSA) and Na content: SSA of both CDA and BCP powders were measured by BET adsorption and the sodium content was checked using atomic absorption spectroscopy.

Suspension Preparation

In this study, the O'Brien model, which takes into effect double-layer distortion, was used to calculate the ζ-potential from the UAS mobility data, which was measured using the AcoustoSizer II ESA apparatus (Colloidal Dynamics, Warwick, RI). To eliminate adsorption of ions from the atmosphere, all ζ-potential measurements for each of the materials and cells examined in this study were carried out under a N_2 blanket. Measurements were not made in the presence of an adsorbed protein such as bovine serum albumin as prior work has shown it to have only minimal effect on the surface potential. [20] All suspensions were prepared in physiologic saline (PS; 0.154M NaCl) at a concentration of ~1 volume%.

Bone: Bone stock was taken from the proximal femur of a deer harvested within 4 hours of death and sectioned for immediate grinding. The soft tissue and periosteum were removed and the bone wet ground from the sub-periosteal surface to the mid-cortex, while submerged in PS, using a diamond

conical grinding bit at 3,000rpm, under moderate hand pressure. The resulting bone particle suspension was then subjected to immediate ζ-potential and particle size measurement.

Osteoblasts: MC3T3-E1 mouse osteoblast cells were cultured in α minimum essential medium (α-MEM, Invitrogen Corp., Carlsbad, CA) supplemented with 10% fetal bovine serum (FBS, Atlanta Biologicals, Norcross, GA) at 37°C in a humid atmosphere containing 5% CO_2 and 95% air. The media was aspirated off and the cells washed once with 1X phosphate buffered saline. Cells were then trypsinized and subsequently pelleted by centrifuging at 10,000rpm for 10min. The resulting OB pellets were resuspended by aspiration in PS in 50ml tubes. PS was prepared at three different pH levels (7.3, 7.4, 7.5) by titrating with complementary acid and base (1M HCl and 1M NaOH). The resulting suspensions were then transferred to 60ml syringes and finally, injected in turn into the UAS cell chamber where instantaneous mobility measurements were taken and ζ-potential values calculated and recorded as a function of pH. This technique is known as static ζ-potential measurement (as the suspension does not constantly flow through the chamber) and was chosen because of the small volume of OB suspension available for measurement.

Bioceramics: Two types of CDA (hydrolized using NaOH and NH_4OH) along with two types of BCP bioceramic were assessed for differences in their ζ-potential. The average diameters of the CDA (NaOH), CDA (NH_4OH), BCP (NaOH) and BCP (NH_4OH) were measured, under identical suspension

conditions, as 0.95, 0.85, 1.0 and 0.93μm, respectively. Because the magnitude of the ζ-potential is indirectly proportional to the diameter of the particulate material, the bone was ground until a particle size of 1μm was reached. These particle sizes were also measured as a function of pH to detect agglomeration and each of the powders remained essentially unagglomerated throughout the pH range examined. Each powder was suspended in PS and subjected to ζ-potential measurement with the AcoustoSizer II under a N_2 blanket. The ζ-potential was then collected and plotted as a function of physiologically relevant pH. The pH range was controlled with automated titration with complementary acid (1M HCl) and base (1M NaOH) under constant stirring.

RESULTS AND DISCUSSION

Powder analysis

FTIR spectra (not shown) verified that the classic PO_4 and OH vibration peaks were present and that the presence of carbonate and hydrogenophosphate bands was minimally present for both CDA powders. [21]

Rietvelt analysis is applied to XRD data for polycrystalline materials in order to better refine peaks, yielding a more accurate determination of the crystal structure. In this study, Rietvelt refinement was used to determine the lattice parameters of the HA and β-TCP in BCP(NaOH) (HA: a = b = 0.9416(2); c = 0.6887(2) / β-TCP: a = b = 1.0408(2); c = 3.7228(9)) and in BCP(NH_4OH) (HA: a = b = 0.9420(2); c = 0.6881(2) / β-TCP: a = b =

1.0403(2); c = 3.7368(9)) (all values in nanometers). The HA/β-TCP weight ratio was found to be 3.48/6.52±0.301 for BCP(NH_4OH) and 3.53/6.57±0.352 for BCP(NaOH). This yielded the atomic Ca/P ratios for both CDA/BCP(NH_4OH): 1.56 and CDA/BCP(NaOH): 1.57. Only the c values for β-TCP, present in both BCP powders, were significantly different. This indicates that Na for Ca substitution occurs preferentially in the β-TCP phase. According to the crystal structure of β-TCP, the only possible Ca site is the incomplete one noted Ca(4).

Specific surface area (SSA) was determined using BET adsorption. The SSA is 120.3±0.15 m^2/g for CDA(NH_4OH), 60.7±0.05 m^2/g for CDA(NaOH) and 2.85±0.01m^2/g for both BCP powders. Atomic absorption spectroscopy measurements give Na content for both CDA(NaOH) and BCP(NaOH) as 1.97±0.09%. For both CDA(NH_4OH) and BCP(NH_4OH), the amount of Na was found to be 0.45±0.09%. This latter result is due to Na impurities present in the dicalcium phosphate dihydrate ($CaHPO_4 \cdot H_20$, also known as DCPD), which is used as a starting material in the alkaline hydrolysis.

ζ-potential

ζ-potential data, as a function of pH, for the calcium phosphate powders is shown in Figure 1. The iso-electric point (iep) is the pH at which the *net* surface potential is zero. The iep for the CDA powders varies from a pH of 6.8 for the CDA (NH_4OH) shifting to a more basic pH of 7.4 for the CDA (NaOH), while the BCP processed with NH_4OH does not exhibit an iep over the pH

range tested and the BCP processed using NaOH has an iep at pH 6.4. The BCP (NH_4OH) powder behaves very much like commercially available HA, having relatively little positive potential and no iep. [20] The ζ-potential values range from 5.1 to –0.7mV for the CDA (NaOH), 1.5 to –4.2mV for the CDA (NH_4OH), 1.5 to –2.8mV for the BCP (NaOH) and 2.9 to 1.5mV for the BCP (NH_4OH) over the approximate pH range from 6 to 8. Sodium substitution in the CDA powders caused a slight increase in the overall ζ-potential curve while in the BCP powders, it led to a slight decrease in the overall ζ-potential values. This decrease in the BCP ζ-potential with sodium ion substitution is logical considering that Na ions having a +1 charge are substituting for Ca ions having a +2 charge, thus decreasing the overall net charge within the material. The smaller positive shift in the CDA materials may indicate either that an insufficient amount of Na was substituted into the structure and/or that NH_4OH caused other changes in the surface chemistry of CDA that resulted in the noted increase in the overall surface potential.

Kowalchuk et al., using bone particles having a diameter of >5μm, reported ζ-potential values from 0 to -15mV, while the bone particles used in this study have a diameter of 1μm and a relatively constant ζ-potential of –75mV across comparable pH ranges. [23] Because the magnitude of the ζ-potential is indirectly proportional to the diameter of the particulate material, the ζ-potential values obtained in this study are therefore consistent with this earlier finding. [3],[17],[24-26]

Stability

Stability calculations plotted as a function of pH for CDA(NaOH), CDA(NH_4OH), BCP(NaOH) and BCP (NH_4OH) are shown in Figures 2-5. At all pHs tested, the CDA(NaOH) remained unstable ($W_{11} < 20$) and is predicted to flocculate in suspension in physiologic saline while the bone shows values of stability, $W_{22} > 20$, and is hence stable over all test pHs. Interestingly, even though there is a difference in both the sign and hence the magnitude of the zeta potential between the bone and the CDA(NaOH), the interaction between the bone and bioceramic (W_{12}) is predicted to be stable ($W_{12} > 20$) and hence each component will remain separately stable and unflocculated over the pH range. Similar results were also found for the CDA(NH_4OH), BCP(NaOH) and BCP (NH_4OH).

A.

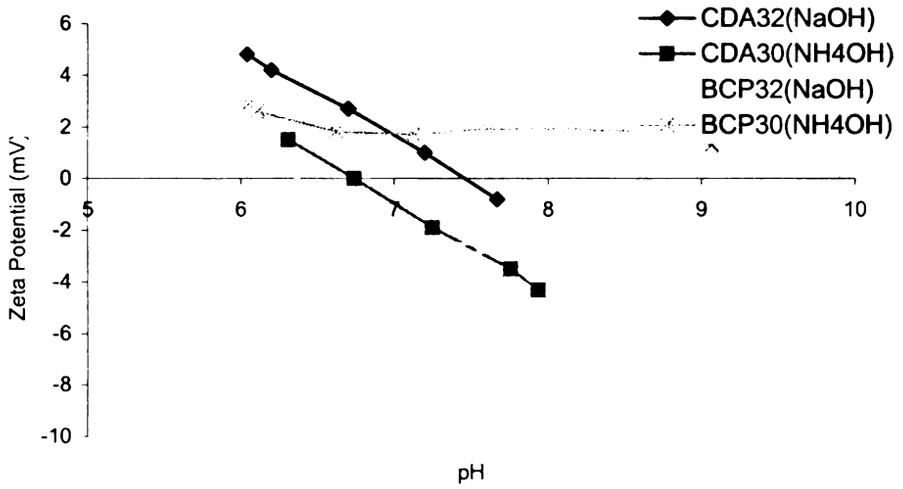

B.

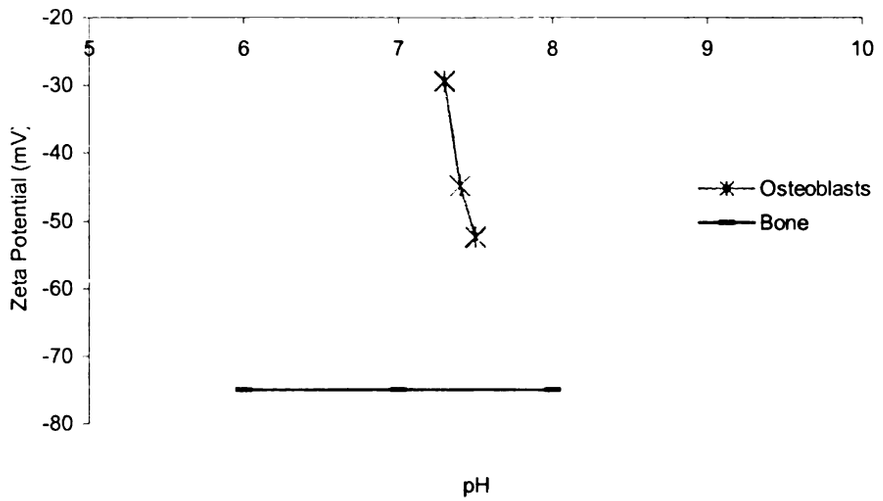

Figure 1: ζ-potential for CDA(NaOH), CDA(NH_4OH), BCP(NaOH), and BCP(NH_4OH) (2A). ζ-potential for MC3T3-E1 mouse osteoblasts and ground bone (2B).Both figure 2A and 2B are shown as a function of physiologically relevant pH at solids loadings of ~1 volume % in 0.154 M NaCl electrolyte.

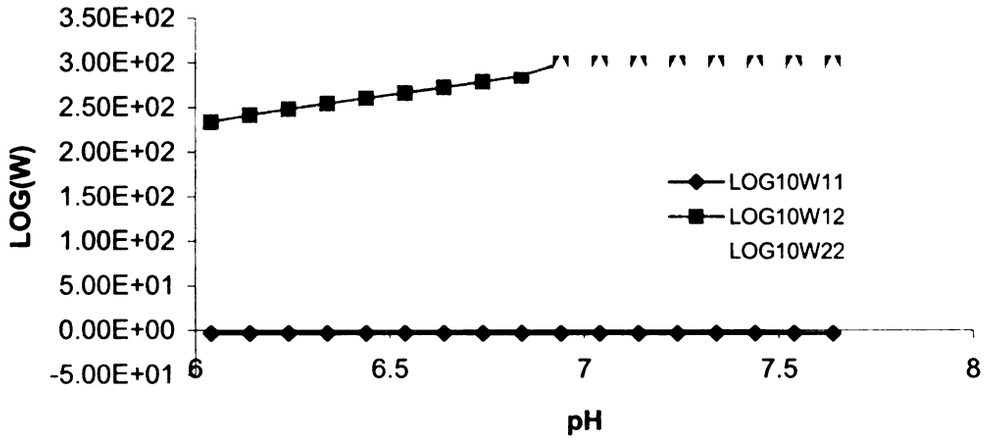

Figure 2: Stability calculations for CDA(NaOH), denoted W_{11}, bone (W_{22}) and the interaction between CDA(NaOH) and bone (W_{12}).

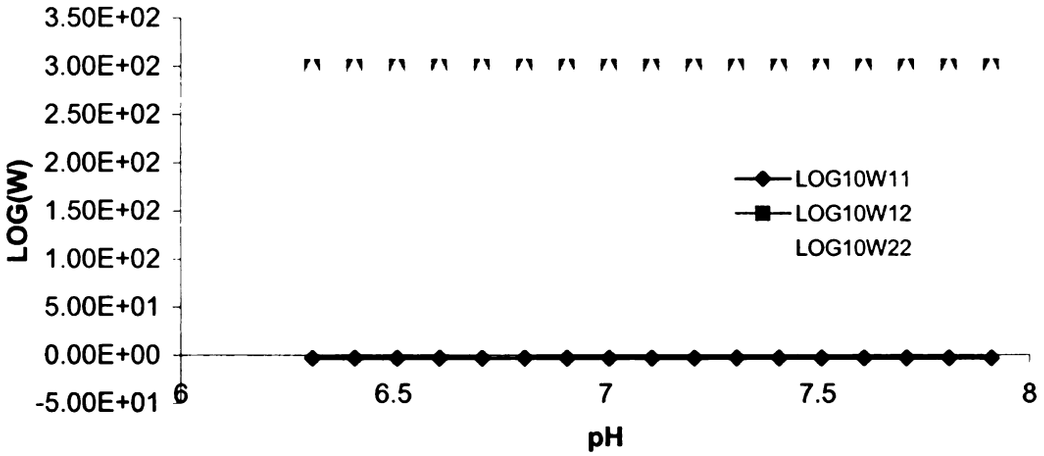

Figure 3: Stability calculations for CDA(NH_4OH), denoted W_{11}, bone (W_{22}) and the interaction between CDA(NH_4OH) and bone (W_{12}).

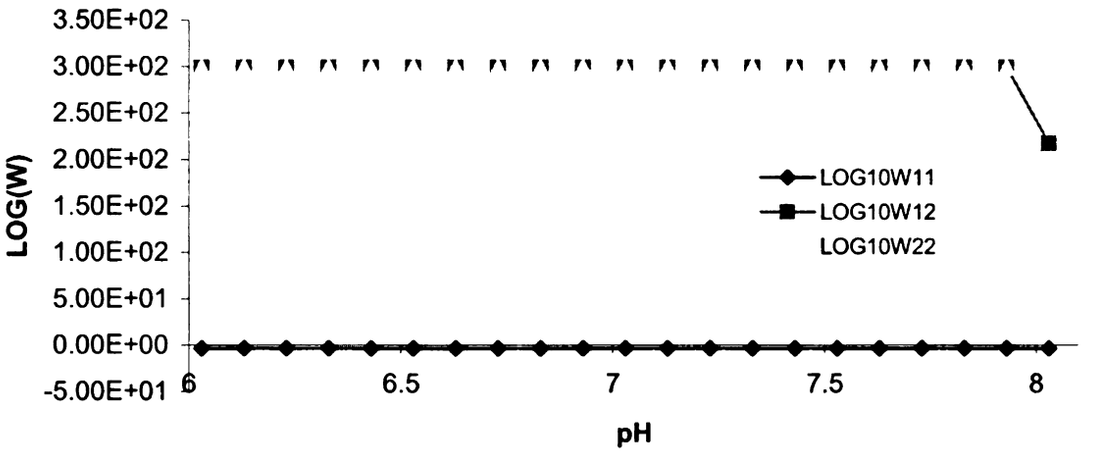

Figure 4: Stability calculations for BCP(NaOH), denoted W_{11}, bone (W_{22}) and the interaction between BCP(NaOH) and bone (W_{12}).

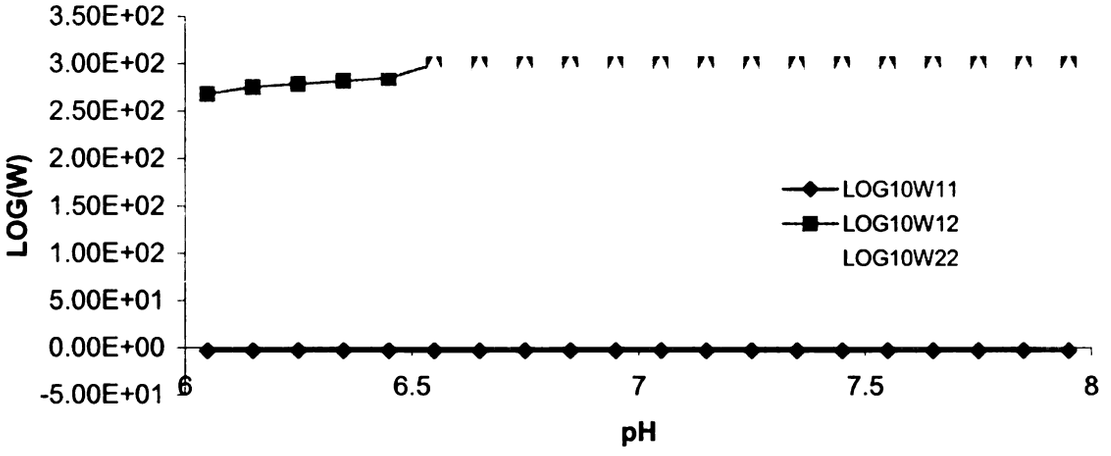

Figure 5: Stability calculations for BCP(NH_4OH), denoted W_{11}, bone (W_{22}) and the interaction between BCP(NH_4OH) and bone (W_{12}).

While it is well known that osteoblasts attach to calcium phosphate surfaces, and indeed bone has been shown to integrate into these implant materials, the mechanisms for such bonding are not completely understood. [27] The ζ-potential results in this paper agree with those reported by

Ducheyne et al. who found small ζ-potentials of 0-10mV using <5μm hydroxyapatite powders. [28] The powders in this study were submicron in size, giving comparable magnitudes and sign for the ζ-potential. Using a comparably sized HA powder (diameter < 5μm) purchased from a commercial supplier, Oppermann et al. report much greater ζ-potentials on the order of ~130mV. Therefore, while both of these powders are nominally hydroxyapatite, they have very different surface potentials, which are likely to result from differences in powder processing and surface area.

So, while the hydroxyapatite-based powders in this study have similar particle sizes and ζ-potential magnitudes, the effect of different processing treatments, such as sodium substitution on both the surface potential and SSA, must still be further evaluated. As each of the powders examined in the current study are calcium phosphate-based, it is logical to expect that their surface potentials are similar, which indeed, the data from Figure 1 illustrate. The primary difference between the two groups of calcium phosphate powders is the nature of the inorganic base (NH_4OH and NaOH) in the hydrolysis reaction during powder processing. Sodium ions are added to substitute partially for Ca in both the HA and β-TCP phases, where the Ca/P ratio decreases with Na substitution but the (Ca+Na/2)/P ratio remains constant, and these Na ions will then alter the surface chemistry. Such cation substitutions, if concentrated on the powder surface, should yield a disproportionate change the net overall surface potential, and hence the resulting ζ-potential of the powder. However, the specific surface area (SSA)

was found to be twice as high for CDA (NH_4OH), at ~120 m^2/g, in comparison to CDA (NaOH), at ~60 m^2/g. This doubling of SSA with NH_4OH may also be a factor in understanding why sodium substitution did not produce the expected decrease in the ζ-potential for the CDA powders. In addition, if it is assumed that only the atoms at the surface of the CaP are contributing to the surface potential, then a 2% addition of Na to the particle only involves ~$1.3x10^{-4}$% increase in Na at the surface of 1μm particles. Therefore, such a slight change may not be detected by ζ-potential analysis. Further work will include measuring the ζ-potential of CDA and BCP powders with increased Na substitution to verify the nature of the changes in the surface potential.

Differences in the ζ-potential in turn necessitate changes in the experimental protocol if these powders are processed in aqueous slurries. For example, the greater the magnitude of the ζ-potential, the easier it is to disperse and form a uniform slurry. A uniform slurry is necessary to form a uniform green body, and hence a uniform scaffold. [29] None of the ceramic materials tested in this study have a sufficiently large enough ζ-potential to exist as a dispersed, stable suspension, however all of the calcium phosphate powders examined have zeta potential curves that have a sufficiently large enough electronegativity gap with respect to both bone and osteoblasts to expect that each calcium phosphate would favor the initial attachment of osteoblasts.

Such differences may be the key to interpreting conflicting osteoblast attachment results. Given the significant difference between the magnitude

and sign between the ζ-potentials of each of the calcium phosphate powders and both the osteoblasts and bone at pH 7.4 (≥50mV and ≥70mV, respectively), it may be that while the stability curves rightly represent the thermodynamic steady-state, osteoblast attachment to any of the calcium phosphate powders examined in this paper is more accurately characterized by differences in the sign of the net ζ-potentials at a given pH because osteoblast attachment occurs over short times, involving multiple organic and cellular components.

ACKNOWLEDGEMENTS

Funding for this study was granted by the National Science Foundation (DMR0074439), the MSU Foundation and CPER Pays de la Loire – Axe Biomatériaux S3.

REFERENCES

1. D.A. Oppermann, M.J. Crimp and D. Bement, "*In vitro* stability predictions for the bone/hydroxyapatite composite system", *J. Biomed. Mater. Res.*, **42**, 3, (1998) 412-416.

2. M.J. Crimp, D.A. Oppermann and U. Doctor, "*In vitro* stability predictions for the bone/bioglass and bone/HA interactions", American Ceramic Society, in "Bioceramics: Materials and Applications III", (2000) p. 1-13.

3. F.B. Bagambisa, U. Joos and W. Schilli, "Mechanisms and structure of the bond between bone and hydroxyapatite", *J. Biomed. Mater. Res.*, **27**, (1993) 1047-1055.

4. F.B. Bagambisa, U. Joos and W. Schilli, "The interaction of osteogenic cells with hydroxyapatite implant materials *in vitro* and *in vivo*", *Int. J. Oral Maxillofac. Implants*, **5**, (1990) 217-226.

5. B.A. Wilson and M.J. Crimp, "Prediction of composite colloidal suspension stability based upon the HHF interpretation", *Langmuir (The American Chemical Society's Journal of Surfaces and Colloids)*, **9**, (1993) 2836.

6. O. Malard, J. M. Bouler, J. Guicheux, D. Heymann, P. Pilet, C. Coquard, G. Daculsi, "Influence of biphasic calcium phosphate granulometry on bone ingrowth, ceramic resorption, and inflammatory reactions: preliminary in vitro and in vivo study", *J Biomed Mater Res* **46**(1) (1999) 103-11.

7. J. Toquet, R. Rohanizadeh, J. Guicheux, S. Couillaud, N. Passuti, G. Daculsi, D. Heymann, "Osteogenic potential in vitro of human bone marrow cells cultured on macroporous biphasic calcium phosphate ceramic", *J Biomed Mater Res* **44**(1) (1999) 98-108.

8. J. Delecrin, G. Daculsi, "Specific resorbable calcium phosphate coating to enhance osteoconduction", *Cells and Materials* **4** (1994). 51-62.

9. J.C. Elliott, in "Structure and Chemistry of the Apatites and Other Calcium Orthophosphates", (Elsevier, Amsterdam 1994).

10. R. Z. LeGeros, "Calcium phosphates in oral biology and medicine", *Monogr Oral Sci* **15** (1991) 1-201.

11. J.M. Bouler, R. Z. LeGeros, G. Daculsi, "Biphasic calcium phosphates: influence of three synthesis parameters on the HA/beta-TCP ratio", *J Biomed Mater Res* **51**(4) (2000) 680-4.

12. K. Ishikawa, P. Ducheyne, S. Radin, "Determination of the Ca/P ratio in calcium-deficient hydroxyapatite using X-ray diffraction analysis", *Journal of Materials Science : Materials in Medicine* **4** (1993) 165-168.

13. O. Gauthier, J.-M. Bouler, E. Aguado, R.Z. LeGeros, P. Pilet, G. Daclusi, "Elaboration conditions influence physicochemical properties and in vivo bioactivity of macroporous biphasic calcium phosphate ceramics", *Journal of Materials Science: Materials in Medicine* **10**(4) (1999) 199-204.

14. R.W. O'Brien, "Electro-acoustic effects in a dilute suspension of spherical particles", *J. Fluid Mech.* **190** (1986) 71-86.

15. R.W. O'Brien, "The electro-acoustic equation for a colloidal suspension", *J. Fluid Mech.* **212** (1990) 81-93.

16. T. Oja, Matec Applied Sciences Inc., New York. Personal communication.

17. R. Hogg, T.W. Healy and D.W. Fuerstenau, "Mutual coagulation of colloidal dispersions", *Trans. Faraday Soc.* **66** (1966) 490.

18. I.O. Smith, M.K. Soto, M.J. Baumann and L.R. McCabe, "*In vitro* stability predictions of osteoblast interaction with hydroxyapatite and β-tricalcium phosphate", *Ceramic Transactions, Vol. 147; Bioceramics: Materials and Applications IV* (2003) 123.

19. P. Weiss, M. Lapkowski, R.Z. LeGeros, J.M. Bouler; A. Jean, G. Daclusi, "Fourier-transform infrared spectroscopy study of an organic-mineral composite for bone and dental substitute materials", *Journal of Materials Science: Materials in Medicine* **8**(10) (1997) 621-629.

20. R.M. Kowalchuk, S.R. Pollack and T.A. Corcoran, "Zeta potential of bone from particle electrophoresis: Solution composition and kinetic effects", *J. Biomed. Mater. Res.* **29** (1995) 47-57.

21. J.F. Key, R.H. Doremus and M. Jarcho, "Ion micromilling of bone-implant interfaces", *Trans. 4th Ann. Meet. Soc. Biomaterials: 10th Int. Biomaterials Symposium* (1978) 154-155.

22. P.N. DeAza, Z.B. Luklinska, M. Anseau, F. Guitian and S. DeAza, "Morphological studies of pseudowollastonite for biomedical application", *J. Microsc.* **182**(4) (1996) 24-31.

23. L.L. Hench, "Bioactive ceramics"; in Bioceramics: materials characteristics versus *in vivo* behavior, Vol. 523. Edited by P. Ducheyne and J. Lemons. (Annals N.Y. Acad. Sci. 1988) pp. 54.

24. R. Shu, R. McMullen, M.J. Baumann, L.R. McCabe, "Hydroxyapatite accelerates differentiation and suppresses growth of MC3T3-E1 osteoblasts", *J. Biomed. Mater. Res.* **67A**(4) (2003) 1196-1204.

25. P. Ducheyne, C.S. Kim and S.R. Pollack, "The effect of phase differences on the time-dependent variation of the zeta potential of hydroxyapatite", *J. Biomed. Mater. Res.* **26** (1992) 147-168.

26. B.V. Velamekanni and F.F. Lange, "Effect of interparticle potentials and sedimentation on particle packing density of bimodal particle distributions during pressure filtration", *J. Am. Ceram. Soc.* **74** (1991) 166-172.